

Formulation and Quantification of the Distributed Collinear Triad Approximation

M.Sc. thesis **ct5060**

Matthijs B nit **1115146**

02-09-2009

Colophon

Author

Matthijs Bénit
1115146
m.p.benit@student.tudelft.nl

Institute

Delft University of Technology
Faculty of Civil Engineering & Geosciences
Section Hydraulic Engineering – Environmental Fluid Mechanics
Stevinweg 1, 2628 CN Delft

Graduation committee

Prof. dr. ir. G. S. Stelling
Section Environmental Fluid Mechanics

Dr. ir. L. H. Holthuijsen (daily supervisor)
Section Environmental Fluid Mechanics

Dr. ir. G. Ph. Van Vledder
Section Environmental Fluid Mechanics

Dr. ir. P. J. Visser
Section Hydraulic Engineering

Dr. ir. A. J. Van Der Westhuysen
Deltares

Abstract

The author has, in order to obtain a M.Sc. degree, worked on the development of the Distributed Collinear Triad Approximation (DCTA), a spectral formulation of the effects of triad interactions in wind generated waves. The basic idea was first suggested by N. Booij and further developed by L.H. Holthuijsen. It was first presented at the 30th International Conference on Coastal Engineering in San Diego (Holthuijsen and Booij, 2006). The present study was a collaborative effort of these two authors and the present author, which consisted of two parts, a description of the contribution of the author to the conceptual formulation and a description of the quantification of the DCTA .

The contributions of the author to the formulation, the first part of this report, entailed his participation in discussions among the developers, the implementation of the resulting suggestions of these conversations in an experimental version of the spectral wave model SWAN (Booij et al., 1999) and testing of the suggestions with trial calculations. The final formulation of the DCTA was presented in a second publication (Booij et al., 2009) of which the present author is co-author. This manuscript was included in this report.

In the second part, the latest formulation and its quantification were presented. After the validation of the DCTA, in which its ability to converge any spectrum to a universal shape in various simple bathymetries was established, the calibration was subsequently done with measurements of Smith (2004). To remove the influence of a malicious simulation of the dissipation, a joint calibration was executed of both the Battjes-Janssen breaker parameter γ and the tuneable coefficient of the DCTA λ . For every incident spectrum (out of 31), the optimum values for γ and λ was found through a minimisation of the error-values for H_{m0} and T_{m01} . The average value for γ was 0.787 (standard deviation 0.068) and the average value for λ was 0.130 (standard deviation 0.064). The performance calibrated DCTA was then verified on a series of laboratory (Beji and Battjes, 1993; Smith, 2004; Boers, 2005) and field measurements (Delilah, Amelander Zeegat, Haringvliet from Ris et al., 2002). This indicated that the DCTA estimated the evolution of the spectra towards a universal shape and the generation and smoothening of harmonic frequency peaks well. Contrary to the LTA, it generated harmonic frequency peaks at every multiple of the base frequencies and was able to remove the peak in shallow water. However, it overestimated the

height of the peak and the height of the tail and did not smooth the shape frequencies between harmonic frequencies sufficiently.

It was concluded that the transfer of energy towards higher frequencies was inhibited by a rapid saturation of the spectral tail. Including a frequency dependent distribution of the dissipation, as suggested in the literature and confirmed with measurements (Mase and Kirby, 1992; Kirby and Kaihatu, 1996; Chen et al., 1997; Herbers et al., 2000; Kaihatu et al., 2007), will probably improve the results, as this will invoke a continued energy flux through the spectrum from lower frequencies to higher where energy is eventually dissipated.

Acknowledgements

The aid of my daily supervisor, Leo Holthuijsen, is deeply appreciated, as it was invaluable for the progress of this thesis. His suggestions, feedback and comments have helped me greatly to successfully end this M.Sc. thesis. I am also very grateful for the efforts of the other members of the graduation committee.

I am very grateful to Jane Smith for providing me with the observations that were used for the calibration in this study and for her permission (and Linwood Vincent's) to publish the results. I obtained the observations of Marien Boers (2005) from the ONR virtual testbed published by Ris et al. (2002) and I greatly appreciate the implied permission to publish the results.

Deltares has provided financial support to seek collaboration in Paris for this study, for which I am very grateful.

Matthijs B nit

Table of contents

1	Introduction	11
Part I	13
2	Manuscript submitted to the ICCD 2009	15
Part II	31
3	Triad interactions	33
4	Formulation	35
5	Implementation	39
6	Validation.....	41
7	Calibration	51
8	Verification.....	63
9	Conclusions and recommendations.....	85
References	89
List of figures	93
List of tables	97
Nomenclature	99
Appendices	101
Appendix A	Code listing	102
Appendix B	Smith measurements.....	106
Appendix C	Results calibration	107

1 Introduction

The aim of the study that is described in this report was to quantify (validate, calibrate and verify) the Distributed Collinear Triad Approximation (DCTA), a spectral formulation of the effects of triad interactions. The basic idea was first suggested by N. Booij and further developed by L.H. Holthuijsen. It was first presented at the 30th International Conference on Coastal Engineering in San Diego (Holthuijsen and Booij, 2006). The present study is a collaborative effort of these two authors and the present author, which started in September 2008. It began with a continuation of the development of the formulation of the DCTA and ended with its quantification. Before the ending of the present study, a second publication, with an updated form of the formulation and intermediate results of the quantification was submitted to the 6th International Conference on Coastal Dynamics in Tokyo (Booij et al., 2009).

Although the general formulation was clear, several details, such as the exact expression of the scaling and the manner in which mismatches from exact resonance are accounted for^a, were still being perfected by the time the present study commenced. The author participated in, and contributed to, discussions between the developers, N. Booij and L.H. Holthuijsen. He implemented the suggestions that were the result of these conversations in an experimental version of the spectral wave model SWAN (Booij et al., 1999) and conducted trial simulations of the evolution of several different incident spectra that were measured by Smith (2004). The results were analysed and used for the continuation of the detailed conceptual development in succeeding discussions. It is impossible to describe in detail the exact suggestions and contributions of the present author to the latest formulation of the DCTA due to its gradual, evolutionary development. These contributions have become an integral part of the DCTA and therefore the present author is co-author of the second publication on the DCTA: the manuscript that was submitted to the Coastal Dynamics Conference (Booij et al., 2009).

^a See chapter 4.

As the conceptual development crystallized, the focus gradually shifted towards the quantification of the DCTA. In order to investigate and improve its ability to simulate the effects of triad interactions, it was verified and consequently calibrated with measurements by the present author. The calibration was executed for two different formulations for the scaling of the DCTA. The results of the latest formulation (equation 4-7) are presented in this report. Finally, the calibrated version of the DCTA was applied to a large series of laboratory and field measurements.

This study was carried out by the present author to obtain a M.Sc. degree and this report describes in detail the work carried out by the present author to fulfil the necessary requirements. Its structure therefore reflects the dualistic nature of his activities by a division in two separate parts. The contributions to the conceptual development of the DCTA are described in the first part. It presents the manuscript of Booij et al. (2009) that was submitted to the Coastal Dynamics Conference. This work was done in close collaboration with the other authors of that manuscript. Some additional remarks about the work that the present author has carried out are made in chapter 3. The second part describes work that was exclusively done by the author and is a supplement to this manuscript. It starts with some background information on triad interactions (chapter 3) and then describes the formulation of the DCTA (chapter 4) in more detail than the Coastal Dynamics manuscript and its implementation (chapter 5). Next, the quantification is treated: the validation, the calibration and the verification are described in chapters 6, 7 and 8. In chapter 9, the conclusions of this study and recommendations are presented.

The following remarks concerning the design of the plotted parameters and spectra in this report may help the reader to understand the displayed content promptly. Throughout the whole report, a fixed set of colours has been used to represent the plotted spectra. The red line always represents measured spectra, the green line DCTA results, the blue line LTA results and the black line results from simulations without the triad interaction source term. The locations of which the spectra are presented in this report are marked in the bathymetry figures with an orange colour. Although the formulation of the DCTA was expressed in terms of intrinsic (relative) radian frequencies and action densities $N(\sigma)$, the output of SWAN is usually given in terms of absolute angular frequencies and energy densities $E(f)$. Additionally, the displayed spectra are always scaled throughout this report according to equation 6-2. Therefore, all spectra represent scaled energy densities as a function of angular frequency $G(f)$.

Part I

**Manuscript submitted to the
International Conference on Coastal
Dynamics 2009**

2 Manuscript submitted to the ICCD 2009 ^b

A DISTRIBUTED COLLINEAR TRIAD APPROXIMATION IN SWAN

N. Booij^c, L.H. Holthuijsen^d and M. P. B nit^e

Abstract

Waves entering the surf zone initially develop higher harmonics, which disappear after two or three wave lengths. The default Lumped Triad Approximation (LTA) in the SWAN wave model generates only (persistent) second harmonics. An alternative approximation (DCTA) is suggested which is based on an analogy with quadruplet wave-wave interactions. It initially generates all (transient) higher harmonics and subsequently a smooth universal spectral tail, in agreement with observations. The DCTA is calibrated with 31 published laboratory cases and then applied to 20 other, one- and two-dimensional cases, including field cases. The conclusion is that using the DCTA instead of the LTA barely affects the significant wave height but improves the mean period and spectral tail of the computed spectra. Further improvements are expected with enhanced high-frequency dissipation.

Key words: wave model, surf zone, triad wave-wave interactions, laboratory wave observations, field wave observations, wave breaking

^b6th International Conference on Coastal Dynamics 2009 in Tokyo, Japan

^cDigital Hydraulics, Willemsplein 535, 3016 DR, Rotterdam, the Netherlands, n.booij@digital-hydraulics.com

^dFaculty of Civil Engineering and Geosciences, Delft University of Technology, Stevinweg 1, 2628 CN, Delft, the Netherlands, l.h.holthuijsen@citg.tudelft.nl

^eFaculty of Civil Engineering and Geosciences, Delft University of Technology, Stevinweg 1, 2628 CN, Delft, the Netherlands, m.p.benit@student.tudelft.nl

1. Introduction

When random waves, with a unimodal spectrum, enter the surf zone, triad wave-wave interactions often generate a secondary peak at twice the peak frequency, and sometimes also at higher multiples of the peak frequency. However, these peaks seem to persist only over a short distance because triad wave-wave interactions force the spectral tail into a smooth, universal shape. Observations and theoretical consideration (Toba, 1973; Zakharov, 1999; Resio et al., 2001; Smith, 2004) show that the shape of this tail is $k^{-4/3}$ for $kd < 1$ (where k is wave number and d is water depth) and $k^{-5/2}$ for $kd > 1$. This evolution to a smooth universal tail also occurs for multimodal spectra. This behavior can be explained with the theory of near-resonant triad interactions (e.g. Herbers et al., 2000; Janssen et al., 2006) but using this theory in operational models is prohibitively expensive in terms of required computer capacity. Some models therefore use a parameterization of the triad interactions. One of the simplest is the Lumped Triad Approximation of Eldeberky (1996), which is used in the third-generation wave model SWAN (Booij et al., 1999). However, this approximation only accounts for the initial evolution of the second harmonics as the waves enter the surf zone. It does not properly account for the evolution of the universal smooth tail as the waves travel further. A simple reduction of the expression for quadruplet wave-wave interactions (Hasselmann, 1963), supplemented with forcing the universal tail and a tuneable scaling suggests another parameterization that does account for both the initial evolution of higher harmonics in the spectrum and the transition to a universal, smooth tail.

2. The wave model

Our parameterization is formulated in terms of a source term of the spectral action balance of the waves:

$$\begin{aligned} \frac{\partial N(\sigma, \theta; x, y, t)}{\partial t} + \frac{\partial c_{g,x} N(\sigma, \theta; x, y, t)}{\partial x} + \frac{\partial c_{g,y} N(\sigma, \theta; x, y, t)}{\partial y} + \\ + \frac{\partial c_\theta N(\sigma, \theta; x, y, t)}{\partial \theta} + \frac{\partial c_\sigma N(\sigma, \theta; x, y, t)}{\partial \sigma} = \frac{S^E(\sigma, \theta; x, y, t)}{\sigma} = S^N(\sigma, \theta; x, y, t) \end{aligned} \quad (1)$$

where $N(\sigma, \theta)$ is the action density spectrum (action density is defined as energy density divided by the relative frequency $N(\sigma, \theta) = E(\sigma, \theta) / \sigma$). The first term in the left-hand side of these equations represents the local rate of change of action density in time, the second and third terms represent propagation of action in geographical space (with propagation velocities $c_{g,x}$ and $c_{g,y}$ in x - and y -space, respectively, thus

accounting for depth and current-induced shoaling or bunching). The fourth term represents depth- and current-induced refraction and diffraction (with propagation velocity c_θ in θ -space). The fifth term represents depth- and current-induced frequency shifting (with propagation velocity c_σ in σ -space). The term $S^E(\sigma, \theta)$ is the source term for the energy evolution of the waves and $S^N(\sigma, \theta)$ is the same for the action evolution, representing the effects of generation, nonlinear wave-wave interactions and dissipation. For the computations of this study, we will use the SWAN model of Booij et al. (1999), which is based on this equation.

We use the default settings of SWAN for all physical processes and numerical schemes except for the following. In the calibrations, we use the bottom friction coefficient C_{bottom} in the JONSWAP expression of Hasselmann et al. (1973) to calibrate the dissipation outside the surf zone (and continue to use it inside the surf zone) and we use the ratio of maximum wave height over local depth $\gamma = d/H_{max}$ in the formulation of depth-induced breaking of Battjes and Janssen (1978) as a tuning parameter to calibrate the dissipation inside the surf zone. It must be emphasized that (a) the default formulation for white-capping in SWAN is due to Hasselmann (1974) as adapted by the WAM group (1988), which implies that this form of dissipation is proportional to the energy density $E(\sigma, \theta)$ and wave number k and that (b) in the formulation of Battjes and Janssen (Battjes and Janssen, 1978) dissipation by depth-induced breaking is proportional to the energy density $E(\sigma, \theta)$ and does not otherwise depend on wave number, frequency or direction. Rogers et al. (2003) argue that dissipation due to white-capping should be proportional to $k^{1.5}$ or k^2 and Chen et al. (1997) argue that dissipation due to depth-induced breaking should be proportional to σ^2 . We will have cause to return to these options in the following. The default formulation in SWAN for the triad wave-wave wave interactions is the Lumped Triad Approximation (LTA) of Eldeberky (1996). It is the purpose of the present study is to propose an alternative formulation for this.

3. The triad parameterization

Our parameterization of the triad wave-wave interactions is based on a reduction of the expression for the *quadruplet* wave-wave interactions (e.g., Hasselmann, 1963), which can be represented as

$$S_{nl4}^N(\mathbf{k}_1) = \iiint N(\mathbf{k}_3) N(\mathbf{k}_{1+2-3}) [T_a N(\mathbf{k}_2) - T_b N(\mathbf{k}_1)] d\mathbf{k}_2 d\mathbf{k}_3 \quad (2)$$

for the resonance conditions of wave numbers $\mathbf{k}_{1+2-3} = \mathbf{k}_1 + \mathbf{k}_2 - \mathbf{k}_3$ and frequencies $\sigma_{1+2-3} = \sigma_1 + \sigma_2 - \sigma_3$; T_a and T_b are interaction coefficients. We similarly formulate *triad* wave-wave interactions by removing one component from this expression:

$$S_{nl3}^N(\mathbf{k}_1) = \iint N(\mathbf{k}_{1+2}) [\chi_a N(\mathbf{k}_2) - \chi_b N(\mathbf{k}_1)] d\mathbf{k}_2 \quad (3)$$

for the resonance conditions $\sigma_{1+2} = \sigma_1 + \sigma_2$ and $\mathbf{k}_{1+2} = \mathbf{k}_1 + \mathbf{k}_2$, with unknown coefficients χ_a and χ_b . Triad resonance can occur only for collinear non-dispersive waves, so we reduce the formulation to (replacing the notation of k_{1+2} by k_3):

$$S_{nl3}^N(k_1) = \int N(k_3) [\chi_a N(k_2) - \chi_b N(k_1)] dk_2 \quad (4)$$

for the quasi-resonance conditions $k_2 = |k_3 - k_1|$ (i.e., the wave numbers match but the frequencies not necessarily). To force the spectrum towards a universal tail, $N(\sigma) \sim \sigma^{-1} c_g^{-1} k^{-p}$ we take the coefficients as

$$\chi_a = \chi \sigma_2 c_{g,2} k_2^p \quad \text{and} \quad \chi_b = \chi \sigma_1 c_{g,1} k_1^p \quad (5)$$

so that in terms of the frequency spectrum,

$$S_{nl3}^N(\sigma_1) = \int \chi N(\sigma_3) [\sigma_2 c_{g,2} k_2^p N(\sigma_2) - \sigma_1 c_{g,1} k_1^p N(\sigma_1)] d\sigma_2 \quad (6)$$

A dimension analysis of expressions (5) shows that the dimension of the coefficient $[\chi] = m^{p-3}$. The dimension m^p results from forcing the spectral tail to the k^{-p} -shape. We therefore assume $\chi = \chi_0 \bar{k}^{-p}$ where \bar{k} is a characteristic wave number of the triad (we take $\bar{k} = (k_1 + k_2 + k_3)/3$). A comparison with the scaling of the Lumped Triad Approximation (LTA; Eldeberky, 1996) suggests in addition that

$$\chi = \chi_0 \bar{k}^{-p} = \lambda d^{-2} |\sin \beta| \bar{k}^{1-p} \quad (7)$$

where the bi-phase β is parameterized as

$$\beta = \pi (\tanh(\delta / Q_{Ursell}) - 1) / 2 \quad (8)$$

(Doering and Bowen, 1995) in which the Ursell number

$$Q_{Ursell} = \hat{k} \sqrt{2m_0} / (\hat{k}d)^3 \quad (9)$$

(the average wave number \hat{k} is estimated as $\hat{k} = \hat{\sigma}(gd)^{-1/2}$ with the average frequency $\hat{\sigma}$ determined from the zero-th and first moment of the energy spectrum) and $\delta = 0.2$ (Eldeberky, 1996). To account for the increasing resonance mismatch with increasing wave number, we scale the interactions with the ratio of the dispersion relationship for shallow water and the dispersion relationship for water of arbitrary depth, i.e., with $\tanh \bar{k}d / \bar{k}d$. The final expression is therefore

$$S_{nl3}^N(\sigma_1) = \int \lambda d^{-2} |\sin \beta| \bar{k}^{1-p} N(\sigma_3) \tanh \bar{k}d / \bar{k}d \left[\sigma_2 c_{g,2} k_2^p N(\sigma_2) - \sigma_1 c_{g,1} k_1^p N(\sigma_1) \right] d\sigma_2 \quad (10)$$

for the quasi-resonance conditions $k_2 = |k_3 - k_1|$, with only the scaling coefficient λ as a tuneable parameter. We call this approximation the *distributed*, collinear triad approximation (DCTA), to contrast it with the *lumped* triad approximation (LTA; which is also collinear).

4. The calibration

For the calibration of the scaling coefficient λ , we use the rather extensive observations of Smith and Vincent (2004) of waves in a laboratory flume propagating over a 1:30 flat bottom (Fig. 1) with a variety of spectra (31 cases with unimodal and bimodal incident spectra, with various degrees of wave steepness and spectral width). We determined the values of λ and γ that provided the best fit (in a least-square-error sense) between the computed significant wave height and mean period (from the zero-th and first-order moment of the spectrum). The technique that we employed was to first determine, for each individual case, the rms-error between the computed and observed significant wave height for a large number of values of λ and γ , and then to determine the loci of the line of slowest decent of the rms-error (this gives the optimal value of λ for any given value of γ and vice versa). We then determined along this line the minimum value of the rms error between the computed and observed mean period. We thus determined for each individual case the optimum values of λ and γ . These values varied between 0.05 and 0.30 and between 0.69 and 0.93 respectively. This seems to be a disturbingly wide range but it turns out that the results are only weakly sensitive to the value of λ (see for example Figs. 2 and 3, to be treated next). The mean values of λ and γ over all 31 cases thus obtained were $\lambda = 0.13$ and $\gamma = 0.786$. In the following, we use the default value in SWAN $\gamma = 0.73$ as it is based on considerably more data (Booij et al., 1999). Using the DCTA and these values $\lambda = 0.13$ and $\gamma = 0.73$ for all 31 cases slightly increased, compared to the results obtained with the default LTA, the rms-error in the significant wave height from

0.0036 m to 0.0037 m (+ 3%) and decreased the rms-error in the mean wave period from 0.068 s to 0.047 s (- 30%).

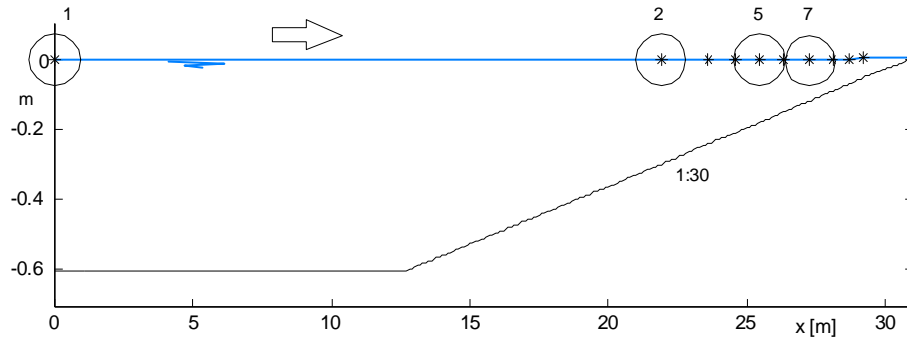


Fig. 1 The bottom profile of the observations of Smith and Vincent (2004) with the locations of stations 1, 2, 5 and 7 used for the comparison with the spectra computed in this study.

To illustrate the effect of this calibration on the computed spectra, we show in Fig. 2 the results for the steepest waves in the data set of Smith and Vincent (2004) with a spectrum that is nominally unimodal (case 31 of Smith and Vincent, 2004; the small secondary and tertiary peaks at station 1 may have been generated by the wave maker or in the flume before the waves arrived at station 1). Note that the vertical scale in Fig. 2 is such that the universal $k^{-4/3}$ -tail would appear as a horizontal line. It is obvious that in this case, the LTA (a) generates only the second and fourth harmonic of the incident peak (the eighth harmonic is outside the range of the computations), (b) considerably overestimates these peaks and (c) does not remove these secondary peaks as the waves propagate further into the surf zone. However, it reduces the primary peak reasonably well. It is equally obvious that in this case, the DCTA (a) generates all harmonics of the incident peak with the correct magnitude and that it forces the tail to the universal shape, but also that (b) it does not reproduce the reduction of the primary peak very well and that (c) it is too slow in smoothing the spectral tail. Using the optimum (i.e., calibrated) values for this case of $\lambda = 0.30$ and $\gamma = 0.69$ reduces the primary peak slightly and enhances the spectral levels at the high frequencies somewhat but overall this does not improve the results significantly (See Fig. 3; in other words, the results are not very sensitive to changes in the value of λ and γ ; at least not in combination).

5. The verification

We have verified the calibrated model (i.e., all coefficients at their default values and $\lambda = 0.13$) with the laboratory observations of Boers (2005; also in Ris et al., 2002) and the field observations in a branch of the Rhine estuary published by Ris et al. (2002).

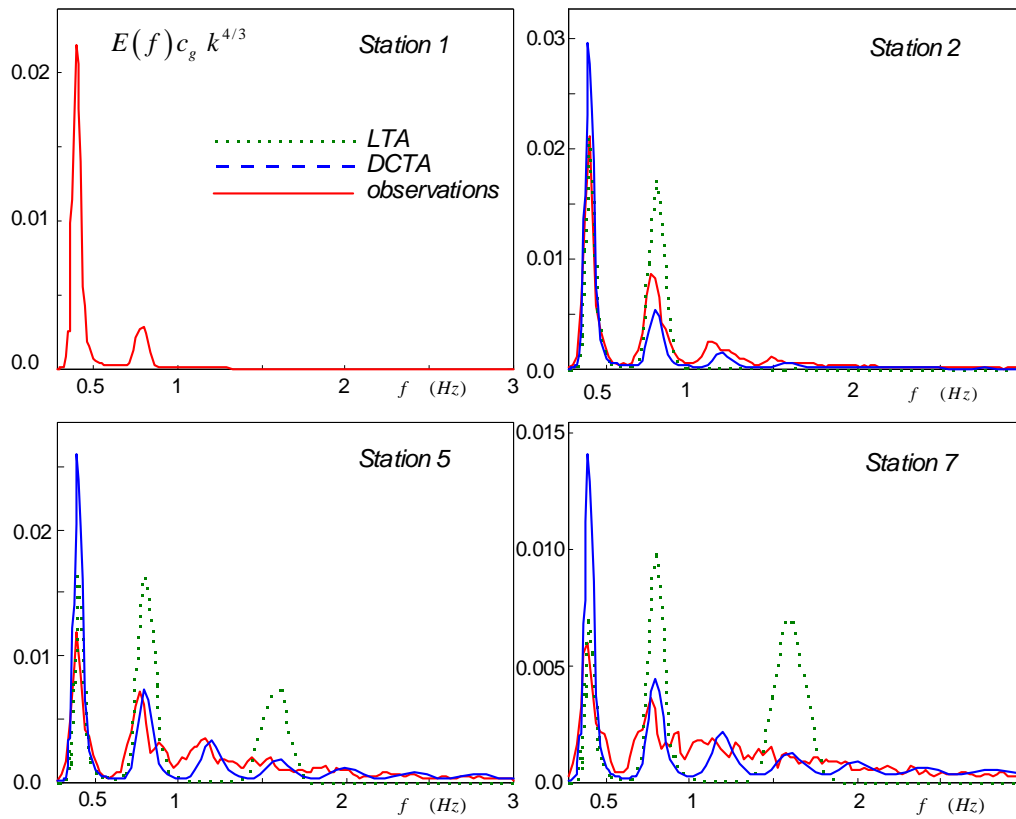


Fig. 2 The evolution of the spectrum (stations 1, 2, 5 and 7 in Fig. 1), computed with the LTA and the DCTA over a 1:30 flat bed, compared with the spectra observed by Smith and Vincent (2004). Note that the vertical scale is such that a $k^{-4/3}$ -tail would appear as a horizontal line.

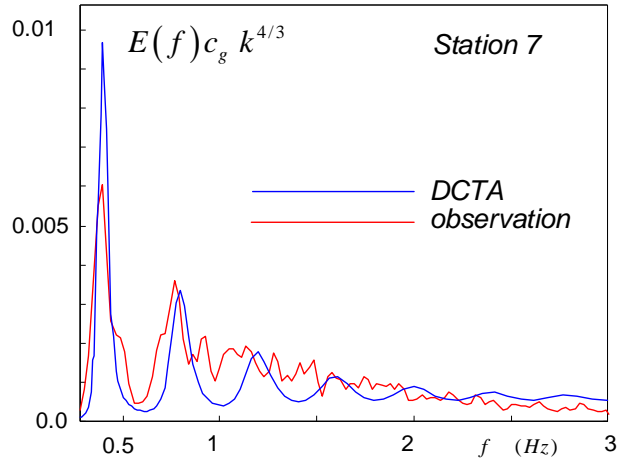


Fig. 3 The spectrum at station 7 (in the upper panel of Fig. 1), computed with the DCTA calibrated for this case, compared with the spectrum observed by Smith and Vincent (2004). Note that the vertical scale is such that a $k^{-4/3}$ -tail would appear as a horizontal line.

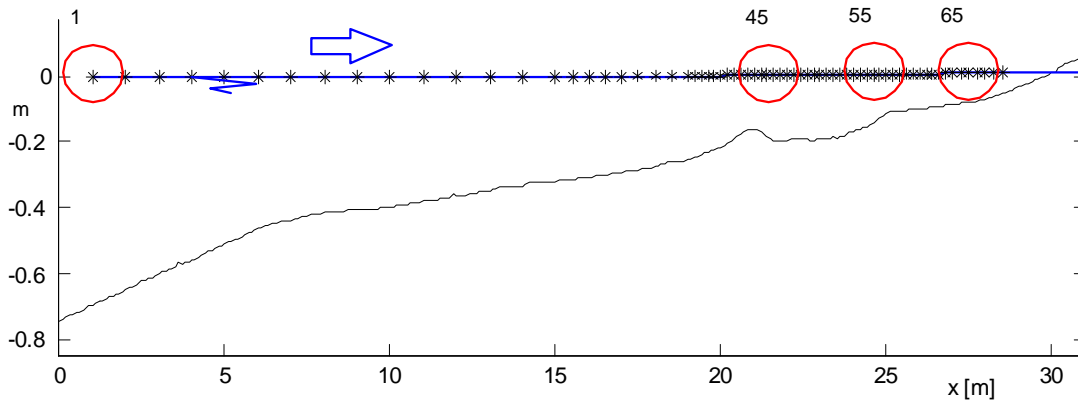


Fig. 4 The bottom profile of the observations of Boers (2005) with the locations of stations 45, 55 and 65 used for the comparison with the spectra computed in this study.

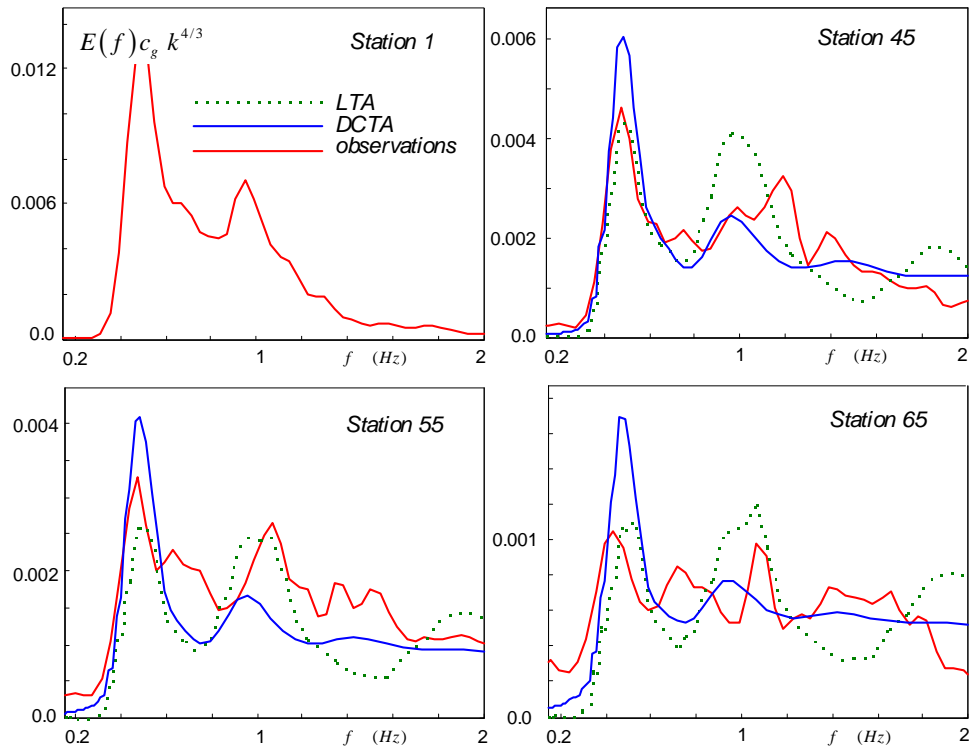


Fig. 5 The evolution of the spectrum (stations 1, 45, 55 and 65 in Fig. 4), computed with the LTA and the DCTA over a natural bed in a laboratory flume, compared with the spectra observed by Boers (2005; also in Ris et al., 2002). Note that the vertical scale is such that a $k^{-4/3}$ -tail would appear as a horizontal line.

Boers (2005) published rather detailed observations of the evolution of waves in 3 cases (69 spectra per case, Fig. 4) over a natural bottom profile in a laboratory flume. We show here our results for his case 1 in Fig. 5. Note that, just as in Figs. 2 and 3, the vertical scale in Fig. 5 is such that the universal $k^{-4/3}$ -tail would appear as a horizontal line. Again, it is obvious that, the LTA (a) generates only the second and fourth harmonic of the incident peak (the eighth harmonic is outside the range of the computations), (b) generally overestimates these peaks and (c) does not remove these secondary peaks as the waves propagate further into the surf zone. But again (as in the previous comparison), it reproduces the reduction of the primary peak reasonably well. It is equally obvious that, the DCTA (a) generates all harmonics of the incident peak but, in this case, not always with the correct magnitude and that it forces the tail to the universal shape at approximately the correct level, but also that (b) it does not reproduce the reduction of the primary peak very well and that (c) it creates a spectral tail that is too smooth (although one may argue that the shape of the observed tail is rather irregular).

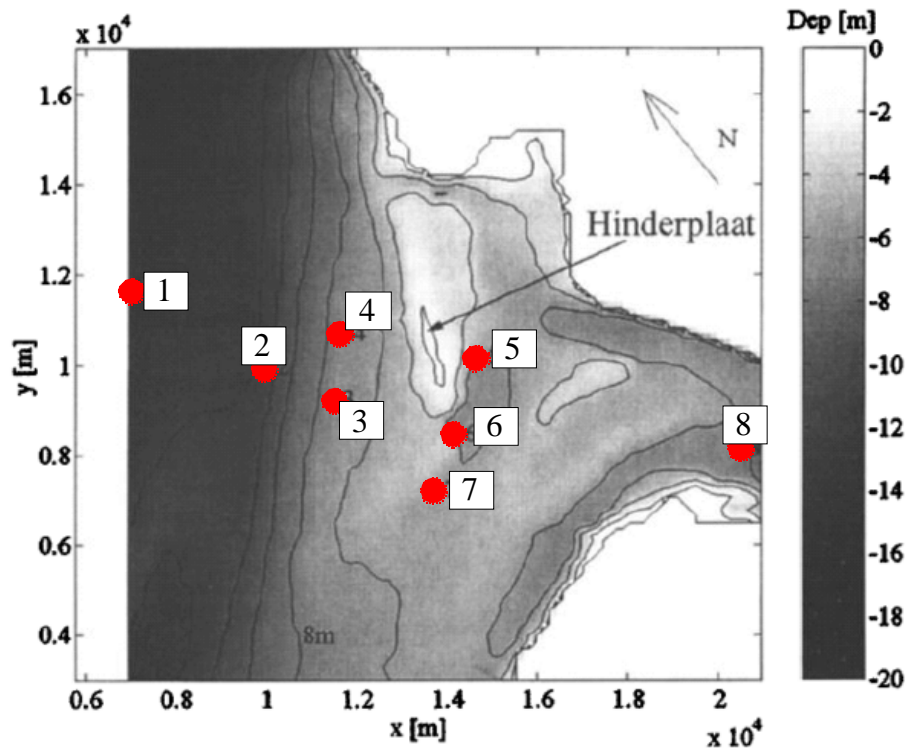


Fig. 6 The bathymetry of the Haringvliet, a branch of the Rhine estuary in the Netherlands, with the southern North Sea towards the west. The labels indicate the name and position of the buoys.

The Haringvliet is a branch of the Rhine estuary in the southwest of the Netherlands that is separated from the main estuary by sluices. The bathymetry of the area and the locations of the eight observation stations are shown in Fig. 6. The geographic situation can be characterized as a relatively shallow bay that penetrates a few kilometers into the coast, with no currents during the observations (the sluices were closed and the tides were low). The water depth is 4 to 6 m in the area considered (including the deep water approach). And the surface area is about 10km x 10km. The bay is partly protected from the southern North Sea by a shoal (called the “Hinderplaat”, Fig. 6) of roughly 1km x 4km surface area, extending across half the bay entrance. The water depth over the top of the shoal during the observations was about 2 m. The waves were measured in deep water with a WAVEC pitch-and-roll buoy (station 1), six Waverider buoys scattered around the shoal (stations 2 to 7), and one wave gauge located about 5 km behind the shoal (station 8). The wind velocity, the wind direction and the water level were measured at a site near station 6. From the extensive data set, one case is selected from a local storm in the southern North Sea on October 14, 1982, which generated waves from southwesterly directions. SWAN

computations are carried out at 2300 UTC on this day. This time was selected because (1) the wind speed and direction were fairly constant, (2) the waves were fairly high (for the observation period of 13 weeks), and (3) the water level was sufficiently low to see the generation of a significant secondary peak in the spectra near the shoal but not so low that the shoal would be dry. The observed incident significant wave height was 3.56 m, the incident mean wave period (from the zero-th and first moment of the observed spectrum) was 6.7 s and the incident mean wave direction was 306° and the directional spreading was 31° (definitions of Kuik et al., 1988). The wind was assumed to be uniform and stationary with an observed speed of 14.0 m/s and direction 300° . The waves approach the estuary from deep water and break over the shoal with a reduction of the significant wave height from about 3.6 m in deep water to 2.5 m just in front of the shoal to about 0.6 m behind the shoal. The local wind regenerates the waves behind the shoal to about 1.1 m significant wave height at station 8. The observations at the various stations were not synchronous. Therefore the two nearest observations on either side of 2300 UTC are considered at each station (Fig. 5).

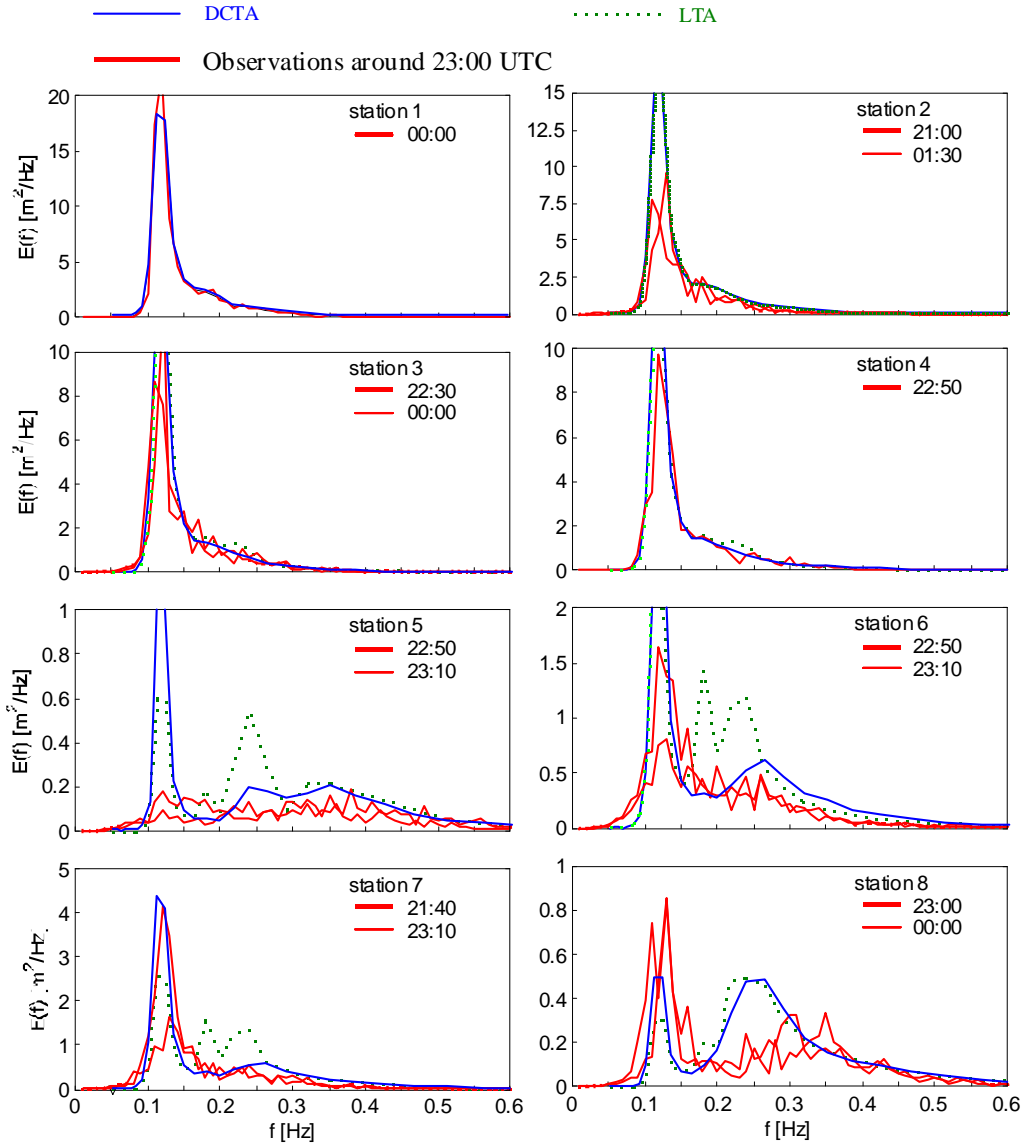


Fig. 7 The computed spectra at the various stations compared with the observed stations bathymetry of the Amelanders Zeegat in the north of the Netherlands (southern North Sea). The labels indicate the name and position of the buoys.

The travel time of the waves through the area is sufficiently short that stationary computations can be used. The computations are carried out with all physical processes of propagation, generation, dissipation and wave-wave interactions active (except diffraction). Triad wave-wave interactions are therefore accompanied by all other processes. The agreement between the observed spectra and the spectra computed with the LTA is reasonable (Fig. 7) if allowance is made for the large variation in scale of the

spectra (e.g., station 5 with a twenty fold change in scale in energy density compared to station 1). Nevertheless, the decay of the primary peak is not well predicted and the regeneration of high-frequency energy is over-predicted. It was verified with repeated computations that water level variations during the residence time of the waves cannot explain these discrepancies at the low frequency peak. However, it must be stressed that only small residuals of low-frequency energy are compared here. For instance, the observed reduction of the peak level between stations 1 and 8 (where the discrepancy is largest) is about 95% whereas the computed reduction is 97%. The regeneration at high frequencies may be due to too much energy transfer from the lower frequencies by the LTA or by too much generation by wind. Repeated computations without triad wave-wave interactions but with wind and vice versa show that both processes are equally responsible for this high-frequency regeneration. Using the DCTA instead of the LTA improves the computational results for the higher frequencies in the sense that at stations 5, 6 and 7, i.e., the stations just behind the shoal, where the effect of triad wave-wave interactions are expected to be largest, the agreement with the observations at high frequencies is greatly improved. However, the energy level of the primary peak is severely over-predicted. This indicates a restriction of “pumping” energy from the primary peak to the higher frequencies (where that extra energy would presumably be dissipated). The over-prediction at station 8 is not removed and it is therefore assumed to be due to an over-estimation of the regeneration by wind.

We computed another 16 cases (1 laboratory case and 15 field cases; results not shown here) and found basically the same results: an improvement in the level and shape of the spectral tail but a delayed decay of the primary peak when using the DCTA instead of the LTA.

6. Summary and discussion

We have formulated an approximation of triad wave-wave interactions based on an analogy with the formulation of quadruplet wave-wave interactions. For waves entering the surf zone, this approximation allows the initial evolution of all collinear super-harmonics in the wave spectrum but eventually forces a universal shape of the spectral tail (modeled as a saturation level). The time scale of these interactions is derived from a dimension analysis, a comparison with the Lumped Triad Approximation (LTA - which is based on a Boussinesq model), a heuristic correction for the resonance mismatch and a calibration of one coefficient. This approximation transfers energy between all frequencies, permitting upward and downward shifting of energy (along a common spectral direction) - hence the name “*Distributed* Collinear

Triad Approximation (DCTA)“ as opposed to the “*Lumped* Triad Approximation” (LTA) which transfers energy only upwards to second harmonics.

The comparison with observations shows the required qualitative behavior of the initial generation of the super-harmonics and the subsequent smoothing to a universal shape of the spectral tail. Both the time scale of generating the super-harmonics and the magnitude of these super-harmonics agree reasonably well with the observations (after calibration) but the transfer of energy from lower to higher frequencies seems to be inhibited when the spectral tail attains its universal shape. This inhibition leaves the spectral level of the primary peak of the spectrum at a value that is too high: the triad “pump”, which transfers energy from the primary peak to the higher frequencies is stopped too soon because dissipation at the high frequencies is too low. The LTA does not suffer from this problem to the same extent because the saturation level of the high frequencies is much higher than that in the DCTA. This interpretation in terms of an energy flux through the spectrum is essentially the model of Herbers et al. (2000). The problem seems therefore to be in the high-frequency dissipation. In SWAN this dissipation is assumed to be proportional to the spectral energy density with a uniform weighting over the frequencies (based on Beji and Battjes, 1993). Adding a σ^2 dependency to the depth-induced dissipation (as suggested by Chen et al., 1997) and a $k^{1.5}$ or k^2 dependency (as suggested by Rogers et al., 2003) would enhance the high-frequency dissipation, thus allowing the triad wave-wave interactions to “pump” more energy to the higher frequencies and consequently decaying the primary peak at a higher rate than it does in the present computations, even when the tail has achieved its equilibrium level. Adding such dependency is obviously the next step in the development of SWAN.

Acknowledgements

We are very grateful to Jane Smith for providing us with the observations that we used for the calibration in this study and for her permission (and Linwood Vincent’s) to publish the results. We obtained the observations of Marien Boers from the ONR virtual testbed published by Ris et al. (2002) and we greatly appreciate the implied permission to publish the results.

References

- Booij, N., R.C. Ris and L.H. Holthuijsen, 1999. A third-generation wave model for coastal regions, Part I, Model description and validation, *J. Geophys. Res.*, 104, C4: 7649-7666
- Battjes, J.A. and J.P.F.M. Janssen, 1978. Energy loss and set-up due to breaking of random waves, *Proc. 16th Conf. Coastal Engineering*, Hamburg, ASCE, New York: 569-587
- Beji, S. and J.A. Battjes, 1993. Experimental investigation of wave propagation over a bar, *Coastal Engineering*, 19: 151 - 162
- Chen, Y., R.T. Guza and S. Elgar, 1997. Modelling spectra of breaking surface waves in shallow water, *J. Geophys. Res.*, 102, C11: 25,035 – 25,046
- Doering, J.C. and A.J. Bowen, 1995. Parameterization of orbital velocity asymmetries of shoaling and breaking waves using bispectral analysis, *Coastal Engineering*, 26, 1-2: 15-33
- Eldeberky, Y., 1996. *Nonlinear transformation of wave spectra in the nearshore zone*, Ph.D. thesis, Delft University of Technology, Department of Civil Engineering, The Netherlands, 203 p.
- Hasselmann, K., 1963. On the nonlinear energy transfer in a gravity-wave spectrum. Part 3. Evaluation of the energy flux and swell-sea interaction for a Neumann spectrum, *J. Fluid Mech.*, 15: 385-398
- Hasselmann, K., T.P. Barnett, E. Bouws, H. Carlson, D.E. Cartwright, K. Enke, J.A. Ewing, H. Gienapp, D.E. Hasselmann, P. Kruseman, A. Meerburg, P. Müller, D.J. Olbers, K. Richter, W. Sell and H. Walden, 1973. Measurements of wind-wave growth and swell decay during the Joint North Sea Wave Project (JONSWAP), *Dtsch. Hydrogr. Z., Suppl.*, A8, 12, 95 p.
- Hasselmann, K., 1974. On the spectral dissipation of ocean waves due to white-capping, *Bound.-Layer Meteor.*, 6, 1-2: 107-127
- Herbers, T.H.C., N.R. Russnogle and S. Elgar, 2000. Spectral energy balance of breaking waves within the surf zone, *J. Phys. Oceanogr.*, 30, 11: 2723-2737
- Janssen, T.T., T.H.C. Herbers and J.A. Battjes, 2006. Generalized evolution equations for nonlinear surface gravity waves over two-dimensional topography, *J. Fluid Mech.*, 552: 393- 418
- Kuik, A.J., G.Ph. Van Vledder and L.H. Holthuijsen, 1988, A method for the routine analysis of pitch-and-roll buoy wave data, *Journal of Physical Oceanography*, 18, 7, 1020-1034
- Resio, D.T., J.H. Phil, B.A. Tracy and C.L. Vincent, 2001. Nonlinear fluxes and the finite depth equilibrium range in wave spectra, *J. Geophys. Res.*, 106, C4: 6985-700
- Ris, R.C., L.H. Holthuijsen and N. Booij, 1999, A third-generation wave model for coastal regions, Part II: Verification, *J. Geophys. Res.*, 104, C4, 7667-7681

- Ris, R., L.H. Holthuijsen, J.M. Smith, N. Booij and A.R. van Dongeren, 2002. The ONR virtual testbed for coastal and oceanic wave models, *28th Int. Conf. Coastal Eng.*, ASCE, Cardiff: 380-391
- Rogers, W.E., P.A. Hwang and D.W. Wang, 2003. Investigation of wave growth and decay in the SWAN model: three regional-scale applications, *J. Phys. Oceanogr.*, 33, 2: 366 - 389
- Smith, J.M., 2004. Shallow-water spectral shapes, *Proc. 29th Int. Conf. Coastal Engineering*, Lisbon, World Scientific, Singapore: 206-217
- Toba, Y., 1973. Local balance in the air-sea boundary processes, III. On the spectrum of wind waves, *J. Oceanogr. Soc. Japan*, 29, 2: 209-220
- WAMDI group, 13 authors, 1988. The WAM model - a third generation ocean wave prediction model, *J. Phys. Oceanogr.*, 18, 12: 1775-1810
- Zakharov, V., 1999. Statistical theory of gravity and capillary waves on the surface of a finite-depth fluid, *Eur. J. Mech. B/Fluids*, 18, 3: 327 - 344

Part II

Work by the author

3 Triad interactions

This chapter is quoted almost verbatim from the book “Waves in coastal and oceanic waters” (Holthuijsen, 2007)

When random waves, with a unimodal spectrum, approach very shallow water, e.g., the surf zone, the triad wave-wave interactions often generate a secondary peak in the spectrum, at twice the peak frequency, and sometimes also peaks at higher multiples of the peak frequency. In addition, low-frequency peaks are generated, which we ignore because they usually fall outside of the wind-wave frequency range. However, these secondary peaks seem to persist only a short distance into the surf zone (several wavelengths at most). As the waves propagate further into the surf zone, the same interactions remove these peaks and force the spectral tail into a smooth, universal shape: $E(k) \propto k^{-4/3}$ for $kd < 1$ (these components are in relatively shallow water) and $E(k) \propto k^{-5/2}$ for $kd > 1$ (these components are in relatively deep water), where k is wave number; d is local water depth and $E(k)$ is the wave number spectrum. Theoretical considerations (Toba, 1973; Zakharov, 1999), observations (Smith and Vincent, 1992, 2003; Smith, 2004) and computations with extended Boussinesq and other types of models (Herbers and Burton, 1997; Herbers et al., 2000; Resio et al., 2001; Kaihatu et al., 2007) indicate that this forcing to a universal tail in very shallow water applies not only to a unimodal incident spectrum but also to a wide variety of other spectral shapes.

A special case occurs when a unidirectional *harmonic* wave enters very shallow water. Such a wave can interact with itself to create a second harmonic, at twice its frequency. The effect of this interaction is visible as a distortion of the basic harmonic: as the wave propagates, it evolves into a wave with sharper crests and flatter troughs. This is possible only if the second harmonic propagates with the same phase speed as does the basic harmonic, i.e., the energy of the second harmonic is bound to the basic harmonic. When the wave continues to propagate in ever-shallower water, it pitches forwards and breaks: it creates a steep forward face and a gentler backward slope. This implies that the phase of the second harmonic shifts in relation to the phase of the basic harmonic (while propagating at the same speed).

Similarly, when *random* waves with a *unimodal* spectrum approach the surf zone, the wave components at or near the peak of the spectrum create Stokes-like wave profiles, generating the secondary peak at twice

the peak frequency referred to above. This added energy is superimposed on the freely propagating energy at this frequency, but it is bound to the primary peak. This distinction between bound and freely propagating energy is not evident in the spectrum since a variance density spectrum does not provide such a distinction. When the random waves propagate further into the surf zone, essentially the same happens as with a harmonic wave: they pitch forwards and break. Breaking reduces the energy scale of the spectrum and is therefore quite evident in the spectrum but the forward pitching is not because phase information is not provided by the spectrum.

4 Formulation

Our parameterization is formulated in terms of a source term of the spectral action balance of the waves, which for the present formulation can be reduced to

$$\frac{\partial c_{g,x} N(\sigma, \theta; x, t)}{\partial x} = \frac{S^E(\sigma, \theta; x, t)}{\sigma} = S^N(\sigma, \theta; x, t) \quad \text{Equation 4-1}$$

where $N(\sigma, \theta; x, t)$ is the action density spectrum (action density is defined as energy density divided by the relative frequency $N(\sigma, \theta; x, t) = E(\sigma, \theta; x, t) / \sigma$), σ is the relative (thus moving with the ambient current) radial frequency, θ is the Cartesian direction, x is the geographical position and t is time. The left-hand side of this equation represent propagation of action in geographical space (with propagation velocity $c_{g,x}$ in x -space, thus accounting for depth and current-induced shoaling or bunching). The term $S^E(\sigma, \theta; x, t)$ is the source term for the energy evolution of the waves and $S^N(\sigma, \theta; x, t)$ is the same for the action evolution, representing the effects of generation, nonlinear wave-wave interactions and dissipation. For the computations of this study, we will use the SWAN model of Booij et al. (1999), which is based on this equation.

We use an analogy with the formulation for quadruplet wave-wave interactions (Hasselmann, 1963; Herterich and Hasselmann, 1980)

$$S_{nl4}^N(\mathbf{k}_1) = \iiint N(\mathbf{k}_3) N(\mathbf{k}_{1+2-3}) [T_a N(\mathbf{k}_2) - T_b N(\mathbf{k}_1)] d\mathbf{k}_2 d\mathbf{k}_3 \quad \text{Equation 4-2}$$

for the resonance conditions $\mathbf{k}_{1+2-3} = \mathbf{k}_1 + \mathbf{k}_2 - \mathbf{k}_3$ and $\sigma_{1+2-3} = \sigma_1 + \sigma_2 - \sigma_3$, in which σ_i is the frequency of the wave component with wave number \mathbf{k}_i as determined by the dispersion relationship of the linear wave theory. Here, T_a and T_b are interaction coefficients dependent on the wave numbers and frequencies involved in the interactions. We interpret this as the exchange of energy between the two components \mathbf{k}_1 and \mathbf{k}_2 as affected by the third and fourth component \mathbf{k}_3 and \mathbf{k}_{1+2-3} . We similarly formulate triad wave-wave interactions as the interaction between two components \mathbf{k}_1 and \mathbf{k}_2 as affected by a third component \mathbf{k}_{1+2}

$$S_{nl3}^N(\mathbf{k}_1) = \iint N(\mathbf{k}_{1+2}) [\chi_a N(\mathbf{k}_2) - \chi_b N(\mathbf{k}_1)] d\mathbf{k}_2 \quad \text{Equation 4-3}$$

for the resonance conditions $\sigma_{1+2} = \sigma_1 + \sigma_2$ and $\mathbf{k}_{1+2} = \mathbf{k}_1 + \mathbf{k}_2$, with unknown coefficients χ_a and χ_b . These resonance conditions are only met by collinear, non-dispersive waves which occur only in extremely shallow water (Phillips, 1960). However, triad interactions also occur under near-resonance conditions (Armstrong et al., 1962), before waves enter such shallow water, in deeper water. To parameterise this, we consider collinear components under quasi-resonance conditions, i.e., under the condition that the wave numbers match but not necessarily the frequencies (a mismatch with the exact resonance condition for the frequencies is thus allowed). Since we consider collinear interactions only^f, the vector wave number \mathbf{k} is replaced by a scalar k and the double integral of equation 4-3 is correspondingly reduced to a single integral. If we write this integral as

$$S_{nl3}^N(k_1) = \int_0^{k_1} N(k_3) [\chi_a N(k_2) - \chi_b N(k_1)] dk_2 + \int_{k_1}^{\infty} N(k_3) [\chi_a N(k_2) - \chi_b N(k_1)] dk_2 \quad \text{Equation 4-4}$$

then, to ensure that all positive wave numbers are used, the quasi-resonance conditions are $k_1 = k_2 + k_3$ (or $k_2 = k_1 - k_3$) for the first integral and $k_3 = k_1 + k_2$ (or $k_2 = k_3 - k_1$) for the second integral. This expression may therefore also be written according to equation 4-5 for the quasi-resonance condition $k_2 = |k_3 - k_1|$ ^g.

$$S_{nl3}^N(k_1) = \int_0^{\infty} N(k_3) [\chi_a N(k_2) - \chi_b N(k_1)] dk_2 \quad \text{Equation 4-5}$$

^f Due to this assumption, sub-harmonic action transfers are not represented correctly by the DCTA as these transfers are the result of so-called difference triad interactions (Herbers and Burton, 1997) which typically exchange energy among non-collinear wave components. The DCTA does calculate transfers to components with lower frequencies but with completely erroneous directions. Moreover, these frequencies are usually outside the wind-wave frequency range and are therefore ignored in this study.

^g Inadvertently, this statement was stated as such in Booij et al. (2009) while the quasi-resonant condition that was implemented in the code was $\sigma_2 = |\sigma_3 - \sigma_1|$. As resonant triad interactions only occur for non-dispersive waves, for which a linear relation exists between σ and k , both expressions are equivalent.

To force the action density spectrum $N(\sigma) = \sigma^{-1}E(\sigma)$ to converge to the universal shape $E(k) \propto k^{-p}$, with p the power of the universal spectrum, we first express this shape in terms of frequency and action density: $N(\sigma) \propto \sigma^{-1}c_g^{-1}k^{-p}$ and then accordingly choose the coefficients $\chi_a = \chi\sigma_2c_{g,2}k_2^p$ and $\chi_b = \chi\sigma_1c_{g,1}k_1^p$. The result is

$$S_{nl3}^N(\sigma_1) = \int \chi N(\sigma_3) [\sigma_2c_{g,2}k_2^p N(\sigma_2) - \sigma_1c_{g,1}k_1^p N(\sigma_1)] d\sigma_2 \quad \text{Equation 4-6}$$

The interaction thus vanishes if the equilibrium shape $N(\sigma) = \alpha\sigma^{-1}c_g^{-1}k^{-p}$ has been achieved for the spectral tail (for arbitrary α). Booij et al. (2009) showed that this formulation also ensures that the interactions conserve action.

We can infer the character of the interaction coefficient χ from a dimension analysis, supplemented with information from the Lumped Triad Approximation (LTA) of Eldeberky, which is based on a Fourier transform of the extended Boussinesq equation (Madsen and Sørensen, 1993; Eldeberky, 1996). A dimension analysis of the above expression for $S_{nl3}^N(\sigma_1)$ shows that the dimension of the coefficient $[\chi] = m^{p-3}$. We therefore take

$$\chi = \chi_0 \bar{k}^{-p} = \lambda d^{-2} |\sin \beta| \bar{k}^{1-p} \quad \text{Equation 4-7}$$

in which λ is a tuneable constant and $\bar{k} = \frac{1}{3}(k_1 + k_2 + k_3)$, the average wave number of the triad under consideration. In the LTA, the bi-phase β is parameterised as $\beta = \frac{\pi}{2} [\tanh(\delta/Q_{Ursell}) - 1]$ (Doering and Bowen, 1995) in which the Ursell number $Q_{Ursell} = \hat{k}\sqrt{2m_0}/(\hat{k}d)^3$ (the spectrum average wave number \hat{k} is estimated as $\hat{k} = \hat{\sigma}(gd)^{-1/2}$ with the average frequency $\hat{\sigma}$ determined from the zero-th and first moment of the energy spectrum) and $\delta = 0.2$ (Eldeberky, 1996).

To account for the increasing resonance mismatch with increasing wave number, we scale the interactions with the ratio of the dispersion relationship for water of arbitrary depth water and the dispersion relationship for shallow, i.e., with $\tanh \bar{k}d / \bar{k}d$.

Trial calculations

The formulation of the DCTA that is presented in this chapter is the result of an extensive development process. The author of the present report has contributed to this process by partaking in many

discussions among the first developers, N. Booij and L.H. Holthuijsen. During these discussions, various formulations for the scaling coefficient χ and the universal tail have been put forward and evaluated. These have been implemented by the present author in an experimental version of the spectral wave model SWAN (Booij et al., 1999). That code was subsequently used for trial calculations in which the evolution of four different incident spectra that were measured by Smith^h (2004) was simulated. The four spectra (listed as cases 1, 5, 20 and 31 in the description of the experiments) were chosen to characterise the full range of conditions that were investigated in the whole series of experiments. Cases 1 and 5 represent bimodal spectra with a low-frequency first peak (around 0.4 Hz) resp. a higher-frequency first peak (around 0.8 Hz). The second peak is at 1.0 Hz for both cases. Cases 20 and 31 are a gentle and broad ($T_p = 1.0$ s; $\gamma_p = 3.3$) resp. a steep and narrow ($T_p = 2.5$ s; $\gamma_p = 100$) spectrum. The results of these calculations were analysed and used in the succeeding discussions. For his contributions to this process, the present author has been listed as co-author of the manuscript that was submitted to the Coastal Dynamics conference.

^h See chapter 7 and Smith (2004) for more details on these measurements.

5 Implementation

The DCTA was implemented by N. Booij in an experimental version of the spectral wave model SWAN (Booij et al., 1999) before the start of this study. As the formulation of the DCTA changed throughout the project, the code has been updated and its computational efficiency improved by the present author.

SWAN is a third generation numerical wave model that solves an Eulerian wave action balance equation using, in contrast to many similar models, implicit numerical schemes for the geographical propagation of wave action. The geographical grid that is used in the present study is regular with constant mesh sizes Δx and Δy , the spectral space contains directional bins $\Delta\theta$ on a regular grid and frequency bins $\Delta\sigma$ with a logarithmic distribution (i.e., with a constant relative frequency resolution $\Delta\sigma/\sigma$). The continuous integral ($\int \dots d\sigma$) in the formulation of the DCTA (equation 4-6) is replaced with the discrete sum ($\sum \dots \Delta\sigma$) of all the contributions from all frequencies σ_2 to the source term of σ_1 .

The DCTA was implemented in SWAN identical to the method for the triad interactions source term described in the technical documentation of SWAN (SWAN-team, 2008) and Booij et al. (1999). To obtain a solution for a wave problem, it is written as a linearized set of equations ($AN = b$) and solved iteratively. As all source terms can be written as a quasi-linear term ($S = \phi N$), they can be approximated either explicitly or implicitly by multiplying with the action density at the current resp. the prior iteration level. Each source terms has been separated in positive and negative contributions to the wave component under consideration. The positive contributions are evaluated explicitly and any negative contributions are approximated implicitly.

The triad interaction source term, according to the DCTA, can be rewritten as

$$S_{n|3}^N(\sigma_1)^n = \left[\chi_2^{n-1} N(\sigma_2)^{n-1} - \chi_1^{n-1} N(\sigma_1)^n \right] \quad \text{Equation 5-1}$$

with $\chi_i = \chi N(\sigma_3) \sigma_i c_{g,i} k_i^p d\sigma_2$ and n is the iteration step. The first, positive part was evaluated explicitly, using values of χ_2 and $N(\sigma_2)$ from the prior iteration, and added to the right hand side vector b . The second, negative part was approximated implicitly by adding it, without the minus sign and $N(\sigma_1)$, to the

main diagonal of matrix A . As such, it was multiplied with the action density at the current iteration level when the system is solved. The subroutine with the implementation of the DCTA is listed in appendix A.

6 Validation

Expected behaviour

The DCTA behaves as a relaxation model that converges the action density spectrum towards the universal shape $N(\sigma) \propto \sigma^{-1} c_g^{-1} k^{-p}$, by removing any deviation from this shape through interactions with (near-) resonating frequencies. This can be illustrated by investigating the value of the source term for the interaction between two fixed frequencies σ_1 and σ_2 (thus removing the integral, equation 6-1).

$$S_{nl3}^N(\sigma_1) = \chi N(\sigma_3) \left[\sigma_2 c_{g,2} k_2^p N(\sigma_2) - \sigma_1 c_{g,1} k_1^p N(\sigma_1) \right] d\sigma_2 \quad \text{Equation 6-1}$$

The direction of the transfer of action between σ_1 and σ_2 , and the sign of the source term, depends on the expression between the straight brackets. The action density spectrum is in complete equilibrium if both sides within the brackets are equal for all σ_1 and σ_2 , i.e. if $\left[\sigma_2 c_{g,2} k_2^p N(\sigma_2) - \sigma_1 c_{g,1} k_1^p N(\sigma_1) \right] = 0$. If the left side $\sigma_2 c_{g,2} k_2^p N(\sigma_2)$, is larger than the right side $\sigma_1 c_{g,1} k_1^p N(\sigma_1)$, the sign of the source term will be positive, indicating that action will be transferred from σ_2 to σ_1 .

It must be noted that, although SWAN calculates the *action* transfers between various frequencies, the results of simulations are given in this report in terms of wave *energy*; a more tangible quantity. In the remainder of this report, we will talk about energy densities and transfers. If the energy density spectrum is scaled according to equation 6-2, the direction of energy transfer can easily be deduced from the shape of the scaled spectrum $G(\sigma)$. A spectrum that complies with the universal shape $E(\sigma) \propto \alpha c_g^{-1} k^{-p}$ is transformed into a straight, horizontal line (equation 6-3 and figure 6-2).

$$G(\sigma) = E(\sigma) \cdot c_g k^p \quad \text{Equation 6-2}$$

$$G(\sigma)_{\text{equilibrium}} = \alpha c_g^{-1} k^{-p} \cdot c_g k^p = \alpha \quad \text{Equation 6-3}$$

If the energy density at any σ_1 is out of equilibrium with a second frequency σ_2 (figure 6-3), the transformed spectrum shows that the energy density at σ_1 is *above* the equilibrium (figure 6-4). The expression in the brackets becomes smaller than one, and the sign of the source term for frequency bin σ_1 will be negative. This means that energy is transferred *from* σ_1 to σ_2 and the spectrum is pushed towards

the equilibrium shape. The typical harmonic frequency peaks (chapter 3) appear if the action densities at the peak frequency and twice the peak frequency are in a similar manner out of equilibrium.

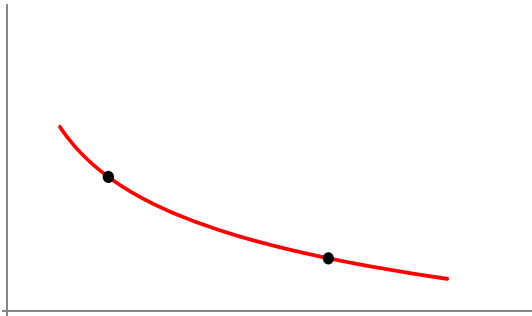


Figure 6-1: Schematic energy density spectrum $E(\sigma)$, in equilibrium

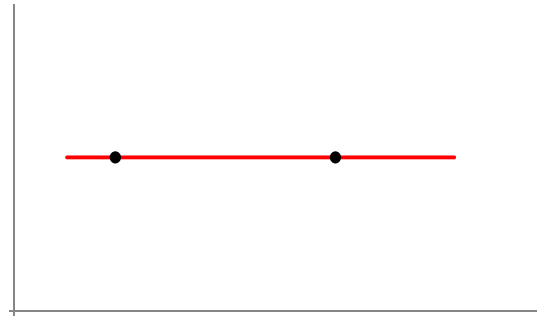


Figure 6-2: Scaled schematic energy density spectrum $G(\sigma)$, in equilibrium

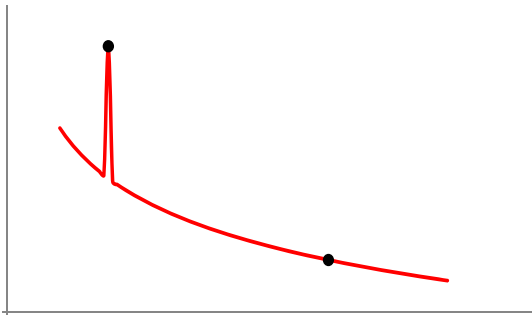


Figure 6-3: Schematic energy density spectrum $E(\sigma)$, out of equilibrium

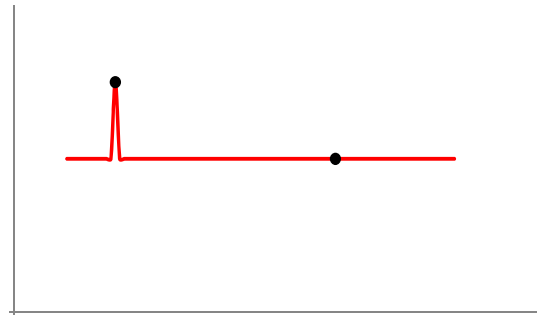


Figure 6-4: Scaled schematic energy density spectrum $G(\sigma)$, out of equilibrium

Validation with simple bathymetries

To validate whether the DCTA performs the expected behaviour, it was applied to three simple one-dimensional bathymetries under various conditions. First, we looked at the model's performance on flat bottoms with three different water depths, then we turned to a straight 1:100 slope and we ended with a one-dimensional version of a tidal inlet. SWAN was in all cases run with default settings (no deepwater source terms, with default wave-induced setup, white-capping and depth-induced breaking dissipation) and the tuning parameter of the DCTA λ was set to one. Although it is normally done by default in SWAN, a diagnostic tail was not included in the calculation of parameters since its *shape* is not influenced by the DCTA.

Flat bottom cases

A JONSWAP spectrum (H_{m0} 1.0 m; T_p 10.0 s; σ_θ 5.7°) was applied to a flat stretch of bottom of 11 km with three different water depths (60.0, 6.0 and 0.6 m) with $H_{m0} = 4\sqrt{m_0}$ and σ_θ according to Kuik et al. (1988). The 60 m case showed that the DCTA is not active in deep water and the spectral parameters identical constant throughout the entire domain (figure 6-5). Reducing the water depth to 6.0 m did activate the DCTA as could be derived from the reduction of the mean period, which was a result of the transfer of energy to higher frequencies. The significant wave height was more or less constant except for a little shoaling (figure 6-6).

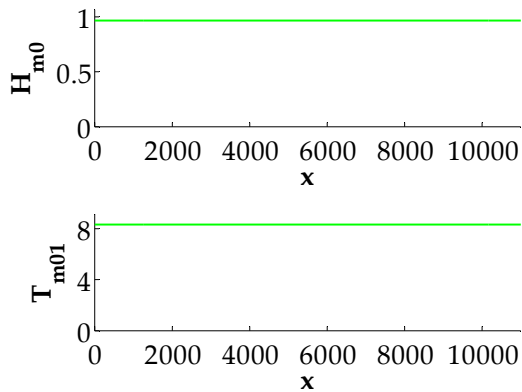


Figure 6-5: Spectral parameters flat bottom case, 60 m water depth

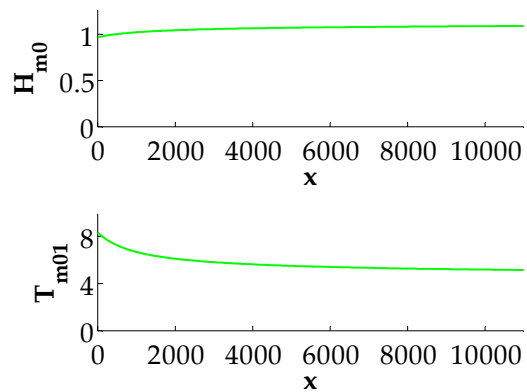


Figure 6-6: Spectral parameters flat bottom case, 6 m water depth

A water depth of 0.6 m cannot sustain a significant wave height of 1.0 m and a sharp reduction of the wave height occurred right behind the up-wave boundary, due to wave breaking (figure 6-7). The largest energy transfer due to triad interactions and the corresponding reduction of T_{m01} took place right at the beginning of the domain.

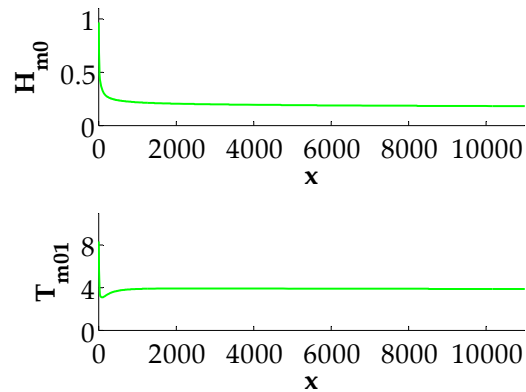


Figure 6-7: Spectral parameters flat bottom case, 0.6 m water depth

The spectra in 60 m water depth confirmed that the DCTA was not activated under these conditions. Throughout the entire domain, the spectra were constant, as were the parameter values (figure 6-8 and figure 6-9).

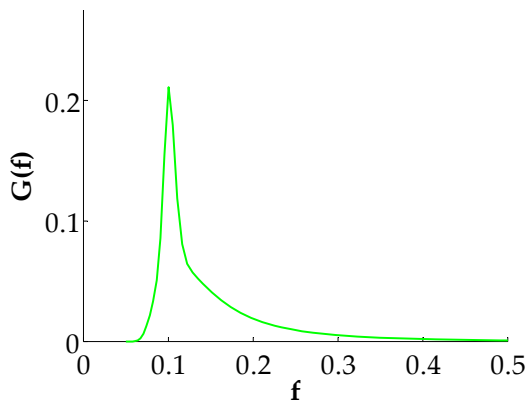


Figure 6-8: Scaled spectrum flat bottom case, 60 m water depth, 1.000 m from up-wave boundary

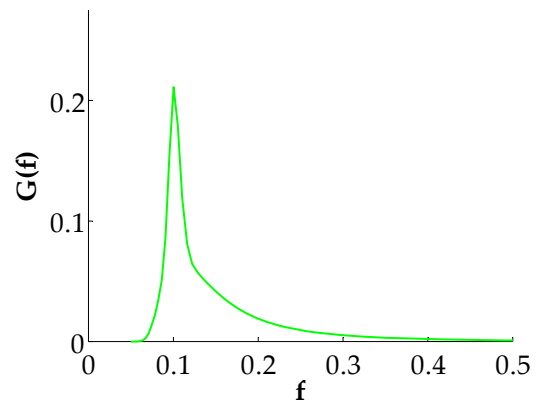


Figure 6-9: Scaled spectrum flat bottom case, 60 m water depth, 10.000 m from up-wave boundary

In figure 6-11, it can be seen that the DCTA was able to create higher harmonic frequency peaks at all multiples of the peak frequency (the first, second and third are visible at multiples of 0.1 Hz). From the horizontal orientation of the (scaled) tail of the spectrum, we found that the model indeed created a spectral tail with k^{-p} -shape. After 10.000 m propagation, the spectrum had not yet completely transformed into the universal shape, indicating that the interactions were not very strong under these conditions.

The transformation towards the equilibrium shape was not achieved for the whole spectrum instantaneously, but achieved first at higher frequencies and then the rest of the spectrum smoothed for progressively lower frequencies. This is remarkable since waves with high frequencies are the most dispersive, and thus least prone to triad interactions, although all wave components had kd -values well below one, the upper limit of the range of validity of the $k^{-4/3}$ -shape (Smith and Vincent, 2002). The saturation of the spectral tail was attributed to the fact that the action density in the tail was generally low and deviations from the universal shape small. The amount of action that had to be transferred towards these frequencies in order to reach the equilibrium was thus accordingly small.

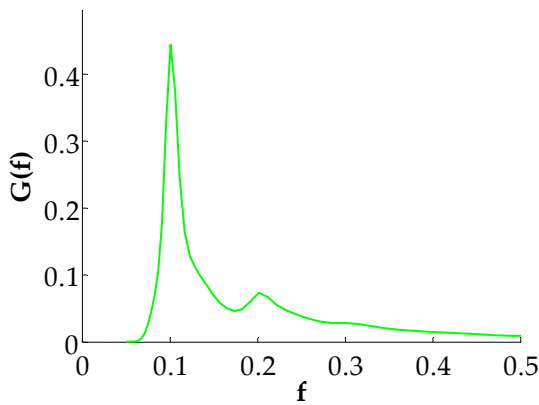


Figure 6-10: Scaled spectrum flat bottom case, 6 m water depth, 1.000 m from up-wave boundary

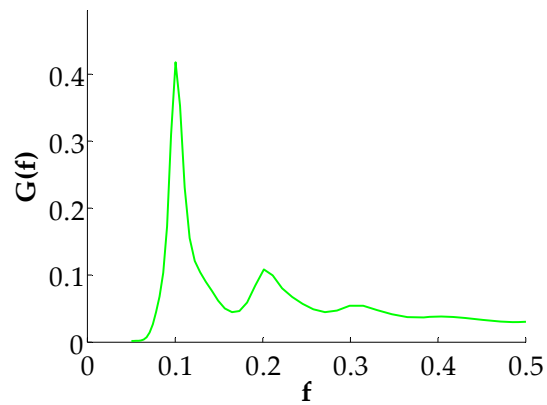


Figure 6-11: Scaled spectrum flat bottom case, 6 m water depth, 10.000 m from up-wave boundary

The transformation towards the universal spectrum of the same incident spectrum, occurred much quicker in 0.6 m water depth than in 6.0 m (compare figure 6-10 with figure 6-12 and figure 6-11 with figure 6-13, yet note the differences in the vertical scales). This might have been due to either the scaling of the DCTA (equation 4-7), which is inversely proportional to the depth squared (and is thus 100 times stronger in 10 times shallower waterⁱ) or the strong dissipation which reduced the quantities of energy that had to be transferred through the spectrum in order to arrive at the equilibrium shape.

ⁱ This is only approximately true since the scaling also depends on the estimate of the local Ursell number, which in turn depends on the inverse water depth cubed, but this dependency is much weaker due to the tangent hyperbolic in the expression of the parameterized bi-phase (end of chapter 4).

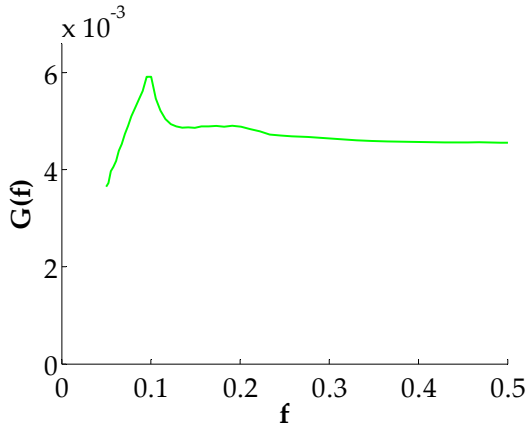


Figure 6-12: Scaled spectrum flat bottom case, 0.6 m water depth, 1,000 m from up-wave boundary

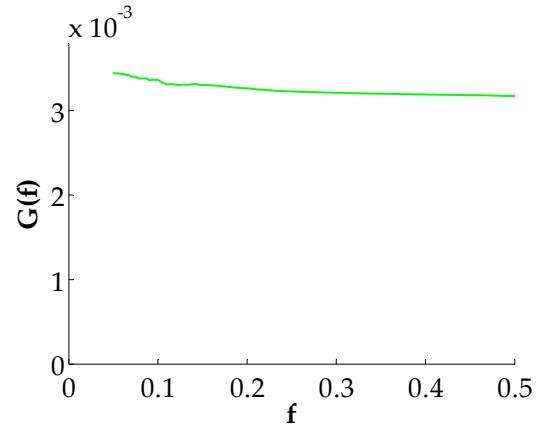


Figure 6-13: Scaled spectrum flat bottom case, 0.6 m water depth, 10,000 m from up-wave boundary

Constant slope cases

Next, we propagated the same incident JONSWAP spectrum (H_{m0} 1,0 m; T_p 10,0 s; σ_θ 5.7°) over a constant 1:100 slope that started at 11 m water depth and stretches over 11.000 m (figure 6-14). Additionally, a bimodal spectrum was run (H_{m0} 1.0 m; $T_{p,1}$ 10.0 s; $T_{p,2}$ 4.0 s; σ_θ 5.7°) that was constructed by superposing two unimodal JONSWAP spectra, each contributing half of the total energy.

The parameters (figure 6-15 and figure 6-16) were consistent with the result from the flat bottom cases. In the deepest part of the domain, the parameters were constant as no wave breaking dissipation and triad interactions took place. In the middle of the domain, where the water depth is approximately 6 m, the wave heights increased due to shoaling and triad interactions caused the wave period to decrease. The shoaling was less for the bimodal spectrum because more of its energy was located at high frequencies, which are less inclined to shoaling. At the end of the domain, the wave height decreased due to depth-induced breaking consistent with the flat bottom case in 0.6 m water depth. The average wave period on the other hand did not decrease as much since the triad interactions had already transformed the spectrum in the up-wave parts of the domain.

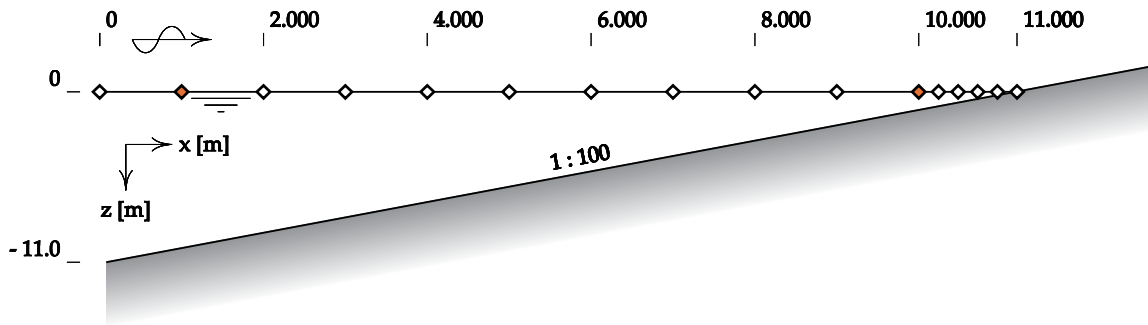


Figure 6-14: Bathymetry constant slope cases

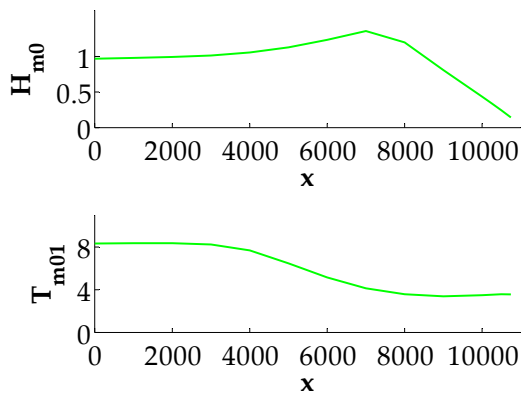


Figure 6-15: Spectral parameters constant bottom case, unimodal spectrum

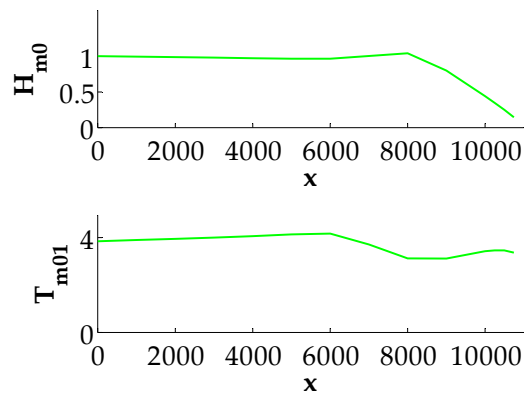


Figure 6-16: Spectral parameters constant bottom case, bimodal spectrum

It can be seen from the spectra (figure 6-17 and figure 6-18), that the results were very similar to the results of the flat bottom case with 6 m water depth, although the transfers were smaller at the beginning of the domain and larger near the waterline. At the end of the domain, the spectra had almost completely transformed to smooth, featureless shapes although the orientation of the tail was not exactly horizontal. The upward orientation of the tail showed that the energy densities at lower frequencies are less than the equilibrium levels. The upwards tail did not entail a strong increase of energy towards higher frequencies since the vertical scale was reduced greatly (more than 15-fold). The spectra from the bimodal case showed that the high frequency peak (no longer visible at distance 10.000 m) was removed much quicker than the low frequency peak (still visible) which agreed with the observations by Smith and Vincent (1992). Again, the tail was not horizontal but oriented upwards.

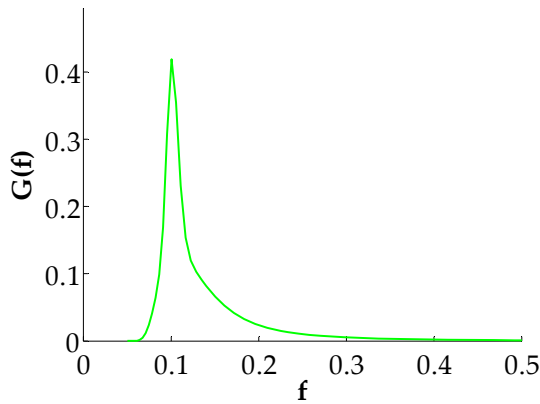


Figure 6-17: Scaled spectrum constant slope case, unimodal spectrum, 1.000 m from up-wave boundary

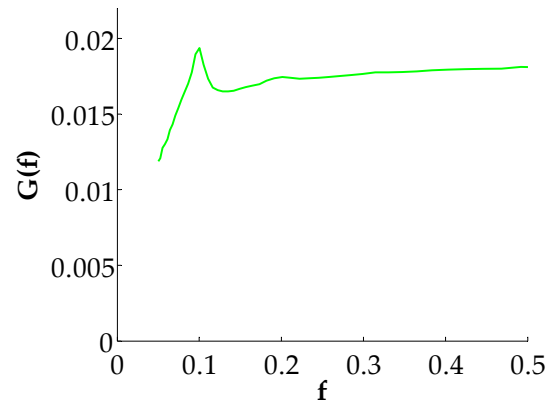


Figure 6-18: Scaled spectrum constant slope case, unimodal spectrum, 10.000 m from up-wave boundary

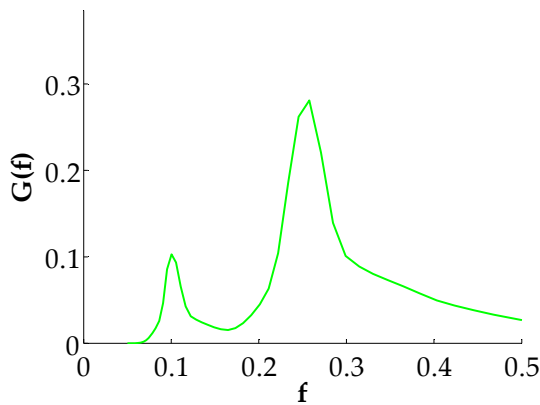


Figure 6-19: Scaled spectrum constant slope case, bimodal spectrum, 1.000 m from up-wave boundary

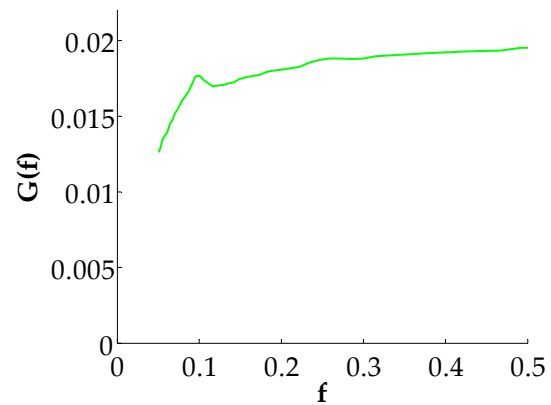


Figure 6-20: Scaled spectrum constant slope case, bimodal spectrum, 10.000 m from up-wave boundary

Tidal inlet case

Applying the model to a more complex bathymetry with the typical scales of a tidal inlet gave us an idea of the model's ability to smoothen the peaks at the inner part of the inlet after the generation of harmonic peaks at the ebb tidal delta. We have taken a linear transect through the Amelanders Zeegat (figure 6-21) and smoothened it somewhat without distorting the length or depth scales. A JONSWAP spectrum (H_{m0} 1.0 m; T_p 10.0 s; σ_θ 5.7°) was applied at the seaward boundary.

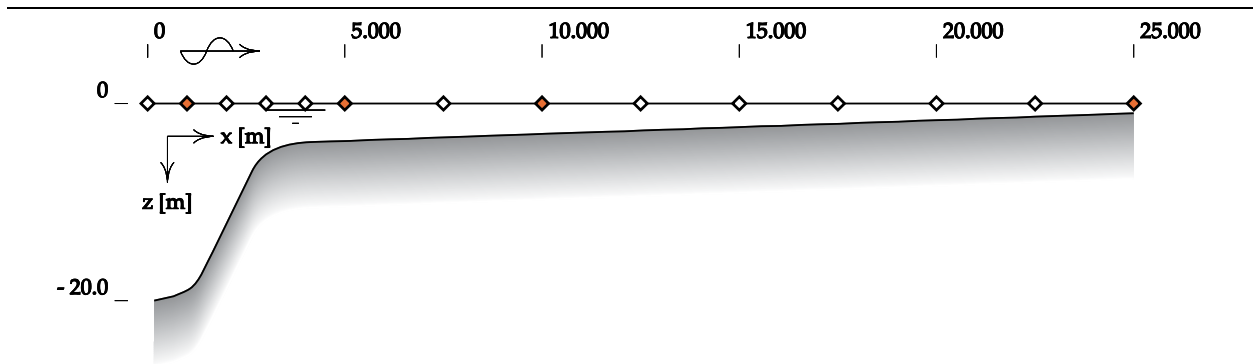


Figure 6-21: Bathymetry tidal inlet case

In figure 6-22 through figure 6-25, the spectra of the simulation with the LTA (blue) and the DCTA (green) at four locations (at 1, 5, 10 and 25 kilometre from the up-wave boundary) are presented. The results indicated that the depth greatly influenced the strength of interactions. In the deeper parts no harmonic peaks appeared (figure 6-22), but once the depth is reduced, the effects of triad interactions were much more pronounced (figure 6-23). Behind the steep decrease of depth, the peaks slowly disappeared in the shallow parts of the domain (figure 6-24 and figure 6-25).

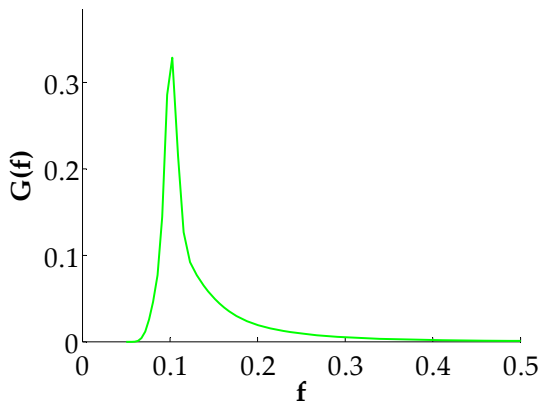


Figure 6-22: Scaled spectrum tidal inlet case, 1.000 m from up-wave boundary

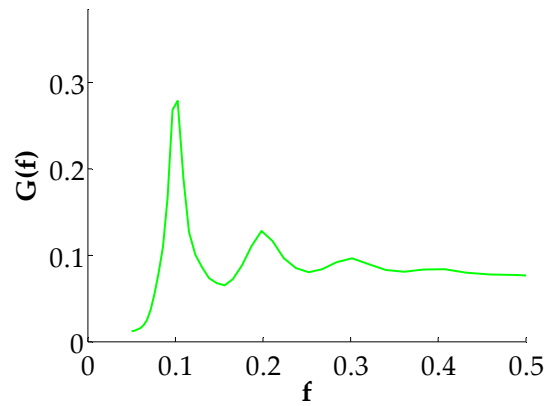


Figure 6-23: Scaled spectrum tidal inlet case, 5.000 m from up-wave boundary

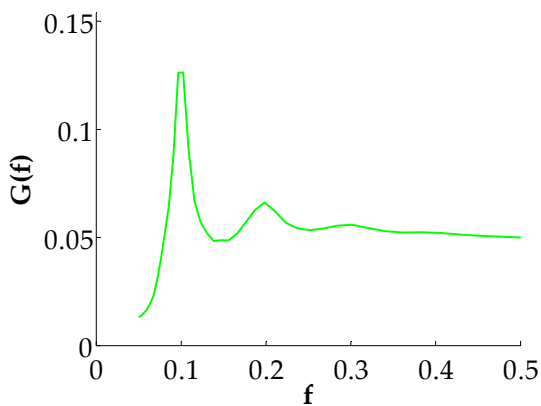


Figure 6-24: Scaled spectrum tidal inlet case, 10.000 m from up-wave boundary

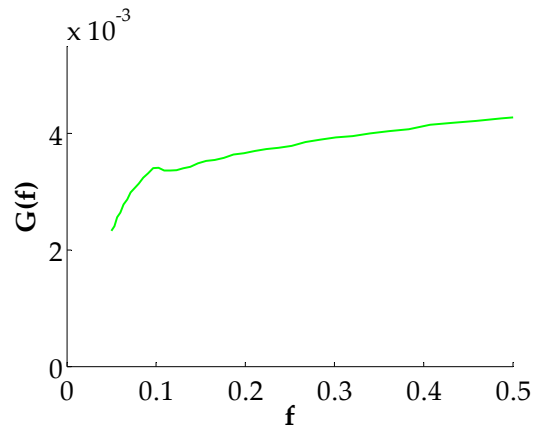


Figure 6-25: Scaled spectrum tidal inlet case, 25.000 m from up-wave boundary

7 Calibration

Method

The value of the tuneable coefficient λ in the formulation of the DCTA was calibrated with measurements from Smith (2004) of waves evolving over a flat, sloping (1:30) bottom. These measurements were considered suitable because the presence of triad interactions could be clearly seen from the emergence of peaks in the spectra at twice the peak frequency and the transformation of the high frequency tail towards a smooth shape near the waterline. The universal shape of the spectral tail was previously confirmed through analysis of these measurements by Smith and Vincent (2003).

The measurements were carried out in a flume that was 0.45 m wide, 0.9 m deep and 45.7 m long with a flat bottom in front of a slope (1:30) that began 21 m from the wave generator. A total number of 10 capacitance wave gauges were installed, the first at a distance of 6.7 m from the wave maker, the others along the slope at depths of 0.30, 0.24, 0.21, 0.18, 0.15, 0.12, 0.09, 0.07 and 0.05 m (figure 7-1). A number of 31 cases with uni- and bimodal spectra were tested during this experiment. The unimodal spectra were TMA spectra (Bouws et al., 1985) and the bimodal spectra were two superposed TMA spectra. Among these, the number of peaks (1 or 2), the peak period of the first peak (between 1 and 2.5 s), the significant wave height (0.06 or 0.09 m) and the spectral peakedness parameter γ_p (3.3, 20 or 100) were varied (appendix B).

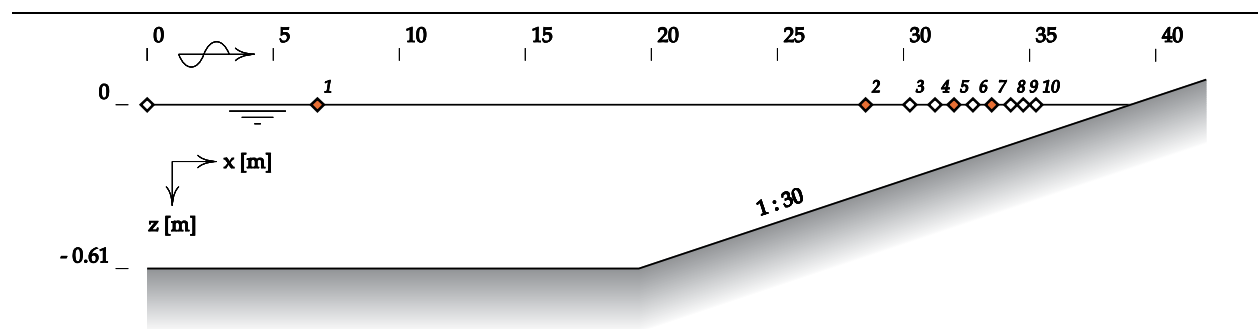


Figure 7-1: Bathymetry Smith measurements

The SWAN simulations were run in one-dimensional mode with the following spatial and spectral resolutions: 0.25 m in x -direction, 10 directional bins in a 20° sector and 100 frequency bins between 0.4

times the peak frequency (this value was specified for each incident spectrum to leave out the influence of sub-harmonic energy transfers) and 3 Hz. These resolutions were chosen to render smooth spectra while not slowing down the computations more than necessary. The calculation of wave setup was included, as were the Battjes-Janssen expression for depth-induced breaking (Battjes and Janssen, 1978) and the JONSWAP bottom friction formulation (Hasselmann et al., 1973); all other source terms were switched off. The measurements at the first location, 6.7 m from the wave maker, were used as boundary conditions to leave out the discrepancy between the target boundary condition and the spectrum that was generated by the wave maker. The distance between the wave maker and the first wave gauge was not included in the modelling domain, which left a flume length of 39.0 m. Remember that the red line always represents measured spectra, the green line DCTA results, the blue line LTA results, the black line results from simulations without the triad interaction source term and all spectra are scaled according to equation 6-2.

Since the triad interactions are an energy conservative process, they should not influence the total amount of wave energy throughout the domain. In the Battjes-Janssen formulation however, they influence the rate of dissipation indirectly through the average frequency of the spectrum, which is affected by triad interactions. The mean rate of dissipation according to the Battjes and Janssen formulation is given in equation 7-1 in which α_{Bj} is a tuneable constant, Q_b the fraction of broken waves and $\bar{\sigma}$ the spectrum average frequency. The maximum wave height H_{max} is defined as the breaker index parameter γ times the local water depth d (equation 7-2).

$$D_{Bj,tot} = -\frac{1}{4} \alpha_{Bj} Q_b \left(\frac{\bar{\sigma}}{2\pi} \right) H_{max}^2 \quad \text{Equation 7-1}$$

$$H_{max} = \gamma d \quad \text{Equation 7-2}$$

Stronger interactions cause a net flow of energy towards higher frequencies, which increases the average frequency and hence the rate of dissipation. The influence between the formulations of the triad interactions and dissipation also operates the other way around. The scaling of the DCTA depends on the local Ursell number, which is affected by the rate of dissipation. A stronger dissipation yields less steep spectra and hence lesser triad interactions. We wanted to remove the influence of an incorrect representation of the dissipation from the calibration of the triad interactions. Therefore, we adjusted the bottom friction coefficient c_f for every case such that the measured and modelled values of H_{m0} were equal at gauge 2, the first gauge on the slope. A joint calibration of both γ (the Battjes-Janssen breaker

index) and λ (the DCTA) was carried out to find values that represent the spectral evolution in the Smith measurements optimally.

The measured and modelled spectra and spectral parameters, $H_{m0} = 4\sqrt{m_0}$ and $T_{m01} = 2\pi m_0 / m_\nu$ were compared at all the measurement locations along the slope for all 31 cases. The optimal values of γ and λ were found through a minimisation of ε , defined as root-mean-square of the difference between the measured and the modelled values (e.g., H_{m0}) at all measurement locations (equation 7-3, with ζ any spectral parameter under consideration, i the measurement location and Z the total number of measurement locations).

$$\varepsilon(\zeta) = \sqrt{\sum_{i=1}^Z \frac{1}{Z} (\zeta_{i,measured} - \zeta_{i,modelled})^2}$$

Equation 7-3

The data from wave gauges 1 and 8 were not included in the calculation of the error values because we used the spectrum of gauge 1 as boundary conditions and the significant wave height at gauge 8 was consistently anomalous. They are not included in any of the parameter graphs of the Smith measurements in this report (although gauge 8 is included as an example in figure 7-2).

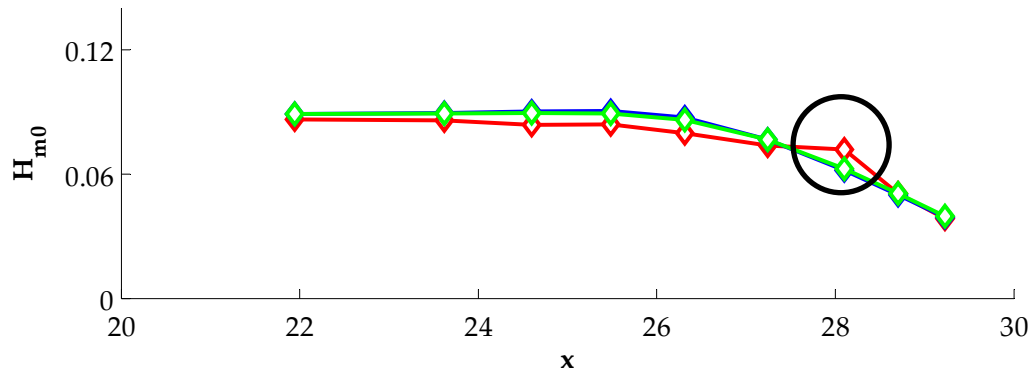


Figure 7-2: H_{m0} Smith case 3, higher value at gauge 8

The calibration method was to minimize for each individual case, the error value of the significant wave height $\varepsilon(H_{m0})$ for a large number of values of λ and γ . From this set of λ , γ and corresponding $\varepsilon(H_{m0})$, the loci of the line of slowest descent of $\varepsilon(H_{m0})$ were determined to find the optimal value of γ for each λ . The minimum error value of the mean wave period $\varepsilon(T_{m01})$ along this line then provided the optimal combination of λ and γ that gives a minimum for both error values. The minimum value of $\varepsilon(H_{m0})$

indicated that the amount of energy in the spectrum was correct, which is affected by the depth-induced breaking, the minimum of $\varepsilon(T_{m01})$ that the distribution of energy within the spectrum was right, which is mainly affected by triad interactions.

Results

The results for each individual case are listed in a table that can be found in appendix C. The average value of c_f for all 31 calibrated cases was $0.11 \text{ m}^2\text{s}^{-3}$, which was larger than the default value for fully developed conditions in shallow water $0.067 \text{ m}^2\text{s}^{-3}$, with a standard deviation of $0.07 \text{ m}^2\text{s}^{-3}$. The values of γ varied between 0.69 and 0.94. The average value of γ was 0.787 (which was a bit larger than the default value of 0.73) while its standard deviation was 0.068.

		λ	$\varepsilon(\mathbf{H}_{m0})$	$\varepsilon(\mathbf{T}_{m01})$
DCTA	Average	0.130	0.0024	0.030
	Standard deviation	0.064	0.0014	0.019
LTA	Average	-	0.0025	0.090
	Standard deviation	-	0.0011	0.030

Table 7-1: Results calibration Smith

The λ -values varied between 0.05 and 0.285 and the average value was 0.130 (table 7-1). The scatter around the average value for all cases was quite large, being about half of the average itself (0.064). This suggested that some fundamental assumptions underlying the basic formulation or the scaling may be wrong. For comparison, the model was also run with the LTA (and furthermore the same settings) which indicated that the error values of T_{m01} were smaller than those with the DCTA (table 7-1). However, bear in mind that a comparison is somewhat unfair because the LTA was not calibrated while the DCTA was. As an example, the results of the steepest unimodal case (31) are given in figure 7-3.

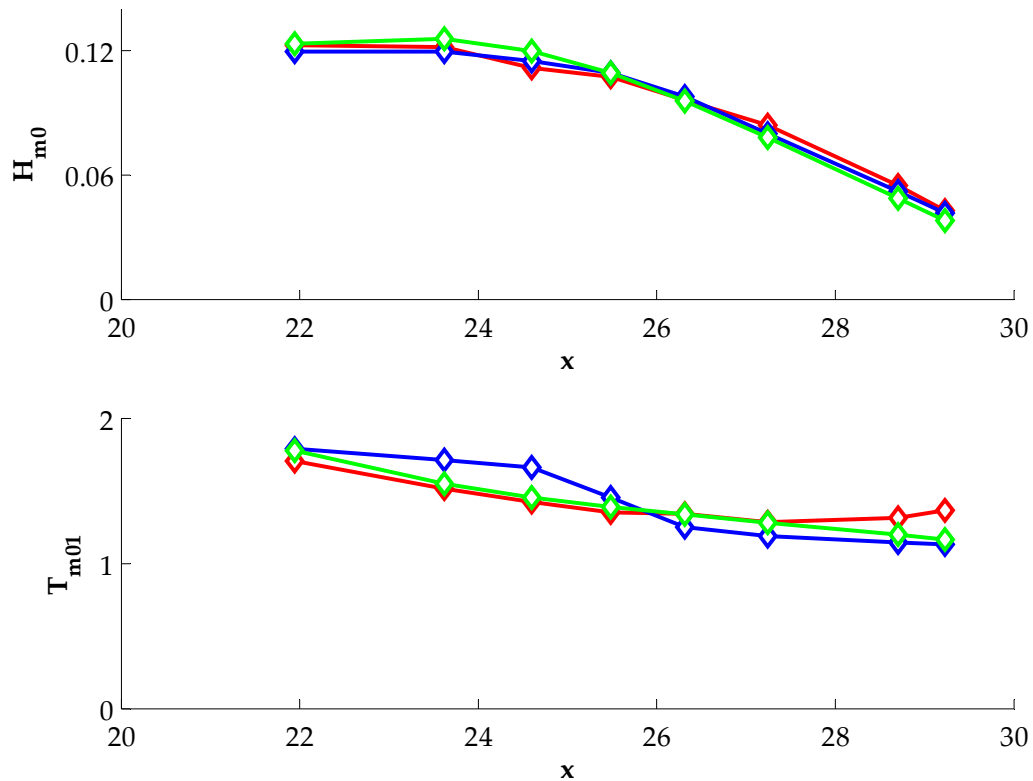


Figure 7-3: Spectral parameters Smith case 31

In figure 7-16 through figure 7-7, a selection of the spectra of four cases is presented. The cases that are presented here are the same as were used for the trial calculations for the formulation of the DCTA (chapter 4) and characterise the full range of conditions in the Smith experiments that were used for the calibration. From these cases, the spectra from four wave gauges (1, 2, 5 and 7) are displayed. The results of the unimodal spectra are discussed first (case 31 and 20) and then those of the more complex bimodal spectra (case 5 and 1). The vertical black lines in figure 7-4 through figure 7-7 indicate the frequency at which $kd = 1$, the upward boundary of the validity of the universal tail shape $k^{-4/3}$ according to Smith and Vincent (2003).

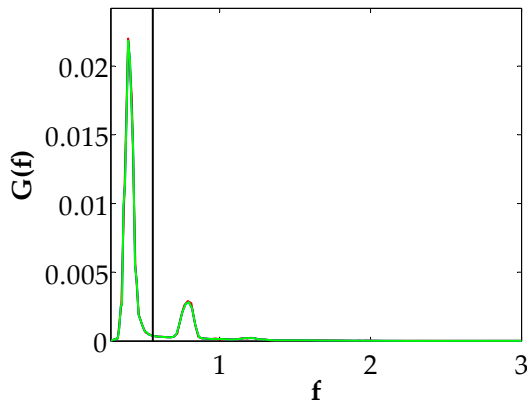


Figure 7-4: Scaled spectra Smith case 31, gauge 1

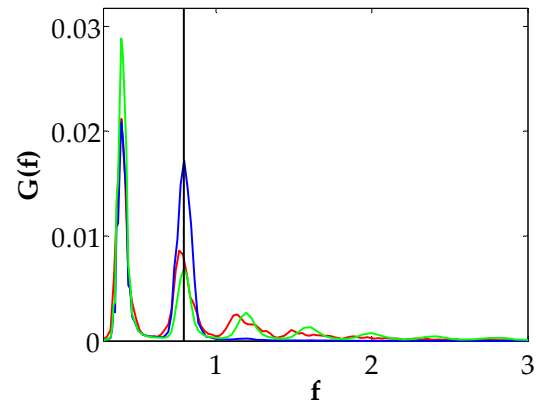


Figure 7-5: Scaled spectra Smith case 31, gauge 2

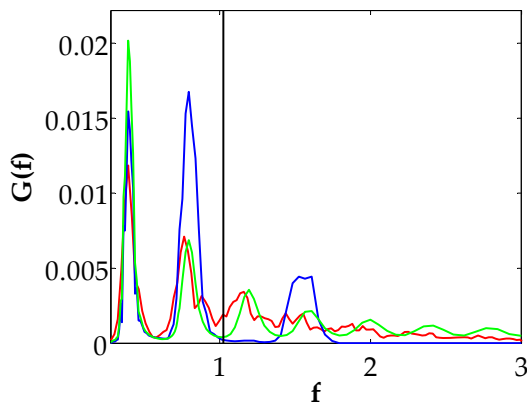


Figure 7-6: Scaled spectra Smith case 31, gauge 5

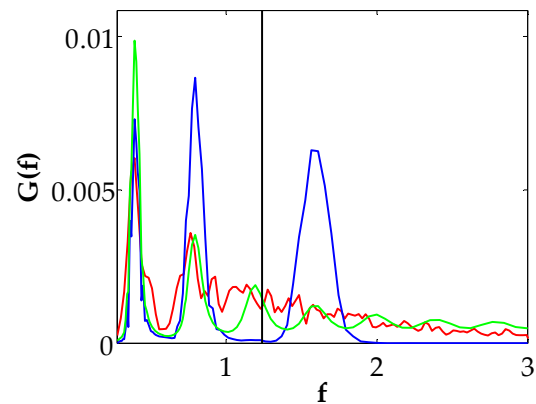


Figure 7-7: Scaled spectra Smith case 31, gauge 7

The narrow and steep unimodal spectra of case 31 (figure 7-4 - figure 7-7) showed that there was already a harmonic component visible in the boundary condition (remember it was taken from measurements at 6.7 m from the wave maker). The steepness of the spectrum invoked strong triad-interactions and the measured spectra broadened and smoothed strongly. The harmonic frequency peaks were very well simulated with the DCTA at the beginning of the slope (figure 7-5), but were more peaked than the measurements at the shallowest locations (figure 7-7). The tail at the shallowest locations was also higher and more horizontal than in the measurements. In addition, too little energy was transferred from the peak to other frequencies and therefore the height of the primary peak was overestimated. The surplus of energy at the peak should have been transferred to frequencies between the harmonic peaks, as we know from the value of H_{m0} in figure 7-3 that the total amount of energy in the spectrum is correct.

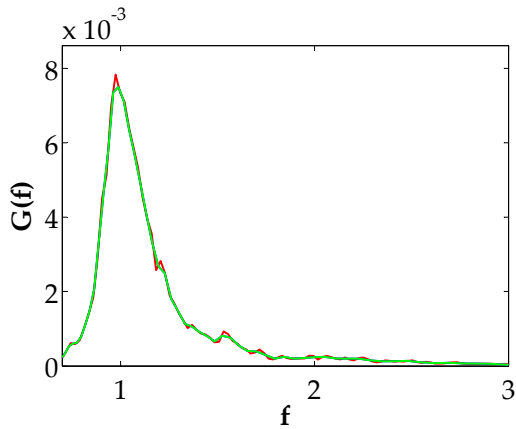


Figure 7-8: Scaled spectra Smith case 20, gauge 1

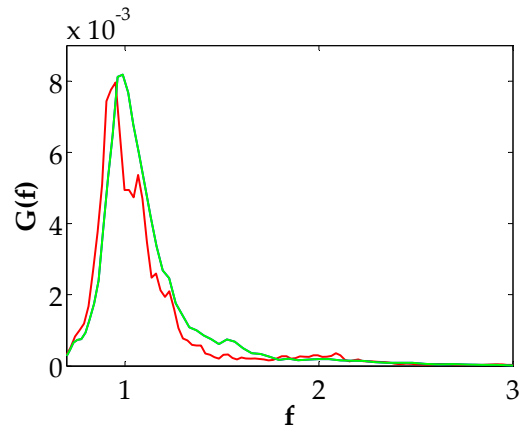


Figure 7-9: Scaled spectra Smith case 20, gauge 2

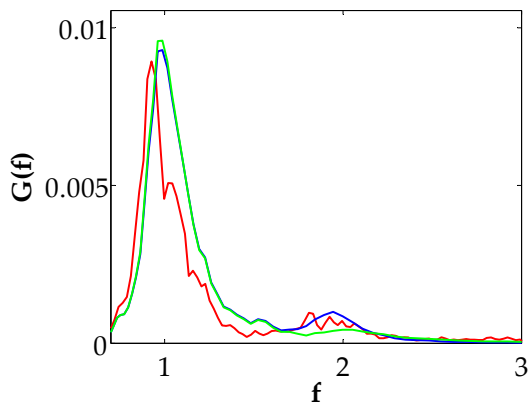


Figure 7-10: Scaled spectra Smith case 20, gauge 5

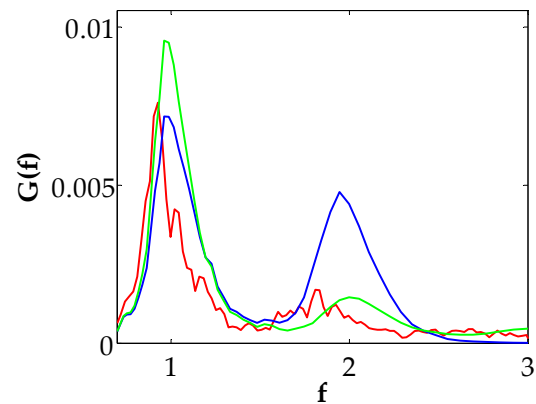


Figure 7-11: Scaled spectra Smith case 20, gauge 7

The broad and gentle unimodal spectra of case 20 (figure 7-12 - figure 7-15) gave a rather different type of results. The decay of the peak was very well calculated with the DCTA and the height of the first harmonic peak was underestimated. The location of the peaks however, was not very well captured by the DCTA. The measurements show that all peaks were shifted towards lower frequencies (from 1 Hz to 0.8 Hz) in shallow water. There is no mechanism in SWAN or the DCTA to reproduce this phenomenon and the peaks remained at the original peak frequency and at multiples thereof.

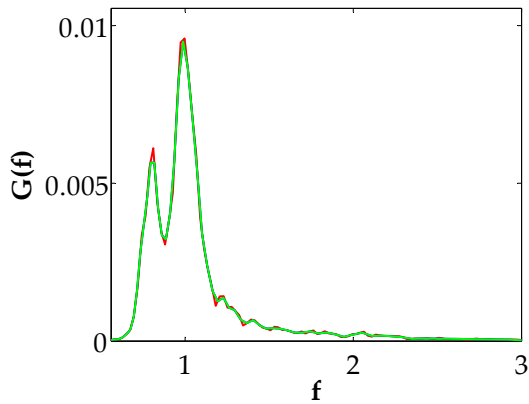


Figure 7-12: Scaled spectra Smith case 5, gauge 1

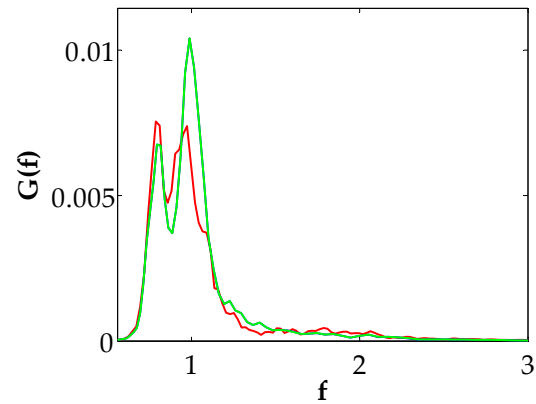


Figure 7-13: Scaled spectra Smith case 5, gauge 2

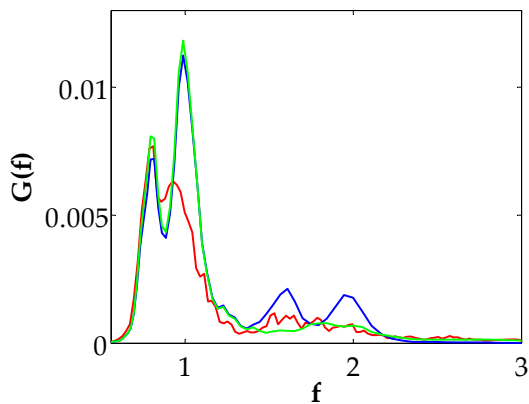


Figure 7-14: Scaled spectra Smith case 5, gauge 5

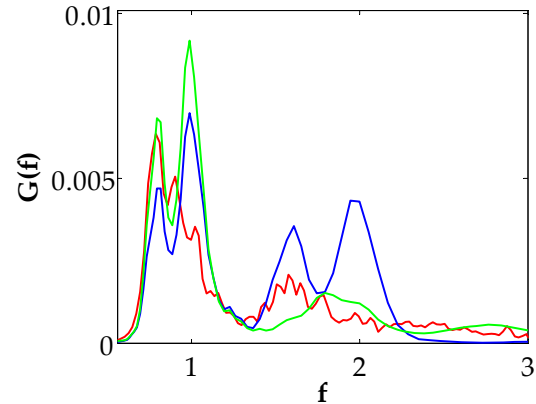


Figure 7-15: Scaled spectra Smith case 5, gauge 7

The peaks of the bimodal spectrum in case 5 (figure 7-8 - figure 7-11) were so close together in frequency, that the spectra in this case were comparable to the broad spectra of case 20. Again, the height of the peak was rather well simulated by the DCTA and the height of the high frequency peaks was a bit underestimated.

In measurement with bimodal spectra on a constant slope, Smith and Vincent (1992) discovered that nonlinear interactions tend to remove the higher frequency peak, irrespective of its size relative to the low-frequency peak and peak period. This preferential decay of the high frequency peak indeed was observed in the DCTA results, although the high-frequency peak did not decay enough (the ratio of the heights of peak 1 over peak 2 was too low). The downshift of the peaks, again, was not represented by the DCTA.

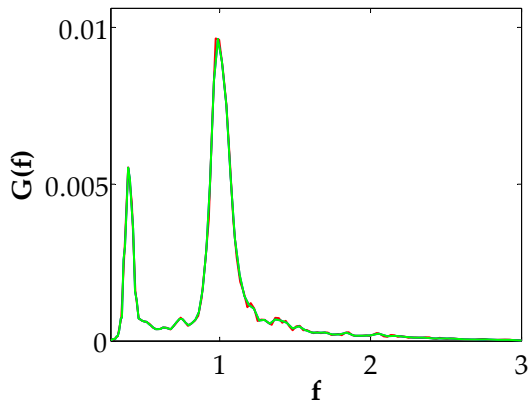


Figure 7-16: Scaled spectra Smith case 1, gauge 1

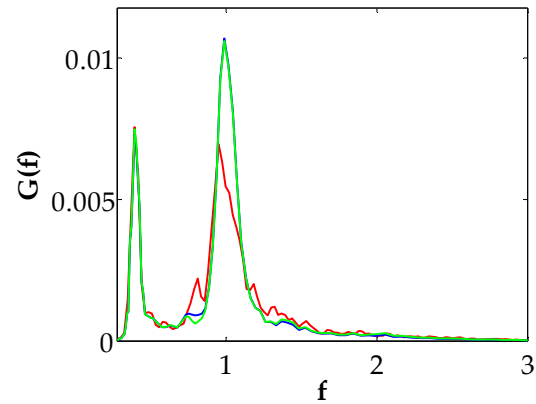


Figure 7-17: Scaled spectra Smith case 1, gauge 2

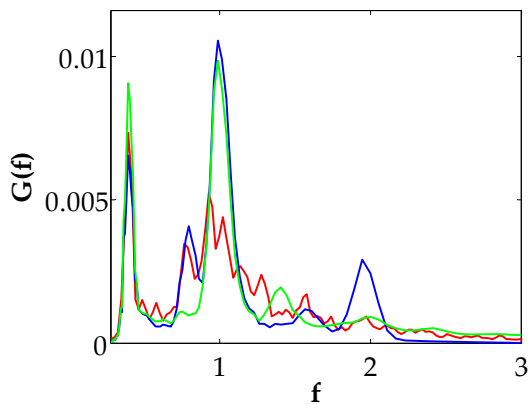


Figure 7-18: Scaled spectra Smith case 1, gauge 5

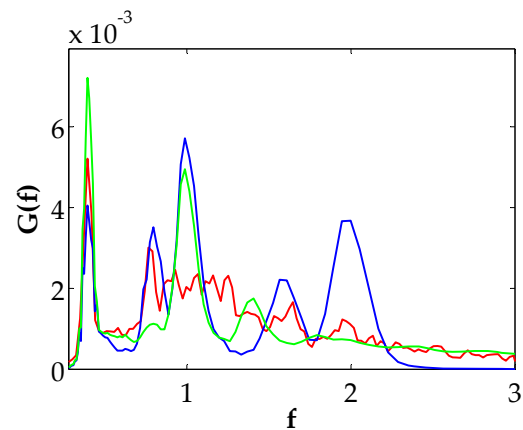


Figure 7-19: Scaled spectra Smith case 1, gauge 7

Case 1 (figure 7-4 - figure 7-7) represented a combination of the behaviour that was seen in case 31 (steep spectrum) and case 5 (bimodal spectrum). As in case 31, the height of the tail that the DCTA produces was more or less correct although it was too high at the highest frequencies. Its shape was more narrow and pronounced than the measurements at intermediate frequencies and the energy density at high frequencies was overestimated. The preferential decay of the high-frequency peak was observed in the DCTA results, although again not strong enough.

The results with the LTA indicated that it strongly overestimated the height of high frequency peaks but that it simulated the decay of the peak better than the DCTA. This could be seen in the results of case 31 and 20. It seemed to be able to infer stronger cross-spectral energy transfers. The preferential decay of the high frequency peak that was observed in case 5 and 1, was not reproduced.

Discussion

In general, we could conclude that the DCTA estimated the general shape of the spectra well. Harmonic peaks evolved and smoothed in shallow water, the lower peaks in bimodal spectra were sustained while the higher peaks disappeared and the tails of the spectra transformed into universal, featureless shapes. Comparison with the LTA showed that the DCTA reproduced the decay of the primary peak poorer. On the other hand, it simulated the growth of the harmonic peaks better as it did not only create peaks at even multiples of the peak frequency and was less prone to overestimating the height of these peaks. In addition, the transformation towards a universal, featureless spectrum and the smoothing of the peaks were very well modelled. Nonetheless, the DCTA overestimated the height of the peak and the height of the tail and did not smooth the shape intermediate frequencies enough.

The overestimation of energy densities at the highest frequencies meant that the DCTA transferred too much energy to the highest frequencies and did not transfer enough towards intermediate frequencies (between the peak frequency and the highest frequency tail). This was unfortunate since it biased the calculation of T_{m01} on which the calibration is based, towards higher values. The highest frequencies were in relatively deep water and had values for kd which were well above one. At the boundary kd was above one for frequencies larger than 0.6 Hz (vertical black line in figure 7-16), and at the shallowest measurement location (of which the spectra are not displayed in this report), kd was above one for frequencies larger than 1.9 Hz. The universal shape, as caused by triad interactions, is only valid for $kd < 1$, and we must draw the conclusion that the DCTA allowed too much triad interaction for dispersive wave components (which are far from resonance).

The overestimation of the energy level of the peak, the underestimation of the heights of the harmonic frequency peaks, and the slow smoothing at intermediate frequencies suggested that the triad interactions in general were not strong enough. The horizontal orientation of the highest part of the spectrum indicated that the spectral levels were saturated and no longer receptive to energy transfers. Higher values of λ could not solve this since that invoked an even larger transfer of energy towards the high frequency part of the spectrum which was already close to equilibrium. Another issue was the location of the peaks in the spectrum. In the measurements, the peaks shifted a little towards lower frequencies when propagating further onshore and the higher harmonics were generated at according lower frequencies. A possible explanation for both the weakness of interaction and the downshift of the peaks may be that the dissipation is not distributed proportionally to the spectral densities, as assumed in

the Battjes-Janssen formulation, but is stronger at higher frequencies. In recent literature, it has been suggested that depth-induced breaking dissipation is proportional to the frequency squared (Mase and Kirby, 1992; Eldeberky and Battjes, 1996; Kirby and Kaihatu, 1996; Chen et al., 1997; Herbers et al., 2000; Kuznetsov and Saprykina, 2004) and white-capping dissipation to the wave number squared (Rogers et al., 2003). Increasing the dissipation at higher frequencies may allow the triad interactions to transport more energy towards this part of the spectrum (Smith and Vincent, 2003) and consequently decrease the height of the primary peak. This would also allow for stronger interactions and accordingly more smoothing of the spectrum without overestimating the energy at the high frequencies, as dissipation is stronger here.

The concept that the distribution of dissipation across the spectrum serves mainly to control the nonlinear transfers of energy was confirmed in the paper of Kirby and Kaihatu (1996). They add in agreement with Chen et al. (1997), that the shape of the predicted spectra is insensitive to the choice for a particular distribution (they tested various dependencies between σ^0 and σ^2) as the nonlinear transfers rapidly compensate dissipation at higher frequencies to transform the spectra into the universal shapes. Wave-shape related statistical parameters (asymmetry and skewness) however, do improve when a σ^2 distribution is applied, which may be related to the suggestion that this is an effect of the transformation of waves towards a sawtooth shape when breaking is established (Kirby and Kaihatu, 1996). The *distribution of dissipation* with σ^2 infers an equilibrium level with the same *spectral shape* (or equivalently k^2 in shallow water) where depth-induced breaking dominates the spectral transformation. Kaihatu et al. (2007) find for a set laboratory observations that the spectral shape moves away from the parameterized shapes that were proposed by Smith and Vincent (2003) and converges towards a σ^2 -shape in the inner surf-zone. Trial calculations with a σ^2 distribution of the dissipation, which are not presented in this report, confirm that the evolution of the spectra converges to the same shapes in the inner surf-zone, but that the evolution of the peaks at the outer surf-zone has improved.

The correlation of the dissipation and triad interactions become also apparent when we made a scatterplot of the values of γ and λ that we found for all 31 Smith cases (figure 7-20). This showed that there is a negative correlation between their values. The effects of depth-induced breaking and nonlinear triad interactions were not independent and a joint calibration was justified. The negative correlation can be reasoned from the formulations. A higher value of λ will invoke stronger triad interactions which will increase the average frequency $\hat{\sigma}$ of the spectrum. As a result, the calculated amount of dissipation with

Battjes-Janssen formulation will increase. To simulate the measured dissipation correctly a lower value for γ is then applied. Vice versa, lower values of γ increase the rate of dissipation, which decreases the steepness of the spectra. The DCTA will therefore decrease the strength of the triad interactions and higher values of λ are required to represent the measured effects of triad interactions.

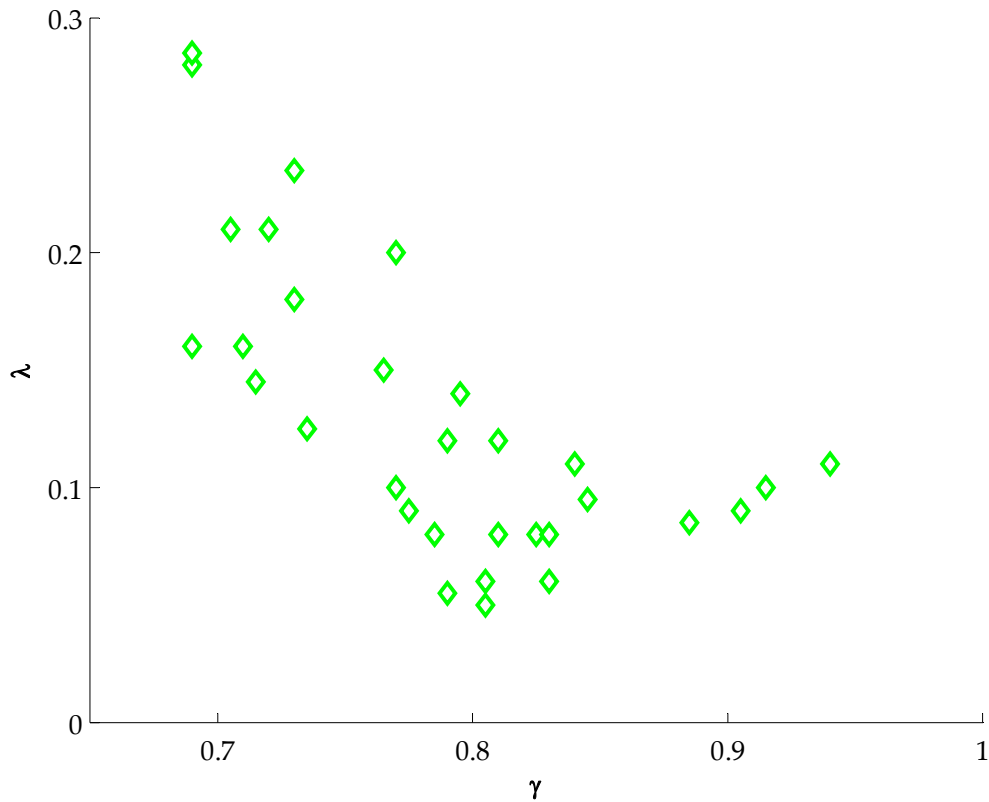


Figure 7-20: Scatterplot $\gamma - \lambda$

8 Verification

To see whether the calibrated DCTA is generally applicable for a wide range of situations, it was tested on a larger set measurements in both lab and field environments, with different bathymetries and of different scales. Again, all red lines represent measured spectra, the green lines DCTA results, the blue lines LTA results, the black line results from simulations without the triad interaction source term and all spectra are scaled according to equation 6-2.

Laboratory measurements

Smith

Instead of calibrating each measurements of Smith (2004) separately, the average value of λ (0.13) was applied to the whole batch for verification of this value. The results with default values for γ (0.73) and c_f (0.067) showed (table 8-1) that the average error value $\varepsilon(H_{m0})$ was rather small for both the DCTA (0.0039 m) and the LTA (0.0038 m). The value $\varepsilon(T_{m01})$ was significantly smaller with the DCTA (0.047 s) than with the LTA (0.086 s) with default settings. Unfortunately, the scatter was very large: the standard deviation of the error values around the mean was 100% of the average error value. The largest error values occurred for cases 30 and 31. These cases have very steep ($T_p = 2.5$ s) and narrow unimodal spectra. In figure 7-4 through figure 7-7, it can be seen that the DCTA already could not reproduce the strong broadening of the spectral tail with the high, calibrated value of λ (0.285). Without these cases, $\varepsilon(T_{m01})$ was reduced with 22% (0.037 s) and the standard deviation with 44% (0.027 s). From the scatter plot of the error values of T_{m01} could be seen that these cases (the encircled values) really enlarged the extent of the cloud and increased the average error value.

		$\epsilon(H_{m0})$	$\epsilon(T_{m01})$	$\epsilon(T_{m01})$ (without case 30 & 31)
DCTA	Average	0.0039	0.047	0.037
	Standard deviation	0.0012	0.048	0.027
LTA	Average	0.0038	0.086	0.082
	Standard deviation	0.0014	0.032	0.028

Table 8-1: Results verification Smith

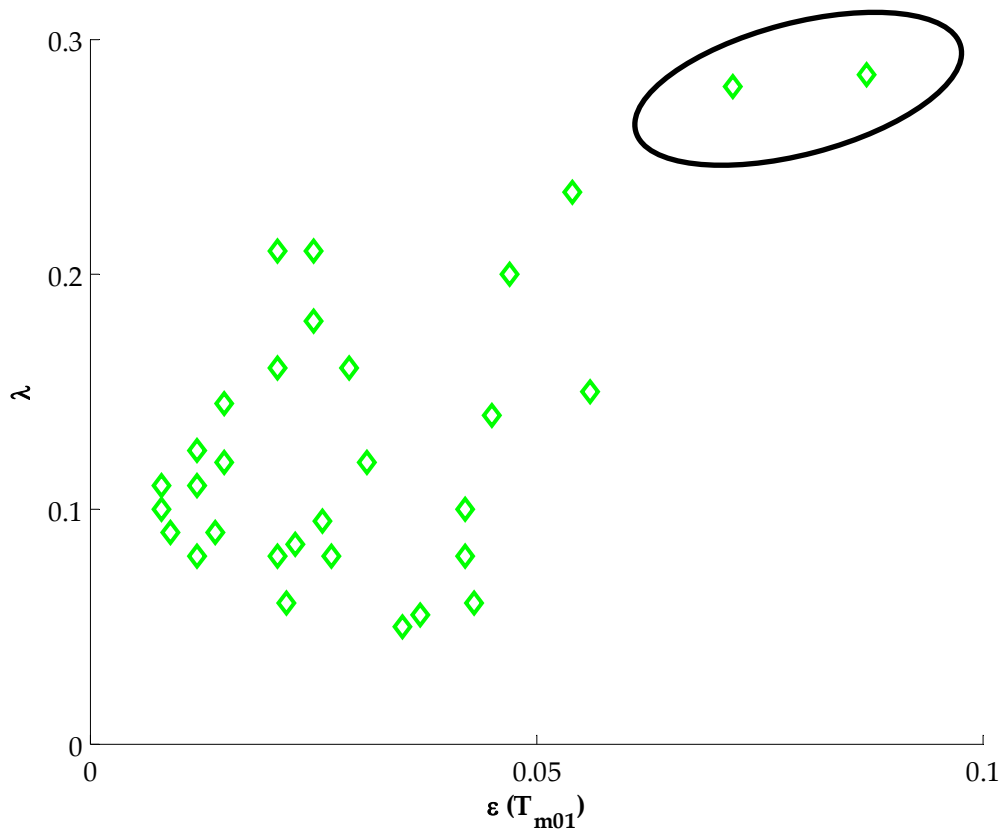


Figure 8-1: Scatterplot $\epsilon(T_{m01}) - \lambda$

Beji-Battjes

In the Beji-Battjes (1993) experiments, spectra were measured at 8 locations along a submerged trapezoidal bar with a 1:20 upslope and a 1:10 down slope (figure 8-2). For the verification of the DCTA the measurements of one, out of originally 66, incident spectra were used, i.e. the case that is included in the ONR testbed (Ris et al., 2002). The incident spectrum was a JONSWAP shape with a peak frequency of 0.5 Hz and H_{m0} was 0.23 m. The measurements showed a decrease of the peak energy, a broadening of the spectrum and the appearance of a harmonic peak at twice the peak frequency. Unfortunately, the spectra behind the bar were not measured and we could not see whether the harmonic peaks disappeared and the tail transformed into a smooth shape. Since measurements from this experiment were used to calibrate the LTA (Eldeberky, 1996), it is expected that the LTA is able to represent these measurements very accurately.

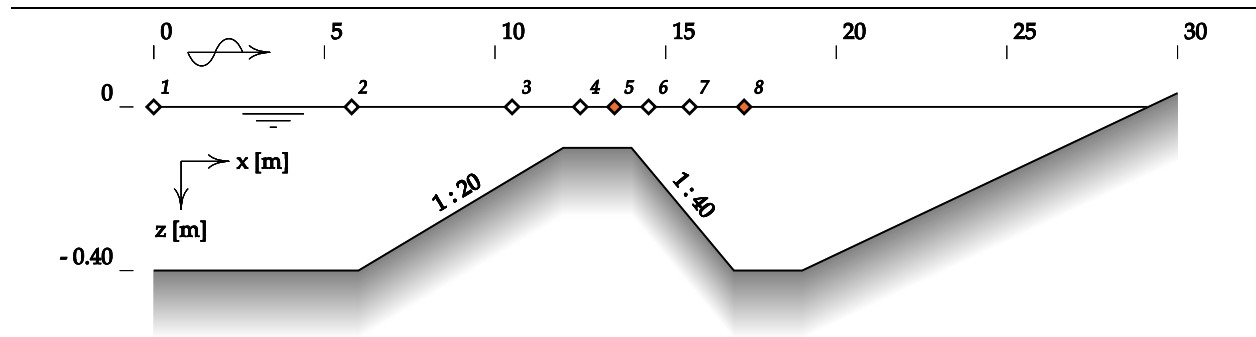


Figure 8-2: Bathymetry Beji-Battjes measurements

For convenience, the default settings of SWAN in the ONR testbed were also applied in this study. SWAN was run in one-dimensional mode on a grid that had 300 nodes in a 30 m geographical domain, 40 directional bins in a sector of 20° and a 40 logarithmically distributed frequencies between 0.0837 and 2.5 Hz. The source terms for wind growth, white-capping and quadruplet interactions were switched off, those for wave-induced setup, breaking, bottom friction run in default mode. The results of the default SWAN with LTA and with the DCTA ($\lambda = 0.13$) were compared (table 8-2).

	$\epsilon(H_{m0})$	$\epsilon(T_{m01})$
DCTA	0.0016	0.105
LTA	0.0019	0.059

Table 8-2: Results verification Beji-Battjes

The parameters indicated that the increase of H_{m0} over the bar, due to shoaling, was too large in both the LTA and the DCTA results. The error values of H_{m0} were more or less equally good, but the T_{m01} error values of the LTA were better (table 8-2). Above the bar, both models overestimated the value of T_{m01} , but the LTA less than the DCTA. Behind the bar, the DCTA seemed to yield better results, though not many measurements were done in this part of the domain.

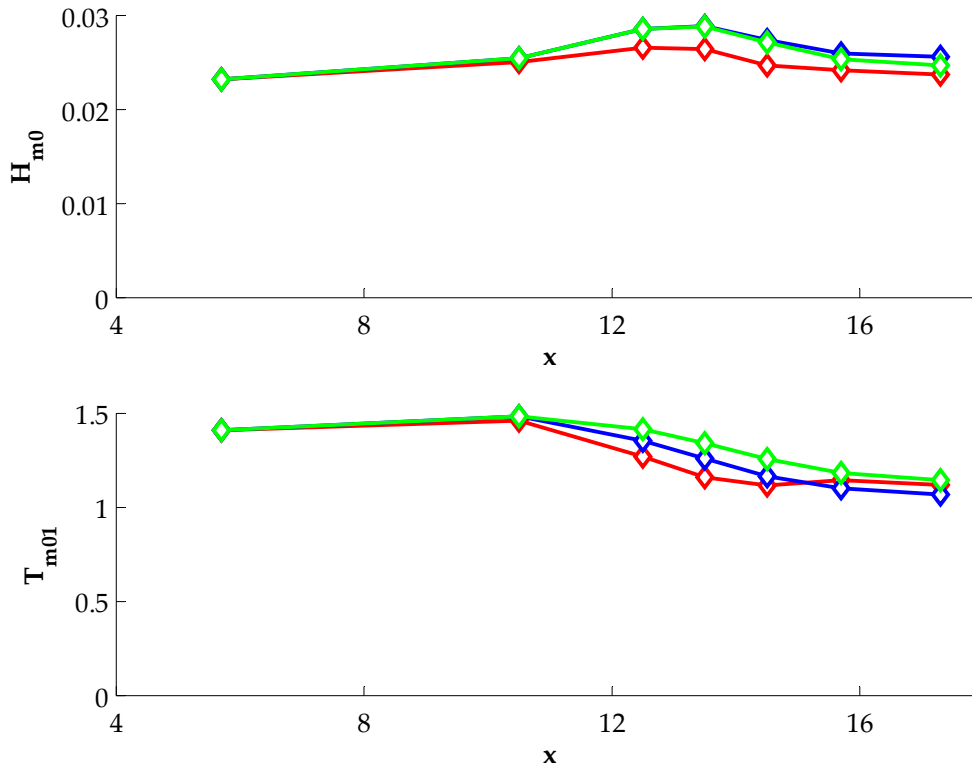


Figure 8-3: Spectral parameters Beji-Battjes

The spectra (figure 8-4 and figure 8-5) showed that the LTA reproduced the decrease of the peak energy and generation of the first harmonic very nicely whereas the DCTA under-predicted the decay of the primary peak and the generation of the first harmonic peak. The amount of energy in the high frequency part of the spectrum, again, was overestimated by the DCTA. The LTA produced a higher harmonic peak at 2 Hz, which is not visible in the measurements while the DCTA created a smooth tail. It is very understandable that the LTA does not account for the smoothing of energy since this was not observed in these measurements, which were used for its calibration.

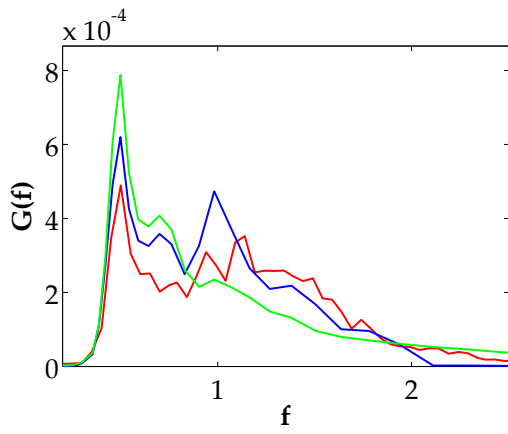


Figure 8-4: Scaled spectra Beji-Battjes, gauge 5

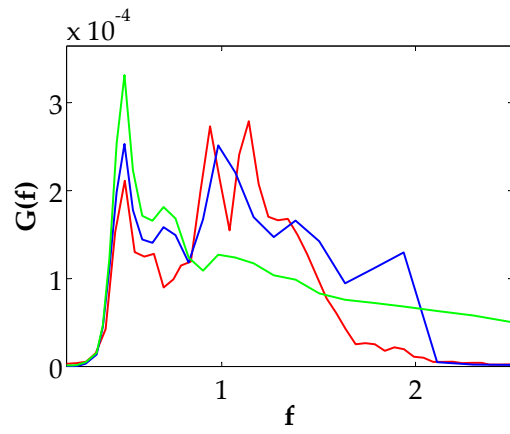


Figure 8-5: Scaled spectra Beji-Battjes, gauge 8

Boers

Boers (2005) measured the evolution of three random, unimodal incident spectra (figure 8-7 - figure 8-9) in a flume of 40 m length, 0.8 m width and 1.05 m height. For every incident spectrum, a total number of 69 spectra were measured along an irregular slope (figure 8-6). The three measurements (figure 8-7 through figure 8-9) were included in the ONR testbed (Ris et al., 2002) and their characteristics are listed in table 8-3.

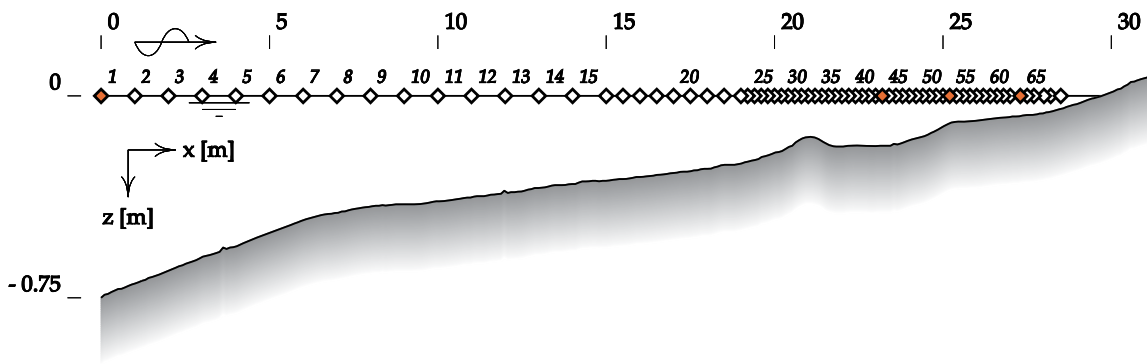


Figure 8-6: Bathymetry Boers measurements

Case	H_{m0}	T_p
1	0.160	2.1
2	0.220	2.1
3	0.107	3.4

Table 8-3: Boers measurements

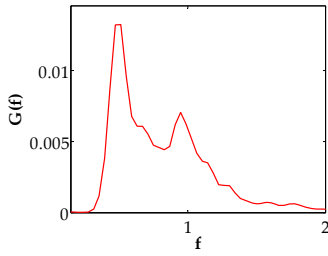


Figure 8-7: Scaled initial spectrum
Boers case 1

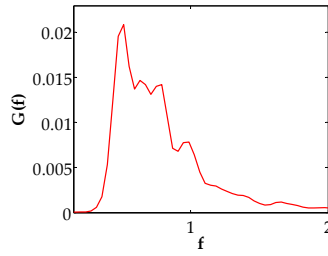


Figure 8-8: Scaled initial spectrum
Boers case 2

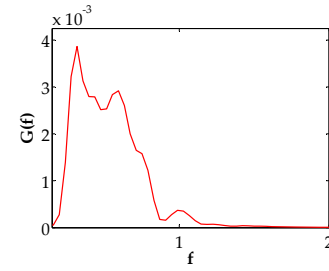


Figure 8-9: Scaled initial spectrum
Boers case 3

Again, the settings from the ONR testbed were applied for this study. SWAN was run in one-dimensional mode on a grid that had 313 nodes in a 31.3 m geographical domain, 30 directional bins in a sector of 15° and a 53 logarithmically distributed frequencies between 0.15 and 2.5 Hz. The source terms for wind growth, white-capping and quadruplet interactions were switched off and the source terms for wave-induced setup, breaking, bottom friction run in default mode. The results of the default LTA and the DCTA with $\lambda = 0.13$ were compared.

The results of the first incident spectrum are presented in this report as a typical example of the results for the Boers case. The parameters in figure 8-10 showed that the significant wave heights were accurately reproduced with default SWAN and the DCTA. The simulated average wave periods were also good, except for the very shallow locations. An overview of the error-value results is given in table 8-4. The DCTA clearly improved the predicted mean wave period values as the error-value was 35% smaller compared to the result with the LTA.

		$\varepsilon(\mathbf{H}_{m0})$	$\varepsilon(\mathbf{T}_{m01})$
DCTA	Average	0.007	0.125
	Standard deviation	0.002	0.050
LTA	Average	0.007	0.194
	Standard deviation	0.003	0.050

Table 8-4: Results verification Boers

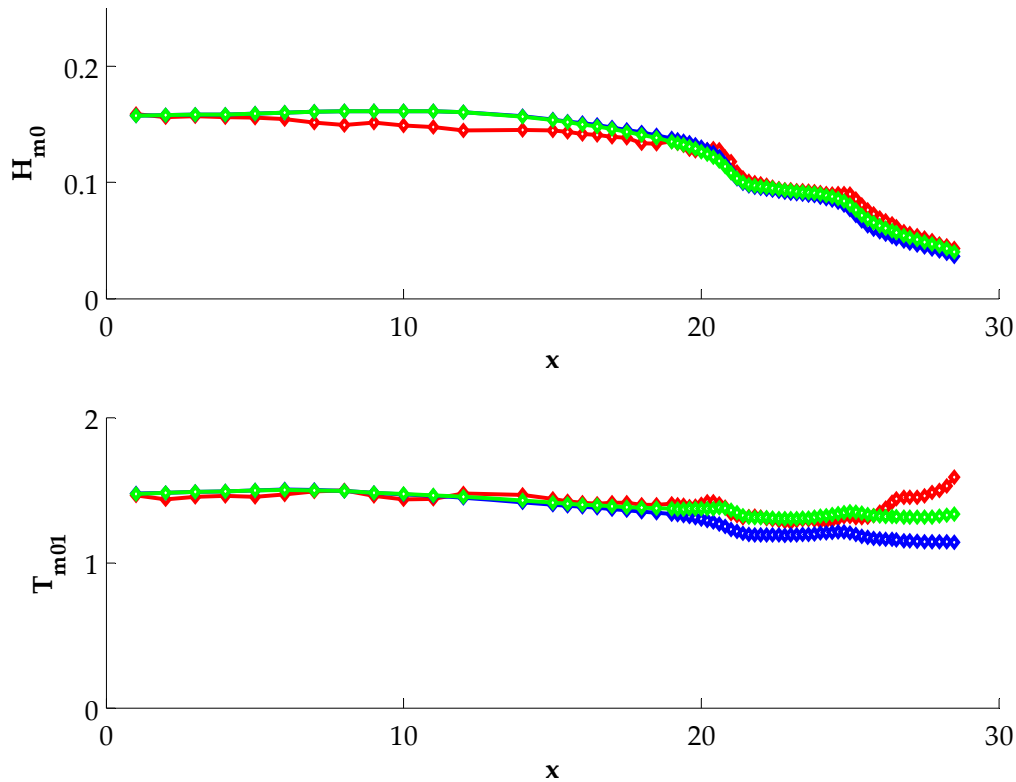


Figure 8-10: Spectral parameters Boers case 1

The measured spectra (see for example some spectra from case 1 in figure 8-11 through figure 8-14) showed that the spectra evolved from a rather steep towards the expected universal, smooth and broad shapes. In the shallowest measurement locations (figure 8-14), the spectral tails had transformed into horizontal spectra (remember the transformation), in which the peaks could hardly be distinguished from other irregularities. Not only the highest frequencies gained energy compared to lower frequencies, also the energy density at low frequencies increased as the spectrum transformed towards the universal shape. In the boundary condition of this case, a harmonic frequency peak at twice the primary peak frequency was already present. All peaks shifted towards lower frequencies for decreasing water depths.

The spectra that were simulated with the DCTA followed the general shape of the measurements very well. The spectra became progressively more horizontal and the average heights of the energy densities were well reproduced. The level of the high frequency tail though, increased too quickly, as very smooth and was throughout the entire flume overestimated. The harmonic frequency peaks were too small and less distinct than in the measurements. The first peak was too high and narrow. Again, this could be

explained by obstruction of the interactions due to the saturation of the spectral tail. The strength of the interactions was too small to reproduce the measured effects of triad interactions.

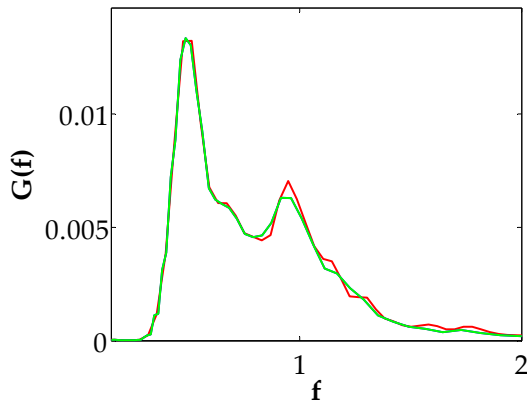


Figure 8-11: Scaled spectra Boers case 1, gauge 1

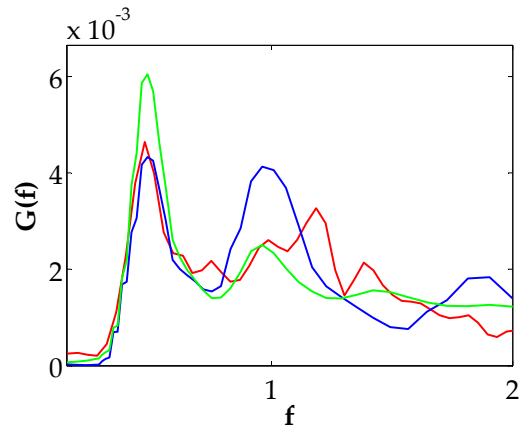


Figure 8-12: Scaled spectra Boers case 1, gauge 45

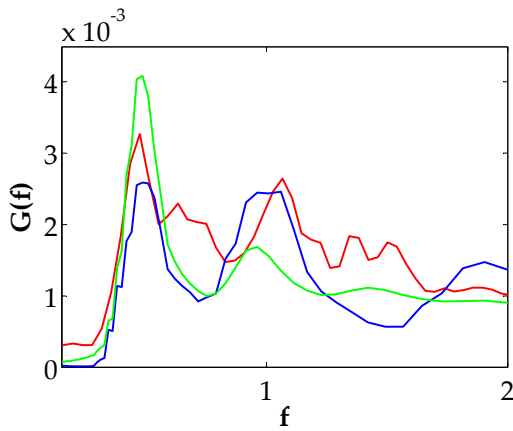


Figure 8-13: Scaled spectra Boers case 1, gauge 55

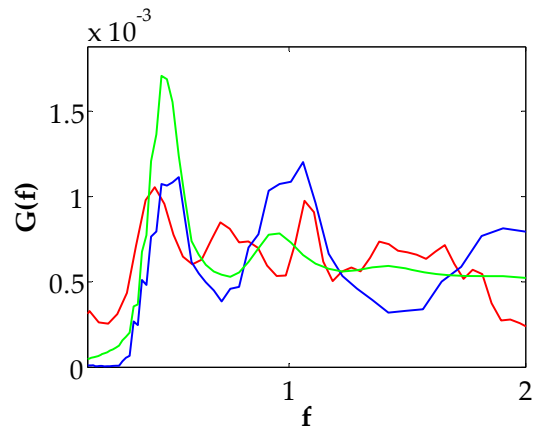


Figure 8-14: Scaled spectra Boers case 1, gauge 65

Field measurements

Delilah

The gauges of the Delilah (Duck Experiment on Low-frequency and Incident-band Longshore and Acrossshore Hydrodynamics) were located north of the FRF pier, open to storm waves from the northeast, and in an area with typically shore parallel contours (figure 8-15) near the town of Duck, North Carolina, USA. The southern end of the gauges area was in the shadow zone of the FRF pier for waves approaching from southeast (Ris et al., 2001). The measurement instruments are numbered from 10 around the shoreline (the leftmost black square of the Delilah array in figure 8-15, please note that the devices between 10 and 70 are not numbered to keep the numbers decipherable) to 90 at the seaward end. The boundary conditions were provided by a series of 13 measurements from the Samson array, about 1750 m from the waterline (located in the top-right corner of figure 8-15). These were supplemented with parametric wave conditions at the lateral two boundaries that were the same for all cases (a JONSWAP spectrum with H_{m0} 0.54 m; T_p 10.5 s; σ_θ 21°). From the measurement data, 13 different cases had been selected. The wind field and water levels were assumed homogeneous in the area. Ambient currents were absent.

SWAN was, identical to the ONR testbed (Ris et al., 2001), run in two-dimensional mode on a grid with 119x123 cells of 13.45 by 13.45 m. The spectral grid consisted of 36 directional bins in a full circle and a 53 logarithmically distributed frequencies between 0.044 and 0.6 Hz. Uniform, stationary wind fields and water levels were applied for each of the 13 available cases. The source terms for wind growth, white-capping (Hasselmann, 1974; WAMDI-group, 1988) and quadruplet interactions (Hasselmann, 1963) were used in default mode and the source terms for wave-induced setup, breaking, bottom friction too. The results of the default LTA and the DCTA with $\lambda = 0.13$ were compared.

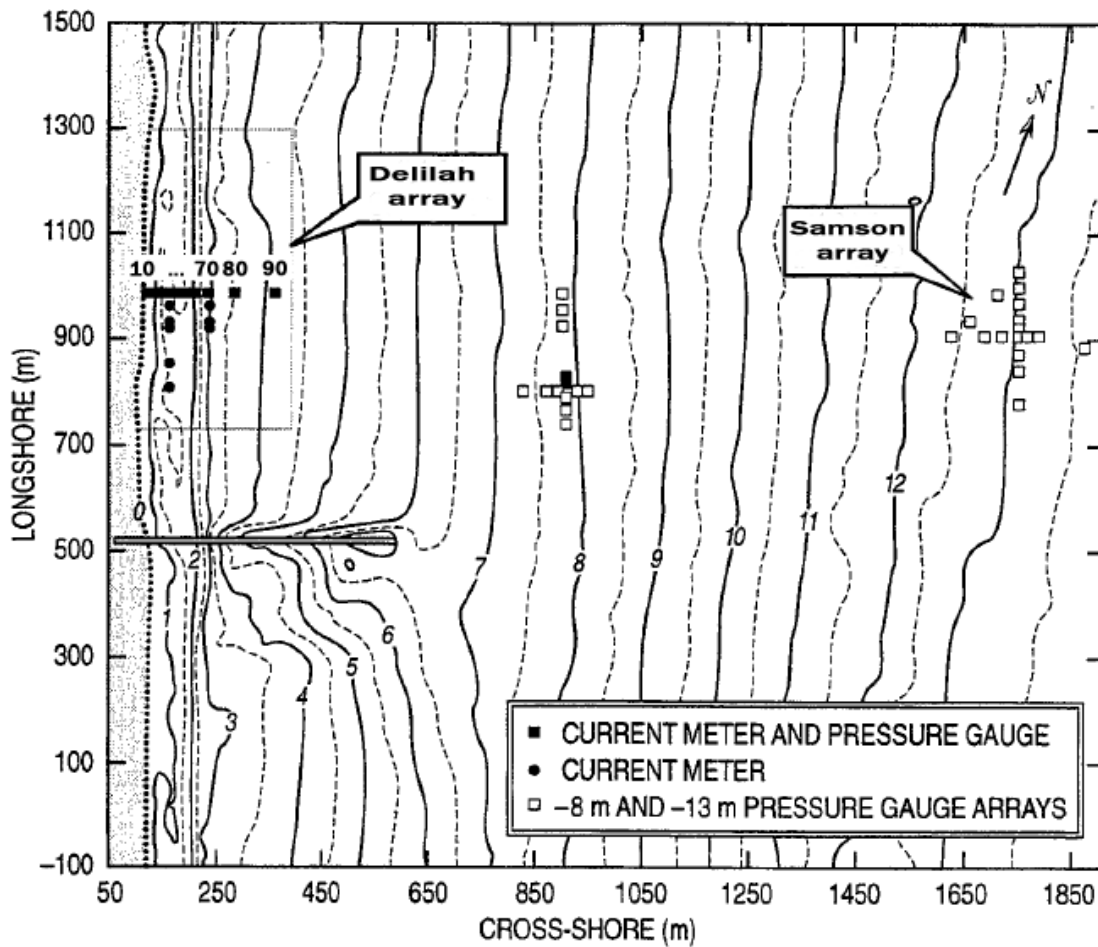


Figure 8-15: Bathymetry Delilah measurements
 Picture taken from (Rogers et al., 1998) and modified by author

When the simulations were run, several problems became apparent that had to be addressed in order to obtain useful results. The spectral parameters provided by the Samson array and those obtained from measurements of the Delilah array were very different in many of the 13 cases. The modelled significant wave heights were highly overestimated and the average wave periods underestimated. The results of case 1 are presented as an example in figure 8-16.

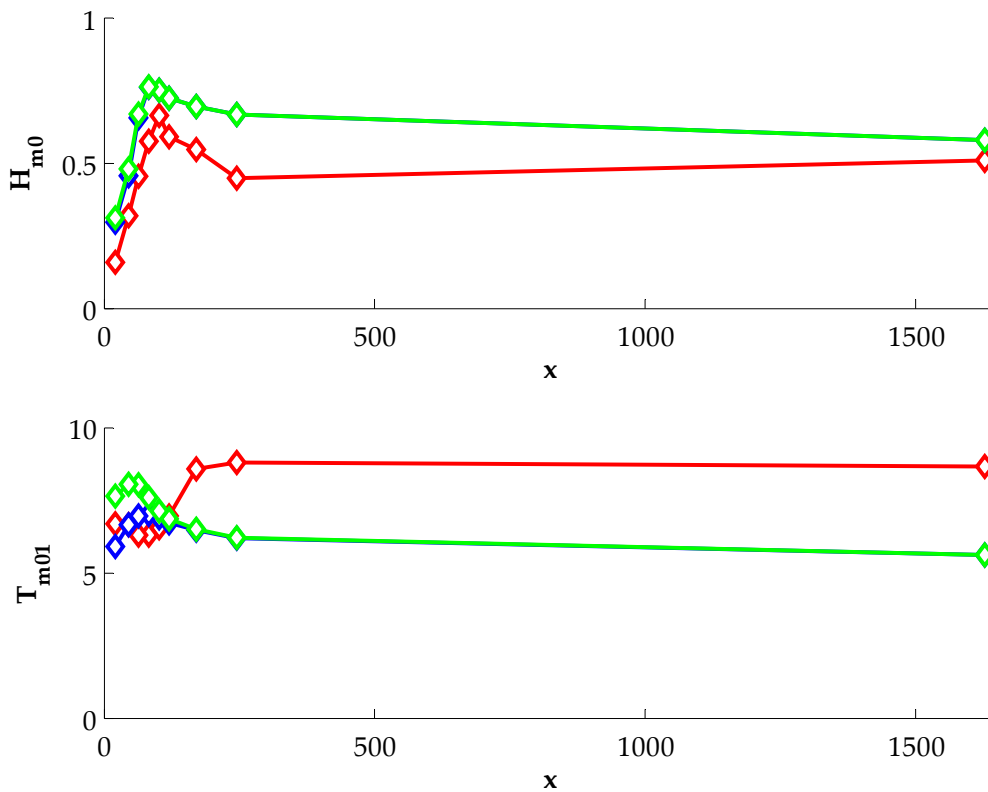


Figure 8-16: Spectral parameters Delilah measurements case 1

The large deviation between the measured and modelled parameters at the boundary (the rightmost value in figure 8-16) was a result of the fact that the spectra provided by Samson had a frequency range between 0 and 0.24 Hz while the spectra from Delilah and the computational grid of SWAN ranged from 0.044 to 0.6 Hz (notice the end of the red line in figure 8-17). As a result, SWAN imposed a fictitious energy spectrum distribution between 0.24 and 0.6 Hz based on a prognostic tail that decreased monotonically with f^{-4} and waves, propagating from the boundaries into the domain. In most cases, the diagnostic tail indeed decreased monotonically. Only the spectra of case 1 showed a peak around 0.5 Hz that visualized wind generated waves that propagated along the offshore model boundary parallel to the shoreline. In general, the energy densities in the tail of the spectra were considered reasonable estimates for the boundary conditions at the location of the Samson array although this was not definite.

The spectral parameters at the locations of the Delilah pressure meters gave very poor results. SWAN was not able to reproduce the Delilah spectra from the Samson and parametric boundary condition with default settings (compare figure 8-17 and figure 8-18). Trial calculations with non-default settings (such as

increased dissipation, or no wind), which are not presented here, could not improve the results satisfactorily.

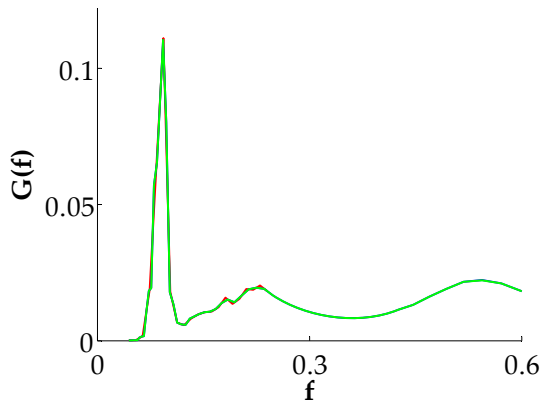


Figure 8-17: Scaled spectra Delilah case 1, Samson

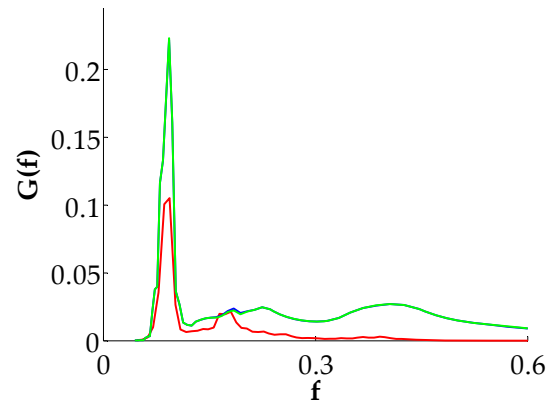


Figure 8-18: Scaled spectra Delilah case 1, gauge 90

The ONR testbed manual (Ris et al., 2001) remarks in a small note that the large differences between the measured spectra at the Samson station and the Delilah array may be due to differences in the duration and the interval of the used data records. The Samson measurement records were 2 hrs and 16 minutes long and created at intervals of three hours. The Delilah measurement records were 30 minutes long and produced every 30 minutes. The maximum difference between the moment of measuring the wave conditions at Samson and Delilah was therefore 30 minutes. Considering that the distance from the wave gauges to a computational boundary was less than 2 km and the wave group celerity of the peak frequency about 8 m/s at the boundary, this mismatch in measurement time was much larger than the average residence time of a typical wave in the computational domain. The manual suggests that the data of Delilah “should therefore be considered with care” and only 4 out of 13 cases were included in the statistical analysis of the testbed (table 8-5).

Case	Date / time	Wind U_{10}	Direction (Nautical)	Water level (+N.A.P.)
1	06-10-1990 / 16:00 hrs	7.06	160	-0.46
2	07-10-1990 / 13:00 hrs	1.38	34	-0.29
3	09-10-1990 / 10:00 hrs	7.37	129	0.63
4	09-10-1990 / 13:00 hrs	6.92	134	0.35

Table 8-5: Delilah measurements

As we looked deeper and deeper into the set-up of the simulation, more and more problems and flaws became apparent. The description of the data was unclear and incomplete (it is for instance not known at

what times exactly the Samson spectra were provided), the boundary conditions were not implemented properly and created waves that propagated parallel to the coast near the offshore boundary; the bathymetric data did not cover the entire computational grid; etc. In order to be able to use these measurements for the validation of the DCTA a fundamental restructuring of the model set-up as required which did not fit in the period of the present study. In the end, we have abandoned hope that these measurements would provide us with useful information regarding the performance of the DCTA and stopped working on them.

Amelanders Zeegat

The Amelanders Zeegat is a tidal inlet in the Wadden Sea, between the islands of Terschelling and Ameland (figure 8-19). Rijkswaterstaat (the implementing body of the Ministry of Transport, Public Works and Water Management) deployed a set of 12 wave buoys (figure 8-21) to study the complex wave processes in the inlet and the Wadden Sea behind it. Many hindcasts of spectra in the inlet during storm conditions have been performed to gain insight of the physical processes and improve the performance of SWAN. One of the recurring problems in these simulations was the underestimation of the wave periods behind the inlet. This is unlikely to be mainly due to the transfer of energy from the peak to higher frequencies by the LTA since the wave conditions behind the inlet are mainly determined by local wind growth. Waves from the North Sea are either dissipated at the ebb tidal delta or at the inner shoals after refraction out of the tidal channels (van der Westhuysen and van Vledder, 2007; van Vledder, 2008). Furthermore it is suggested that the influence of triad interactions on depth limited locally generated waves is negligible (van Vledder, 2008). Altogether, the influence of triad interactions on the spectra is expected to be negligible and simulating these measurements served to verify that the DCTA is not activated at the inner parts of the tidal inlet.



Figure 8-19: The Wadden Sea and the Amelanders Zeegat

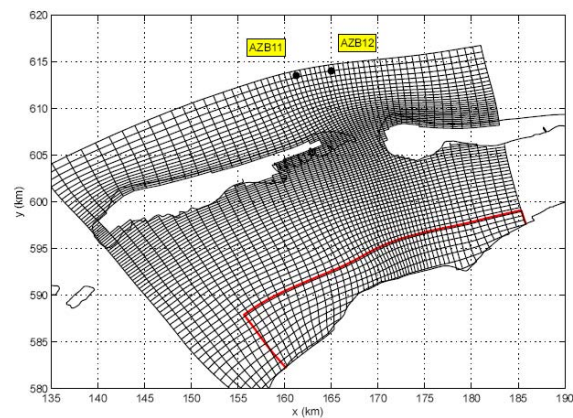


Figure 8-20: Grid AZG3A

The simulations were run on the curvilinear AZG3A grid (the default grid for simulations of the Amelanders Zeegat, figure 8-20) in stationary mode. The storm of February 1st 2005, 10:00 hr was modelled with water levels and current fields from simulations with a two-dimensional flow model and a uniform

wind field based on measurements near the inlet. A two-dimensional spectrum from a larger wave model that covered a larger area around the Wadden Sea was applied as a boundary condition. Swan was run in two-dimensional, stationary mode with 36 directional bins in a full circle and 37 frequency bins between 0.03 and 1 Hz. The deepwater source terms were either those of Komen (1994) or Rogers (2003), breaking and bottom friction were applied with default values and triads were switched off or evaluated with the LTA, or the DCTA.



Figure 8-21: Buoy network Ameland Zeegat

In figure 8-22 and figure 8-23, the spectra of eight buoys with the deepwater source terms of Komen resp. Rogers are presented. As expected, the triads were only of limited influence on the shape of most spectra. Before the ebb tidal delta (buoys AZB11 and AZB12), the influence of triad interactions was negligible due to the large relative depths (more than five times the significant wave heights). The spectra behind the tidal inlet (buoys AZB41, AZB42, AZB51 and AZB52) were dominated by local wind growth (characterised by low energies at relatively high frequencies), there were no distinct peaks at higher

harmonic frequencies and all results are almost identical. As expected, the influence of triad interactions is not visible in the observations.

At buoys AZB31 and AZB32, behind the ebb-tidal delta, some differences between simulations with and without triads, could be seen between 0.1 and 0.3 Hz. This showed that the influence was limited to small transfers from the peak frequency to frequencies around twice the peak frequency. In the simulations with either Komen (figure 8-22) or Rogers (figure 8-23), the results for the cases without triads gave the best results for the peak energy and the LTA gave the best results for the high frequency side of the peak (around 0.2 Hz.). The DCTA gave results that were in between those of the LTA and those without triads. It was hard to say which formulation gave the best results based on so little information, but the scaling of the DCTA worked well for this type of environment since the triad were active and inactive at the buoy locations where they should be.

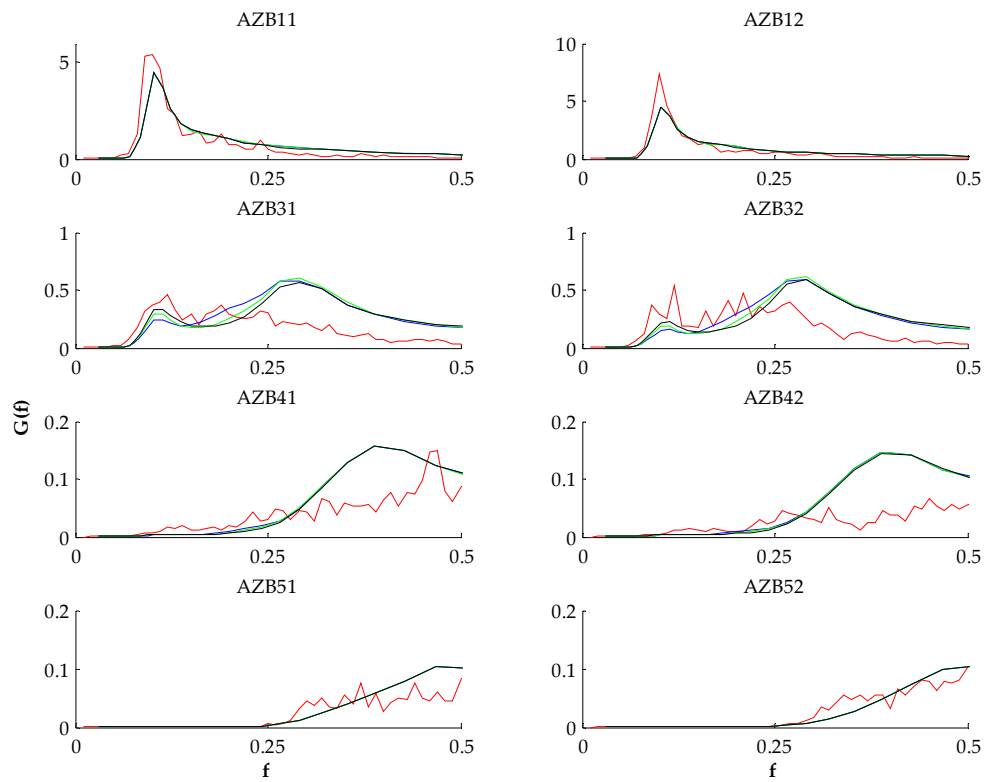


Figure 8-22: Scaled spectra Amelander Zeegat, Komen source terms

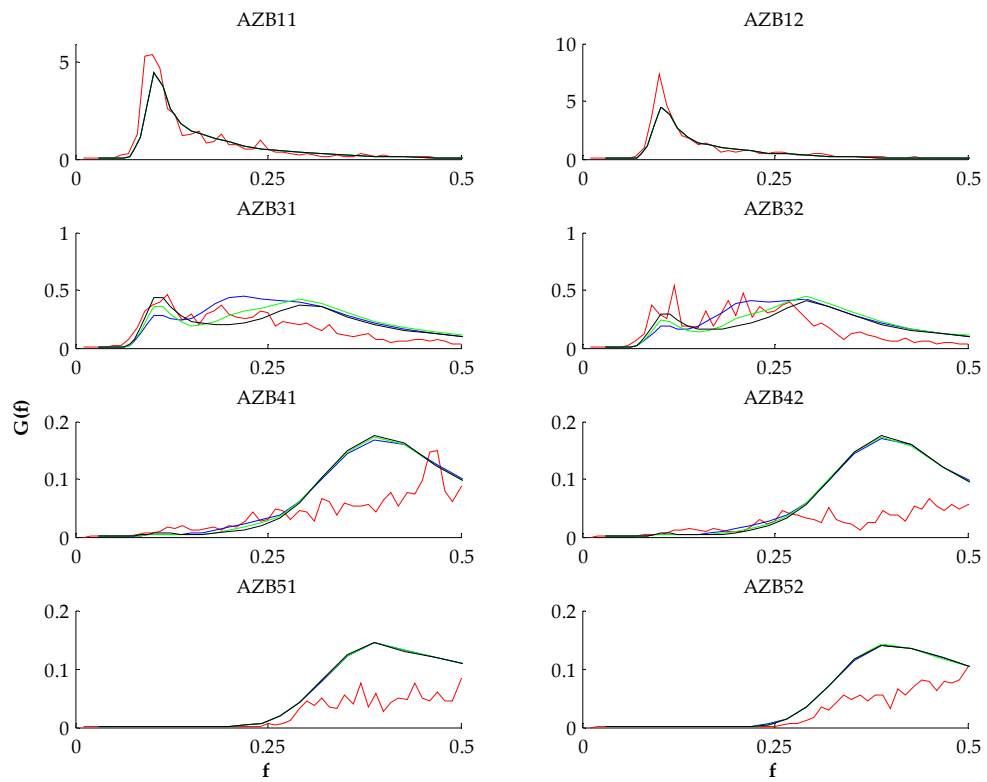


Figure 8-23: Scaled spectra Amelander Zeegat, Rogers source terms

Haringvliet

The DCTA was subsequently used to simulate a series of field observations in the Haringvliet Estuary (figure 8-24) where the presence of triad interactions was clear from the observed spectra. At the entrance of the Haringvliet, eight wave buoys (figure 8-25) were employed around a large shoal called the “Hinderplaat”, visible between buoys 4, 5 and 7. Note that the shape of the waterline in figure 8-25 does not correspond with the situation at the time of the measurements as the Maasvlakte was considerable smaller and the Slufter basin was not installed either. The northern part of the Haringvliet basin was wider. As waves approach the estuary from deep water, they break over the shoal and undergo triad interactions.

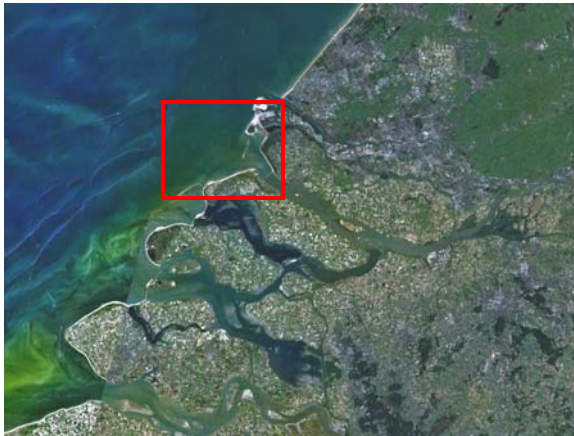


Figure 8-24: The Rhine estuary and the Haringvliet



Figure 8-25: Buoy network Haringvliet

A series of four measurements with wave buoys of October 14th 1982 between 21:00 and 0:00 hrs (table 8-6) from the ONR testbed (Ris et al., 2001) were reproduced to observe whether the DCTA was able to reproduce the harmonic peaks in the spectra. Water levels and wind fields were taken uniform and stationary for each case, currents were assumed negligible. Measurements from buoy 1 served as boundary conditions along the westward model boundary. A rectangular grid of 8 by 22 kilometres with a spatial resolution of 150 x 250 m was used. Swan was run in two-dimensional, stationary mode with 36 directional bins in a full circle and 31 frequency bins between 0.05 and 1 Hz. The deepwater source terms were default, as were depth-induced breaking and bottom friction. Triad interactions were switched off, computed with the LTA, or with the DCTA. In figure 8-26, the spectra of cases 4 are given as an example. Not all measurements were obtained at the exact same moment as the boundary conditions (buoy 1).

Therefore, the results from right before or right after the modelled moment are plotted (which moments are plotted can be read in the legends).

Case	Date / time	Wind U_{10}	Direction (Nautical)	Water level (+N.A.P.)
1	14-10-1982 / 21:00 hrs	17	330	0.30
2	14-10-1982 / 22:00 hrs	12	300	0.90
3	14-10-1982 / 23:00 hrs	14	300	1.70
4	15-10-1982 / 00:00 hrs	15	300	2.10

Table 8-6: Haringvliet measurements

The spectra transformed in all four cases from a rather narrow, unimodal shape at buoy 1 towards a much broader shape with lower energy densities and the maximum level at a higher frequency. This was predominantly due to a combination of wind generation, depth-induced breaking dissipation and triad interactions as was verified with additional computations (which are not presented here). The general decay of the total amount of spectral energy was very well simulated with SWAN (please keep the large variation in the scale of the spectra in mind). The decay of the primary peak and the regeneration of high-frequency energy however, were not well predicted in the shallow regions of the domain. Especially behind the “Hinderplaat” (buoys 5 ,6 and 7), the level of the peak frequency was over predicted. However, it must be stressed that only small residuals of low-frequency energy are compared here.

The regeneration at high frequencies may have been due to too much energy transfer from the lower frequencies by the triad interactions or by too much generation by wind. Repeated computations without triad wave-wave interactions but with wind and vice versa showed that both processes are equally responsible for this high-frequency regeneration. The effect of simulated triad interactions could be seen from the simulations without triad interactions, which indicated that only at buoy 8, the energy around the high frequency edge of the peak (around 0.3 Hz) was not a result of nonlinear interactions, but due to wind sea, since all three triad formulations gave similar results. The DCTA improved the computational results for the higher frequencies in the sense that at the stations just behind the shoal, where the effect of triad wave-wave interactions were expected to be largest, the agreement with the observations at high frequencies was greatly improved. It predicted the best balance between the simulation of both the spectral peak and the high frequency flank of the spectrum. The peak energy was still over-predicted, but this may be due to the blocking of triad interactions due to approaching the universal spectrum. As the

deviations from the universal spectrum become smaller, the magnitudes of the exchanges of energy decrease accordingly. Since the tail is generally closer to the equilibrium, the “pumping” of energy towards higher frequencies (where that extra energy would presumably be dissipated) is restricted. The LTA improved the spectral peak levels by transferring energy to higher frequencies and gave the best estimate for the peak energy, but then the energy at higher frequencies was overestimated.

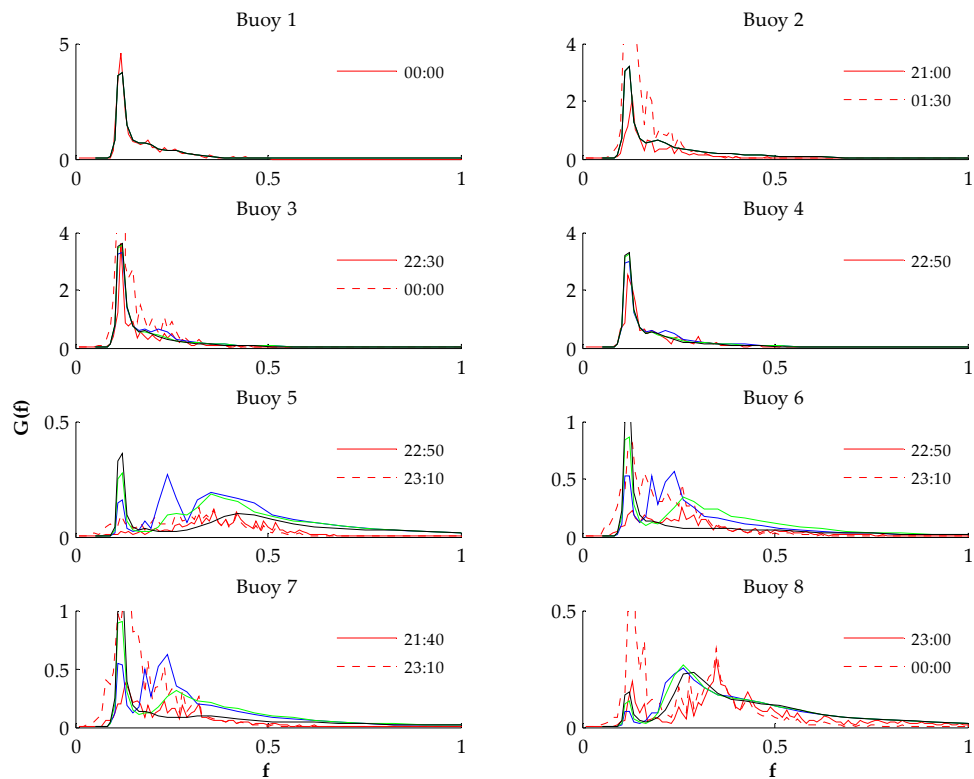


Figure 8-26: Scaled spectra Haringvliet case 4

9 Conclusions and recommendations

The basic formulation of the Distributed Collinear Triad Approximation (DCTA), as presented in a paper to the International Conference on Coastal Engineering (Holthuijsen and Booij, 2006), was taken as a starting point for this work. It derived an expression for triad interactions as an analogy with the quadruplet interactions that converges towards a prescribed universal shape but leaves the magnitudes free to develop. This expression was improved in a subsequent manuscript (of which the present author is co-author) to transform spectra towards a more correct universal shape and extended with a scaling that was based on an analogy with the scaling of the Lumped Triad Approximation (LTA; Eldeberky, 1996) and a heuristic scaling for the mismatch from resonance. The consequent implementation in SWAN (Booij et al., 1999) and validation on horizontal and sloping bottoms indicated that the DCTA is capable of transferring energy throughout the entire spectrum via resonant triads of wave components. Initially harmonic peaks appear, but as the waves progress towards shallow water, these peaks disappear and the spectrum converges towards a smooth shape of the spectral tail in a relaxation-type manner, in qualitative agreement with laboratory measurements (Smith and Vincent, 2003). This was a huge improvement over the LTA, which only transferred energy upwards to second harmonic frequencies and did not converge towards a universal shape.

The scaling of the DCTA was calibrated with measurements of Smith (2004) to tune the calibration coefficient λ to these observations. This was done through finding for each incident spectrum separately, the minimum of the error-values of the difference between measured and modelled parameter values in the whole domain. The calibration of the DCTA had to be combined with a calibration for the dissipation since these processes influence each other and the default depth-induced breaking dissipation in SWAN did not agree with the measured dissipation. The optimum values thus obtained where $\lambda = 0.13$ for the tuneable coefficient of the DCTA and $\gamma = 0.79$ for the Battjes-Janssen breaker coefficient. Whilst the general shape of the spectral tail was reproduced satisfactorily, the magnitudes of the harmonic peaks were under predicted, as was the decay of the peak. It seemed that once the energy at higher frequencies approached the prescribed levels, the triad energy transfers were inhibited in the model. As a result, the peak energy remained too high and the features in the spectrum were not smoothed sufficiently.

Subsequent verification of the calibrated DCTA with a large set of laboratory and field measurements confirmed the same type of behaviour for various scales and conditions. From the same measurements as the calibration, but now with the average calibrated value for λ and default values for all other processes, was concluded that the T_{m01} was better predicted but that the scatter was very large (as large as the average error-value for all 31 Smith cases). For the Beji-Battjes experiment, which was used to calibrate the LTA, the DCTA even gave worse estimates for T_{m01} . Most field measurements gave little detailed information about the performance of the DCTA since they showed either no distinct effects of triad interactions (Amelander Zeegat) or a large dissipation that were not accurately reproduced by SWAN (Delilah). The Haringvliet measurements indicated that the general shape of the spectra improved when the DCTA was used, compared to the LTA or the triad source term switched off. The broadening of the spectra was predicted better but the level of the spectral peak was overestimated.

In general, it was concluded that the calibrated DCTA produces a high frequency tail of the correct shape but it does not represent the level of higher harmonic peaks satisfactorily. These peaks are too slowly generated and not high enough while the primary peak is overestimated and not decay quickly enough. Irregular features in the spectrum are not removed sufficiently and they are longer visible in the simulated spectra than in the measured. Increasing the value of the tuneable parameter λ does not solve this since the energy densities at high frequencies are then overestimated and the saturation prohibits a continual transfer of energy. A solution for this behaviour of the DCTA may lie in an increased dissipation of energy at higher frequencies. At present, the dissipation is assumed to be distributed linearly proportional to the energy densities. In literature, it is suggested that the depth-induced breaking dissipation is proportional to σ^2 (Mase and Kirby, 1992; Kirby and Kaihatu, 1996; Chen et al., 1997; Herbers et al., 2000; Kaihatu et al., 2007) and the white-capping dissipation is proportional to either $k^{1.5}$ or k^2 (Rogers et al., 2003). With such adaptation, the triad interactions will continue to transfer energy from the spectral peak towards higher frequencies with a later saturation of the spectral levels and consequently decrease the energy at the spectral peak. The model of Herbers (2000) supports this idea of a constant energy flux through the spectrum.

Although the data pool with which the DCTA was calibrated (31 laboratory measurements) and validated (35 laboratory measurements and 5 field observations) already is quite extensive, extending the set with additional measurements will very likely improve the results. The calibration was only done with laboratory measurements on a constant 1:30 slope. Quantification with measurements of a different

scale, at slopes of a different inclination or other with bathymetries will indicate whether the DCTA remains accurate in a wider type of bathymetries, or tune its settings to more generic values. The current analysis especially lacks good quality field observations in which triad interactions are clearly visible in the spectra. As this study has pointed out the quantification of the DCTA depends highly on the quality of the modelled dissipation, any further development of the DCTA should be accompanied by an improvement of the dissipation formulation. The Battjes-Janssen formulation was in this study not able to simulate the dissipation satisfactorily. To avoid that the dissipation has to be tuned in any successive quantification or analysis of the DCTA, a better formulation is recommended. It should at least distribute the dissipation with σ^2 and preferably estimate the bulk rate of dissipation throughout the domain better. Finally, it is recommended that the analysis of the spectral parameters, is extended with additional expressions. Currently only H_{m0} and T_{m01} were analysed and used for the calibration. Investigating other wave periods (such as T_{m-10}) may provide additional insight in the distribution of energy among the spectrum and hence give a more solid interpretation of the quality of the DCTA.

References

- Armstrong et al. (1962). Interactions between Light Waves in a Nonlinear Dielectric. *Physical Review*, 127(6), 1918.
- Battjes and Janssen (1978). *Energy loss and set-up due to breaking of random waves*. Paper presented at the 16th International Conference on Coastal Engineering, Hamburg.
- Beji and Battjes (1993). Experimental investigation of wave propagation over a bar. *Coastal Engineering*, 19(1-2), 151-162.
- Boers (2005). *Surf zone turbulence*. Delft University of Technology.
- Booij et al. (2009). *A distributed collinear triad approximation in SWAN*. Paper presented at the 6th International Conference on Coastal Dynamics, Tokyo, Japan.
- Booij et al. (1999). A third-generation wave model for coastal regions; Part 1. Model description and validation. *J. Geophys. Res.*, 104.
- Bouws et al. (1985). Similarity of the wind wave spectrum in finite depth water; Part 1. Spectral form. *J. Geophys. Res.*, 90.
- Chen et al. (1997). Modeling spectra of breaking surface waves in shallow water. *J. Geophys. Res.*, 102.
- Doering and Bowen (1995). Parametrization of orbital velocity asymmetries of shoaling and breaking waves using bispectral analysis. *Coastal Engineering*, 26(1-2), 15-33.
- Eldeberky (1996). *Nonlinear transformation of wave spectra in the nearshore zone*. Delft University of Technology.
- Eldeberky and Battjes (1996). Spectral modeling of wave breaking: Application to Boussinesq equations. *J. Geophys. Res.*, 101.
- Hasselmann (1963). On the non-linear energy transfer in a gravity-wave spectrum. Part 3. Evaluation of the energy flux and swell-sea interaction for a Neumann spectrum. *Journal of Fluid Mechanics Digital Archive*, 15(03), 385-398.
- Hasselmann (1974). On the spectral dissipation of ocean waves due to white capping. *Boundary-Layer Meteorology*, 6(1), 107-127.
- Hasselmann et al. (1973). Measurements of wind-wave growth and swell decay during the Joint North Sea Wave Project (JONSWAP). *Deutsche Hydrographische Zeitschrift*, 8(12).

- Herbers and Burton (1997). Nonlinear shoaling of directionally spread waves on a beach. *J. Geophys. Res.*, 102.
- Herbers et al. (2000). Spectral energy balance of breaking waves within the surf zone. *Journal of Physical Oceanography*, 30(11), 2723-2737.
- Herterich and Hasselmann (1980). A similarity relation for the nonlinear energy transfer in a finite-depth gravity-wave spectrum. *Journal of Fluid Mechanics Digital Archive*, 97(01), 215-224.
- Holthuijsen (2007). *Waves in oceanic and coastal waters*. Cambridge, UK: Cambridge University Press.
- Holthuijsen and Booij (2006). *Experimental wave breaking in SWAN*.
- Janssen et al. (2006). Generalized evolution equations for nonlinear surface gravity waves over two-dimensional topography. *Journal of Fluid Mechanics*, 552(1), 393-418.
- Kaihatu et al. (2007). Asymptotic behavior of frequency and wave number spectra of nearshore shoaling and breaking waves. *J. Geophys. Res.*, 112.
- Kirby and Kaihatu (1996). *Structure of frequency domain models for random wave breaking*. Paper presented at the 25th International Conference on Coastal Engineering.
- Komen et al. (1994). *Dynamics and modelling of ocean waves*. Cambridge, UK: Cambridge University Press.
- Kuik et al. (1988). A Method for the Routine Analysis of Pitch-and-Roll Buoy Wave Data. *Journal of Physical Oceanography*, 18(7), 1020-1034.
- Kuznetsov and Saprykina (2004). Frequency-dependent energy dissipation of irregular breaking waves. *Water Resources*, 31, 384-392.
- Madsen and Sørensen (1993). Bound waves and triad interactions in shallow water. *Ocean Engineering*, 20(4), 359-388.
- Mase and Kirby (1992). *Hybrid frequency-domain KdV equation for random wave transformation*. Paper presented at the 23th International Conference on Coastal Engineering, Venice.
- Phillips (1960). On the dynamics of unsteady gravity waves of finite amplitude Part 1. The elementary interactions. *Journal of Fluid Mechanics Digital Archive*, 9(02), 193-217.
- Resio et al. (2001). Nonlinear energy fluxes and the finite depth equilibrium range in wave spectra. *J. Geophys. Res.*, 106.
- Ris et al. (2002). *The ONR test bed for coastal and oceanic wave models*. Paper presented at the 28th International Conference on Coastal Engineering.
- Ris et al. (2001). Manual for the ONR test bed for Coastal and Oceanic wave models.
- Rogers et al. (2003). Investigation of wave growth and decay in the SWAN model: Three regional-scale applications. *Journal of Physical Oceanography*, 33(2), 366-389.

- Rogers et al. (1998). Review and Verification of Numerical Wave Models for Near Coastal Areas - Part 2: Verification of Near Coastal Numerical Wave Models.
- Smith (2004). *Shallow water spectral shapes*. Paper presented at the 29th International Conference on Coastal Engineering.
- Smith and Vincent (1992). Shoaling and decay of two wave trains on beach. *Journal of Waterway, Port, Coastal and Ocean Engineering*, 118(5), 517-533.
- Smith and Vincent (2002). *Application of spectral equilibrium ranges in the surf zone*. Paper presented at the 28th International Conference on Coastal Engineering.
- Smith and Vincent (2003). Equilibrium ranges in surf zone wave spectra. *J. Geophys. Res.*, 108.
- SWAN-team (2008). *SWAN technical documentation*: Delft University of Technology.
- Toba (1973). Local balance in the air-sea boundary processes. *Journal of Oceanography*, 29(5), 209-220.
- van der Westhuysen and van Vledder (2007). *Sensitivity analysis of SWAN for the Amelande Zeegat*: WL | Delft Hydraulics.
- van Vledder (2008). *Analysis of SWAN hindcasts Wadden Sea, Oosterschelde and Sloterneer*: Alkyon.
- WAMDI-group (1988). The WAM model; a third generation ocean wave prediction model. *Journal of Physical Oceanography*, 18(12), 1775-1810.
- Zakharov (1999). Statistical theory of gravity and capillary waves on the surface of a finite-depth fluid. *Eur. J. Mech. B/Fluids*.

List of figures

Figure 6-1: Schematic energy density spectrum $E(\sigma)$, in equilibrium.....	42
Figure 6-2: Scaled schematic energy density spectrum $G(\sigma)$, in equilibrium	42
Figure 6-3: Schematic energy density spectrum $E(\sigma)$, out of equilibrium.....	42
Figure 6-4: Scaled schematic energy density spectrum $G(\sigma)$, out of equilibrium.....	42
Figure 6-5: Spectral parameters flat bottom case, 60 m water depth	43
Figure 6-6: Spectral parameters flat bottom case, 6 m water depth	43
Figure 6-7: Spectral parameters flat bottom case, 0.6 m water depth	44
Figure 6-8: Scaled spectrum flat bottom case, 60 m water depth, 1.000 m from up-wave boundary	44
Figure 6-9: Scaled spectrum flat bottom case, 60 m water depth, 10.000 m from up-wave boundary	44
Figure 6-10: Scaled spectrum flat bottom case, 6 m water depth, 1.000 m from up-wave boundary	45
Figure 6-11: Scaled spectrum flat bottom case, 6 m water depth, 10.000 m from up-wave boundary	45
Figure 6-12: Scaled spectrum flat bottom case, 0.6 m water depth, 1,000 m from up-wave boundary	46
Figure 6-13: Scaled spectrum flat bottom case, 0.6 m water depth, 10,000 m from up-wave boundary	46
Figure 6-14: Bathymetry constant slope cases.....	47
Figure 6-15: Spectral parameters constant bottom case, unimodal spectrum.....	47
Figure 6-16: Spectral parameters constant bottom case, bimodal spectrum	47
Figure 6-17: Scaled spectrum constant slope case, unimodal spectrum, 1.000 m from up-wave boundary.....	48
Figure 6-18: Scaled spectrum constant slope case, unimodal spectrum, 10.000 m from up-wave boundary.....	48
Figure 6-19: Scaled spectrum constant slope case, bimodal spectrum, 1.000 m from up-wave boundary	48
Figure 6-20: Scaled spectrum constant slope case, bimodal spectrum, 10.000 m from up-wave boundary	48
Figure 6-21: Bathymetry tidal inlet case.....	49
Figure 6-22: Scaled spectrum tidal inlet case, 1.000 m from up-wave boundary	50
Figure 6-23: Scaled spectrum tidal inlet case, 5.000 m from up-wave boundary	50
Figure 6-24: Scaled spectrum tidal inlet case, 10.000 m from up-wave boundary	50
Figure 6-25: Scaled spectrum tidal inlet case, 25.000 m from up-wave boundary	50
Figure 7-1: Bathymetry Smith measurements.....	51
Figure 7-2: H_{m0} Smith case 3, higher value at gauge 8.....	53
Figure 7-3: Spectral parameters Smith case 31.....	55
Figure 7-4: Scaled spectra Smith case 31, gauge 1.....	56
Figure 7-5: Scaled spectra Smith case 31, gauge 2.....	56

Figure 7-6: Scaled spectra Smith case 31, gauge 5.....	56
Figure 7-7: Scaled spectra Smith case 31, gauge 7.....	56
Figure 7-8: Scaled spectra Smith case 20, gauge 1.....	57
Figure 7-9: Scaled spectra Smith case 20, gauge 2.....	57
Figure 7-10: Scaled spectra Smith case 20, gauge 5.....	57
Figure 7-11: Scaled spectra Smith case 20, gauge 7.....	57
Figure 7-12: Scaled spectra Smith case 5, gauge 1.....	58
Figure 7-13: Scaled spectra Smith case 5, gauge 2.....	58
Figure 7-14: Scaled spectra Smith case 5, gauge 5.....	58
Figure 7-15: Scaled spectra Smith case 5, gauge 7.....	58
Figure 7-16: Scaled spectra Smith case 1, gauge 1.....	59
Figure 7-17: Scaled spectra Smith case 1, gauge 2.....	59
Figure 7-18: Scaled spectra Smith case 1, gauge 5.....	59
Figure 7-19: Scaled spectra Smith case 1, gauge 7.....	59
Figure 7-20: Scatterplot $\gamma - \lambda$	62
Figure 8-1: Scatterplot $\varepsilon(T_{m01}) - \lambda$	64
Figure 8-2: Bathymetry Beji-Battjes measurements.....	65
Figure 8-3: Spectral parameters Beji-Battjes.....	66
Figure 8-4: Scaled spectra Beji-Battjes, gauge 5.....	67
Figure 8-5: Scaled spectra Beji-Battjes, gauge 8.....	67
Figure 8-6: Bathymetry Boers measurements.....	68
Figure 8-7: Scaled initial spectrum Boers case 1.....	69
Figure 8-8: Scaled initial spectrum Boers case 2.....	69
Figure 8-9: Scaled initial spectrum Boers case 3.....	69
Figure 8-10: Spectral parameters Boers case 1.....	70
Figure 8-11: Scaled spectra Boers case 1, gauge 1.....	71
Figure 8-12: Scaled spectra Boers case 1, gauge 45.....	71
Figure 8-13: Scaled spectra Boers case 1, gauge 55.....	71
Figure 8-14: Scaled spectra Boers case 1, gauge 65.....	71
Figure 8-15: Bathymetry Delilah measurements.....	73
Figure 8-16: Spectral parameters Delilah measurements case 1.....	74
Figure 8-17: Scaled spectra Delilah case 1, Samson.....	75
Figure 8-18: Scaled spectra Delilah case 1, gauge 90.....	75
Figure 8-19: The Wadden Sea and the Amelander Zeegat.....	77
Figure 8-20: Grid AZG3A.....	77

Figure 8-21: Buoy network Amelander Zeegat.....	78
Figure 8-22: Scaled spectra Amelander Zeegat, Komen source terms.....	80
Figure 8-23: Scaled spectra Amelander Zeegat, Rogers source terms.....	81
Figure 8-24: The Rhine estuary and the Haringvliet	82
Figure 8-25: Buoy network Haringvliet	82
Figure 8-26: Scaled spectra Haringvliet case 4	84

List of tables

Table 7-1: Results calibration Smith.....	54
Table 8-1: Results verification Smith.....	64
Table 8-2: Results verification Beji-Battjes	65
Table 8-3: Boers measurements.....	68
Table 8-4: Results verification Boers.....	69
Table 8-5: Delilah measurements.....	75
Table 8-6: Haringvliet measurements	83

Nomenclature

Name	Symbol	Unit
System matrix	A	–
Right hand side vector	b	[N]
Bottom friction coefficient	c_f	–
Propagation velocity in geographical space	c_g	$m s^{-1}$
Propagation velocity in direction space	c_θ	$Hz s^{-1}$
Propagation velocity in frequency space	c_σ	$^\circ s^{-1}$
Water depth	d	m
Energy density as a function of absolute angular frequency	$E(f)$	$m^2 Hz^{-1}$
Energy density as a function of wave number	$E(k)$	m
Energy density as a function of intrinsic radian frequency	$E(\sigma)$	$m^2 Hz^{-1}$
Absolute angular frequency	f	Hz
Scaled energy density as a function of intrinsic radian frequency	$G(\sigma)$	m^{3+p}
Gravitational acceleration	g	$m s^{-2}$
Maximum wave height	H_{max}	m
Significant wave height	H_{m0}	m
Wave number	k	m
Triad average wave number	\bar{k}	m
Spectrum average wave number	\hat{k}	m
Spectral moment n	m_n	–
Action density as a function of intrinsic radian frequency	$N(\sigma)$	$m^2 Hz^{-2}$
Action density as a function of wave number	$N(k)$	$m Hz^{-1}$
Action density vector	N	[N]
Iteration step	n	–
Power coefficient of universal spectral shape	p	–
Fraction of broken waves	Q_b	–
Ursell number	Q_{Ursell}	–
Source term for energy balance	S^E	$m^2 Hz^{-1} s^{-1}$
Source term for action balance	S^N	$m^2 Hz^{-2} s^{-1}$
Quadruplet interaction coefficient	T	–
Mean wave period	T_{m01}	s
Peak period	T_p	s
Time	t	s

Horizontal main direction	x	m
Total number of measurement locations	Z	–
Universal shape level constant	α	–
Battjes-Janssen breaking coefficient	α_{BJ}	–
Parameterised biphase	β	–
Breaker index parameter	γ	–
TMA spectral peakedness parameter	γ_p	–
Ursell scaling parameter	δ	–
Error-value parameter of parameter ζ	$\varepsilon(\zeta)$	$[\zeta]$
Arbitrary spectral parameter	ζ	$[\zeta]$
Nautical direction	θ	°
DCTA tuneable coefficient	λ	–
Intrinsic radian frequency	σ	Hz
JONSWAP spectral width	σ_θ	°
Spectrum average frequency	$\hat{\sigma}$	Hz
DCTA scaling coefficient	χ	–

Appendices

Appendix A Code listing

The SWAN subroutine STRICL contains the code of the that was used to implement the DCTA in SWAN

⌋ : Code command continues on next line

```

!
!*****
!
!
!   SUBROUTINE STRICL (ACLOC  ,DEPLOC  ,SPCSIG  ,KWAVE  ,
!   &                IDDLLOW ,IDDTOP  ,ANYBIN  ,IMATDA  ,IMATRA ,
!   &                CGO     ,KMESPC  ,ETOT    ,SMEBRK  ) 40.45
!
!*****
!
!   USE OCPCOMM4
!   USE SWCOMM3
!   USE SWCOMM4
!   USE M_WCAP
!
!   IMPLICIT NONE
!
!##COPYRIGHT
!##DISCLAIMER
!
! 0. Authors
!
!   40.45: Nico Booij
!   40.96: Matthijs B nit
!
! 1. Updates
!
!   40.45, July 04: NEW SUBROUTINE
!   40.96: Aug 08 - Aug 09: IMPROVEMENTS
!
! 2. Purpose
!
!   In this subroutine the triad-wave interactions are calculated
!   with the empiric distributed colinear approximation.
!
! 3. Method
!
!   Transfer of action between two components under influence of a
!   third one is formulated as follows:
!
!
!           P+1           P+1
!   M * N (Sigma  N  - Sigma  N  )
!           3           1 1           2 2
!
!   in which:
!
!   M           is a dimensional coefficient

```

```

!      N      is action density
!      Sigma  spectral (angular) frequency

!      Dimensions:
!      ACL#   : m2s2
!      KW#    : 1/m
!      SIG#   : 1/s
!      SDIA#  : 1/s

! 4. Argument variables

!      REAL, INTENT(INOUT)  :: SWTSDA(1:MDC,1:MSC,1:NPTST,1:MTSVAR)  ! Values of ↵
the triad source terms in test-points (defined in command TEST)
      REAL, INTENT(IN)     :: ACLOC(1:MDC,1:MSC)                      ! local ↵
action density spectrum
      REAL, INTENT(IN)     :: DEPLOYC                               ! Depth at ↵
gridpoint ix,iy (obtained from SWANCOM1)
      REAL, INTENT(IN)     :: SPCSIG(1:MSC)                          ! Relative ↵
frequencies in computational domain in sigma-space
      REAL                  :: KWAVE(1:MSC)                           ! Wave ↵
number in stencil points
      INTEGER, INTENT(IN)  :: IDDLLOW                                ! Minimum ↵
counter in directional space
      INTEGER, INTENT(IN)  :: IDDTOP                                  ! Maximum ↵
counter in directional space
      LOGICAL, INTENT(IN)  :: ANYBIN(1:MDC,1:MSC)                    ! If True ↵
this bin is going to be updated using the matrix
      REAL                  :: IMATDA(1:MDC,1:MSC)                   ! IMATDA: ↵
Diagonal of matrix
      REAL                  :: IMATRA(1:MDC,1:MSC)                   ! IMATRA: ↵
Right hand vector of matrix
      REAL, INTENT(IN)     :: CGO(1:MSC)                              ! Group ↵
velocities in stencil points
      REAL, INTENT(IN)     :: KMESPC                                  ! Mean wave ↵
number of the spectrum
      REAL, INTENT(IN)     :: ETOT                                    !
      REAL, INTENT(IN)     :: SMEBRK                                  !

!      Values from common

!      MDC      : Size of array in theta-direction
!      MSC      : Size of array in sigma-direction
!      ITRIAD   : indicates type of triad formulation
!      PI       : Circular constant Pi
!      MTRIAD   : Size of array containing triad-coefficients
!      PTRIAD   : Tunable coefficients for nonlinear triad sourceterms
!      PTRIAD(1) : Interaction coefficient (labda)
!      PTRIAD(2) : Power of the tail of the spectrum (p)
!      PTRIAD(4) : xxx (delta)

! 6. Local variables

      INTEGER, SAVE        :: IENT=0                                ! Number of ↵
entries into this subroutine
      INTEGER              :: ID                                    ! Grid ↵
counter in spectral space (direction)
      INTEGER              :: II                                    ! Counter ↵
      INTEGER              :: IS1, IS2, IS3                          ! Grid ↵
counter for spectral frequency

```

```

    REAL          :: SIG1, SIG2, SIG3          ! ↓
frequencies of 3 components

    REAL          :: ACL1, ACL2, ACL3          ! action ↓
densities of 2 components

    REAL          :: KW1, KW2, KW3            ! wave ↓
numbers of 3 components

    REAL          :: CG1, CG2                ! wave group ↓
velocities at interacting frequencies

    REAL          :: RS3, SS                 ! aux. var. ↓
for determining SIG3

    REAL          :: DSIG                    ! frequency ↓
increment

    REAL          :: SIGMEAN                 ! mean freq ↓
of the 3 components

    REAL          :: KMEAN                   ! mean wave ↓
number

    REAL          :: SDIA1, SDIA2            ! source ↓
term to diagonal

    REAL          :: SRHS

    REAL          :: DISPC                    ! dispersion ↓
coefficient

    REAL          :: BETA

    REAL          :: SINABS

    REAL          :: BIPH

    REAL          :: URSLOC                   ! aux. ↓
coefficient

! 7. SUBROUTINES USED

!     INTEGER :: CNTSIG

! 8. SUBROUTINES CALLING

!     SOURCE

! 9. ERROR MESSAGES

!     ---

! 10. REMARKS

!     ---

! 11. STRUCTURE

!     -----
!     For all active directions do
!       For all first components do
!         determine frequency and wave number of component
!       For all second components do
!         determine frequency and wave number of components
!         determine frequency of third resonating component
!         If this frequency is within spectral range
!           Then determine source terms
!         determine contributions to matrix
!     -----

! 13. Source text

!$OMP MASTER

```

40.22

```

IF (LTRACE) CALL STRACE (IENT,'STRICL')
!$OMP END MASTER
40.22

URSLOC = (GRAV*2.*SQRT(ETOT))/(SQRT(2.)*SMEBRK**2*DEPLOC**2)
BIPH = PI/2 * (TANH(PTRIAD(4)/URSLOC) - 1.)
SINABS = ABS(SIN(BIPH))
BETA = PTRIAD(1) / DEPLOC / DEPLOC * SINABS *
&      KMESPC**(1-PTRIAD(2))

! first loop over all directions
DO II = IDDLLOW, IDDTOP
  ID = MOD (II - 1 + MDC, MDC) + 1
! first loop over all frequencies
  DO IS1 = 1, MSC
    SIG1 = SPCSIG(IS1)
! second loop over all higher frequencies
    DO IS2 = IS1+1, MSC
      SIG2 = SPCSIG(IS2)
! determine properties of 3d component
      SIG3 = SIG2 - SIG1
      IF (SIG3.GT.SPCSIG(1)) THEN

        SS = ALOG(SIG3/SPCSIG(1)) / FRINTF
        IS3 = INT(SS) + 1
        RS3 = SS - REAL(IS3 - 1)

        ACL1 = ACLOC(ID,IS1)
        ACL2 = ACLOC(ID,IS2)
        ACL3 = RS3 * ACLOC(ID,IS3+1) + (1. - RS3) * ACLOC(ID,IS3)
        KW1 = KWAVE(IS1)
        KW2 = KWAVE(IS2)
        KW3 = RS3 * KWAVE(IS3+1) + (1. - RS3) * KWAVE(IS3)
        CG1 = CGO(IS1)
        CG2 = CGO(IS2)
! determine properties of triad
        KMEAN = 0.3333 * (KW1 + KW2 + KW3)
        DELTAK = KW2 - KW1 - KW3
        DISPC = TANH(KMEAN * DEPLOC) / (KMEAN * DEPLOC)

        SDIA1 = BETA * ACL3 * SIG1 * CG1 * KW1**(PTRIAD(2))
&          * DISPC**2
        SDIA2 = BETA * ACL3 * SIG2 * CG2 * KW2**(PTRIAD(2))
&          * DISPC**2

        IF (ANYBIN(ID,IS1)) THEN
          DSIG = FRINTF * SIG2
          SRHS = SDIA2 * ACL2
          IMATDA(ID,IS1) = IMATDA(ID,IS1) + SDIA1 * DSIG
          IMATRA(ID,IS1) = IMATRA(ID,IS1) + SRHS * DSIG
        ENDIF
        IF (ANYBIN(ID,IS2)) THEN
          DSIG = FRINTF * SIG1
          SRHS = SDIA1 * ACL1
          IMATDA(ID,IS2) = IMATDA(ID,IS2) + SDIA2 * DSIG
          IMATRA(ID,IS2) = IMATRA(ID,IS2) + SRHS * DSIG
        ENDIF
      ENDIF
    ENDDO
  ENDDO
ENDDO
RETURN
END subroutine STRICL
40.45

```

Appendix B Smith measurements

The table below was taken from Smith (2004)

Case	$T_{p,1}$	$T_{p,2}$	H_{m0}	γ_p
1	2.5	1.0	0.09	20
2	2.0	1.0	0.09	20
3	1.75	1.0	0.09	20
4	1.5	1.0	0.09	20
5	1.25	1.0	0.09	20
6	2.0	-	0.09	20
7	1.5	-	0.09	20
8	1.0	-	0.09	20
9	1.25	1.0	0.06	20
10	1.5	1.0	0.06	20
11	1.75	1.0	0.06	20
12	2.0	1.0	0.06	20
13	2.5	1.0	0.06	20
14	1.25	1.0	0.09	3.3
15	1.75	1.0	0.09	3.3
16	2.5	1.0	0.09	3.3
17	1.25	1.0	0.09	100
18	1.75	1.0	0.09	100
19	2.5	1.0	0.09	100
20	1.0	-	0.09	3.3
21	1.0	-	0.09	20
22	1.0	-	0.09	100
23	1.25	-	0.09	3.3
24	1.25	-	0.09	20
25	1.25	-	0.09	100
26	1.75	-	0.09	3.3
27	1.75	-	0.09	20
28	1.75	-	0.09	100
29	2.5	-	0.09	3.3
30	2.5	-	0.09	20
31	2.5	-	0.09	100

Appendix C Results calibration

Case	γ	λ	$\varepsilon(\mathbf{H}_{m0})_{\text{DCTA}}$	$\varepsilon(\mathbf{H}_{m0})_{\text{LTA}}$	$\varepsilon(\mathbf{T}_{m01})_{\text{DCTA}}$	$\varepsilon(\mathbf{T}_{m01})_{\text{LTA}}$
1	0.770	0.100	0.0012	0.0015	0.042	0.131
2	0.785	0.080	0.0013	0.0015	0.042	0.094
3	0.790	0.055	0.0013	0.0018	0.037	0.101
4	0.805	0.060	0.0010	0.0018	0.022	0.097
5	0.810	0.080	0.0013	0.0021	0.012	0.061
6	0.770	0.200	0.0037	0.0019	0.047	0.132
7	0.710	0.160	0.0047	0.0053	0.029	0.117
8	0.915	0.100	0.0012	0.0025	0.008	0.073
9	0.840	0.110	0.0007	0.0007	0.012	0.049
10	0.810	0.120	0.0013	0.0018	0.015	0.067
11	0.825	0.080	0.0009	0.0014	0.027	0.082
12	0.845	0.095	0.0015	0.0018	0.026	0.075
13	0.795	0.140	0.0016	0.0017	0.045	0.084
14	0.830	0.080	0.0007	0.0012	0.021	0.056
15	0.805	0.050	0.0010	0.0014	0.035	0.078
16	0.830	0.060	0.0013	0.0013	0.043	0.081
17	0.775	0.090	0.0021	0.0030	0.009	0.066
18	0.790	0.120	0.0025	0.0028	0.031	0.118
19	0.765	0.150	0.0026	0.0029	0.056	0.149
20	0.885	0.085	0.0011	0.0015	0.023	0.061
21	0.905	0.090	0.0009	0.0023	0.014	0.075
22	0.940	0.110	0.0017	0.0035	0.008	0.081
23	0.735	0.125	0.0026	0.0035	0.012	0.040
24	0.715	0.145	0.0033	0.0045	0.015	0.058
25	0.690	0.160	0.0035	0.0050	0.021	0.075
26	0.730	0.180	0.0038	0.0032	0.025	0.078
27	0.720	0.210	0.0044	0.0036	0.021	0.101
28	0.705	0.210	0.0046	0.0036	0.025	0.125
29	0.730	0.235	0.0043	0.0027	0.054	0.098
30	0.690	0.280	0.0049	0.0027	0.072	0.129
31	0.690	0.285	0.0047	0.0027	0.087	0.163

